8-2011

Synthesis, extraction, dissolution, and voltammetry of f-species in a room temperature ionic liquid solvent

Wendy Jacqueline Pemberton
University of Nevada, Las Vegas

SYNTHESIS, EXTRACTION, DISSOLUTION, AND VOLTAMMETRY OF

F-SPECIES IN A ROOM TEMPERATURE IONIC LIQUID SOLVENT

By

Wendy Jacqueline Pemberton

A dissertation submitted in partial fulfillment

of the requirements for the

Doctor of Philosophy Degree in Radiochemistry

Department of Chemistry

College of Sciences

The Graduate College

University of Nevada, Las Vegas

August 2011

We recommend the dissertation prepared under our supervision by

Wendy Jacqueline Pemberton

entitled

Synthesis, Extraction, Dissolution, and Voltammetry of F-Species in a Room Temperature Ionic Liquid Solvent

be accepted in partial fulfillment of the requirements for the degree of

Doctorate of Philosophy in Radiochemistry
Department of Chemistry

Kenneth Czerwinski, Committee Chair

David Hatchett, Committee Member

Alfred Sattelberger, Committee Member

Ralf Sudowe, Graduate College Representative

Ronald Smith, Ph. D., Vice President for Research and Graduate Studies
and Dean of the Graduate College

August 2011

Abstract:

Room temperature ionic liquids (RTILs) are salts that are liquids from as low as -96 °C to up to 100 °C. RTILs are of high interest in many fields of study because of their negligible vapor pressure, high electrochemical stability, high conductivity, and wide electrochemical windows. These diverse solvents have recently been used in organic synthesis, as extraction solvents, and as electrochemical solvents. It is as a direct result of the multifunctional capabilities of these RTIL solvents that they are examined in this work. The ability to probe the chemistry of lanthanides and actinides is based on the unique properties of the cation/anion pair used in the RTIL solutions. The ionic solvent allows studies to be performed under conditions that minimize hydrolysis of the actinide species of interest. In addition, the RTIL solutions can be utilized in the potential dependent electrodeposition of f-elements in their metallic form. However, lanthanide and actinide species cannot always be added into the RTIL directly. Methods of introducing several f-species into the RTIL solvent will be explored. Complexes containing the $N(SO_2CF_3)_2$ anion were synthesized for this work. The synthesis and resulting mechanisms of addition of f-species into the RTIL will be discussed.   Electrochemical analysis of the soluble species will be presented. Separation of the f-species from the RTIL solvent onto the surface of the electrode via potential mediated electrodeposition will be explored. The nature of each deposit was evaluated with scanning electron microscopy and the accompanying energy dispersive spectroscopy. These results will be presented. Finally, conclusions will be reviewed

regarding the feasibility of the use of RTIL solvents as a tool in future separations of

lanthanides and actinides from spent nuclear waste and other mixed systems.

Acknowledgements

In the process of pursuing my doctoral degree, I have been so very fortunate to have had the support of many spectacular individuals. I am extremely thankful to my advisor and mentor, Dr. Kenneth Czerwinski, for developing such an amazing program at UNLV. His guidance was an invaluable component to my education. I am also appreciative for my co-advisor, Dr. David Hatchett, for allowing me the opportunity to expand my radiochemistry knowledge to include electrochemistry. His knowledge and insight was an integral component to my education. I would also like to thank my remaining committee members for all of their support. Dr. Al Sattelberger provided patience and knowledge for which I am very grateful. Finally, I would like to thank Dr. Ralf Sudowe. His input was vital during the development of this Dissertation. I am extremely thankful to him for his constant encouragement throughout this process.

To Julie Bertoia, Trevor Low, Thomas O'Dou, Dr. Richard Gostic, Dr. Julie Gostic, and Dr. Kiel Holliday, you are such an amazing group of people. Each of you has been the truest of friends to me. You have inspired me by your knowledge, and your willingness to go the extra mile to share that knowledge with others. I will always cherish every one of you.

To Nikki Del Quadro, Emilia Gross, and Teri Dixon, I am thankful to each of you for your friendship, and for your reminding me to relax and let the pieces fall where they may when the days seemed rough. I feel so lucky to have such wonderful friends in my life.

To RaJah Mena, my kindred spirit, the Ethel to my Lucy. You have listened to me for countless hours discussing every aspect of this document. You provided a

scientific sounding board for questioning my thoughts, and support for every rough moment. You are an amazing friend, and someone that I am absolutely proud to know.

To my parents, Cynthia and Robert Chernesky, I am completely honored to have such loving and giving role models. I am who I am today because you encouraged me to grow into being the type of person that believes anything is possible if I simply try hard enough.

To my husband, Andrew Pemberton, I have no words to express my love or gratitude to you. I know that times were beyond difficult for us as I pursued this dream of mine. You are my rock, my best friend, and I am so glad to have gone through this journey with you by my side. And just as when we were essentially kids, I will love you with all of my heart, sole, and soul, always.

Table of Contents

List of Tables

List of Figures

Chapter 1: Introduction

1.1   Room Temperature Ionic Liquid Overview

Room temperature ionic liquids (RTILs) are useful solvent systems that have been utilized recently in the study of f-elements. Research can be found in the literature regarding RTIL solutions including extraction, synthesis, electrochemistry, and spectroscopy.[1, 2, 3] The ability to probe the chemistry of lanthanides and actinides is based on the unique properties of the cation/anion pair used in the RTIL solutions. The RTIL solvent can be anhydrous, which allows studies to be performed minimizing hydrolysis of the f-element species of interest.

The same RTIL system used to probe the electrochemical properties can also be used in the extraction of f-elements from aqueous solutions.[4] RTIL solvents have also received a great deal of attention with respect to direct dissolution of lanthanide and actinide solids for use in the possible reclamation of waste materials and unused fuel from nuclear fission processes.[5,6,7,8] In addition, the work presented in this dissertation will demonstrate that RTIL solutions can be utilized in the potential dependent electrodeposition of f-elements in their metallic form. This process is based on the relatively large electrochemical potential window afforded by the reduction/oxidation of the cation/anion combination.[9]

1.2   Synthesis of the RTIL

RTILs are ionic solvents that are composed of an anion and cation that, when combined, form a solution from approximately -100 °C to +100 °C. The melting point of the RTIL is based solely on the choice of cation/anion pairs.[9] RTILs are often considered green solvents because they have negligible vapor pressure and high thermal stability in contrast to common organic solvents. While they are not always "green" in terms of toxicity, RTILs do offer improvements over many volatile organic solvents. In the end, the exact anion and cation composition will determine the relative chemical toxicity for each RTIL.[10]

Modern RTILs have many applications including chromatography, extraction, and inorganic/organic synthesis.[10]   In addition, they can be utilized as solvents for voltammetric experiments based on their potentially high electrochemical conductivity and stability.[4] The large number of cation/anion pairs available allows the physical and chemical properties of the RTILs to be logically constructed and tailored.[5] Seddon et al described a representative sampling of anion and cation combinations.[11] Typical cations include 1-alkyl-3-methylimidazolium, N-alkyl-pyridinium, and tetraalkyl-ammonium (Figure 1.1).
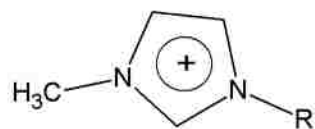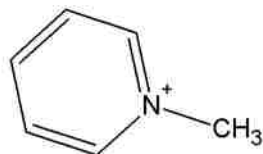
1-alkyl-3-methyl-imidazolium   N-alkyl-pyridinium
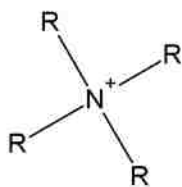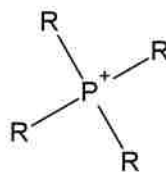
Tetra-alkyl-ammonium   Tetra-alkyl-phosphonium

Figure 1.1. A selection of commonly used RTIL cations

Common anion choices range from n-bis(trifluoromethansulfonyl)imide (TFSI) to acetate based on the miscibility of the anion with water (Figure 1.2).[11]
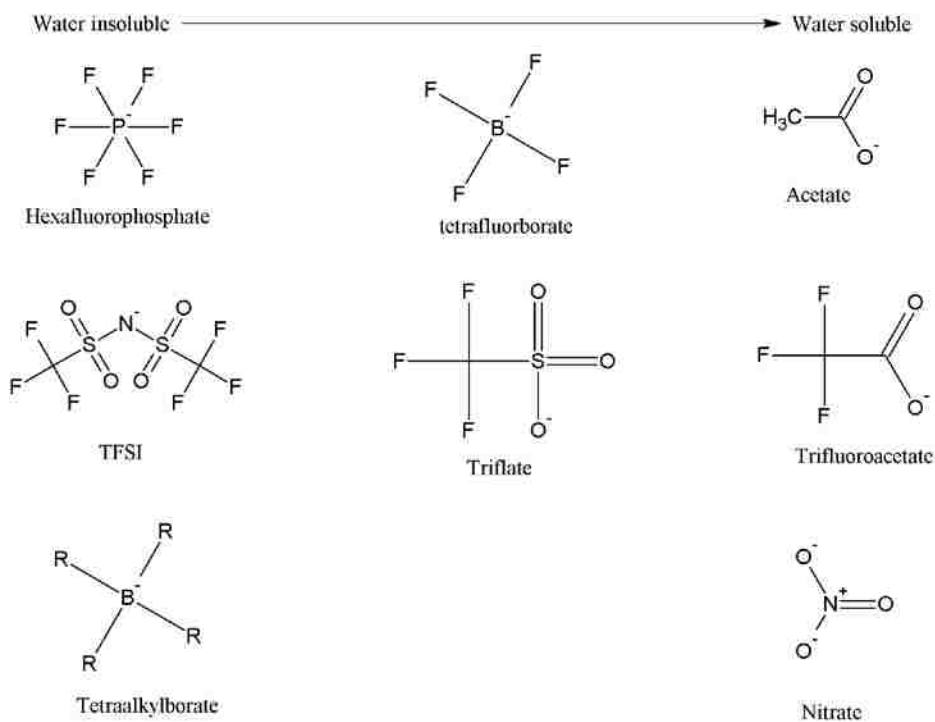
Figure 1.2. A selection of commonly employed anions grouped according to their solubility in water.

In cases where high water stability and low viscosity are required, TFSI is the anion of choice. The TFSI anion has become widely used in RTIL solutions[7] because it can lower the melting point of salts made from ammonium cations,[6] while maintaining high electrochemical conductivity. The TFSI anion is also exploited as a coordinating ligand with lanthanide and actinide ions.[8]

The solution viscosity and conductivity are also important factors that must be considered when selecting the cation. The alkyl chain interactions of ammonium cations

are strongly influenced by the length and branching of alkyl groups. The chain-chain interactions of the alkyl groups in the ammonium cation strongly influence the melting point and viscosity of the resulting ionic liquid.[12] In electrochemical reactions, the reduction of the cation must be at potentials more negative than the reaction to be examined. Ring based structures such as alkyl substituted imidazolium cations have also been used to prepare RTIL solutions. However, previous studies have shown that the potential dependent reductive decomposition of the imidizolium rings typically occurs at potentials that preclude the electrochemical reduction of trivalent actinides to metal.[12,13] In these studies, the tri-methyl-n-butyl ammonium cation was selected for the relatively low viscosity and melting point when combined with TFSI.[14] In addition, the tri-methyl-n-butyl ammonium cation is also electrochemically stable in regions that encompass the negative potentials required for the reduction of actinide species to metal. Figure 1.3 shows the structure of the RTIL used in this work.
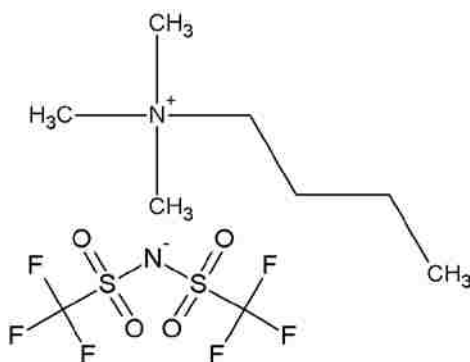
Figure 1.3. TFSI anion paired with [Me$_3$N^{n}Bu] cation to form the RTIL used in this work.

1.3 Benefits of RTIL Solutions

For the actinides, RTILs have potential applications in nuclear fuel cycle separations.[13,14,15,16,17] PUREX is a liquid-liquid extraction process that is used for extracting plutonium and uranium from spent nuclear fuel.[18] In this process, tri-n-butylphosphate (TBP) forms an organic complex with the actinide being extracted from the spent fuel, separating it from the fission products and other actnides.[19] RTILs could be used as an alternative extraction system, replacing the n-dodecane solvent that is used with TBP.[20,19] It may also be possible to create an ionic liquid, such that it can replace both the extractant and the solvent.[21] Once the uranium or plutonium is present in the ionic liquid, then the advantage is clear: The electrochemical properties of the RTIL solvent can be exploited by simply electrodepositing the actinide onto an electrode. This process has not been demonstrated in an aqueous solvent, where the electrochemical window is limited by the oxidation of water and hydrogen reduction. The RTIL solvent has a much larger potential window, which is governed by the oxidation of the anion and the reduction of the cation (Figure 1.4).
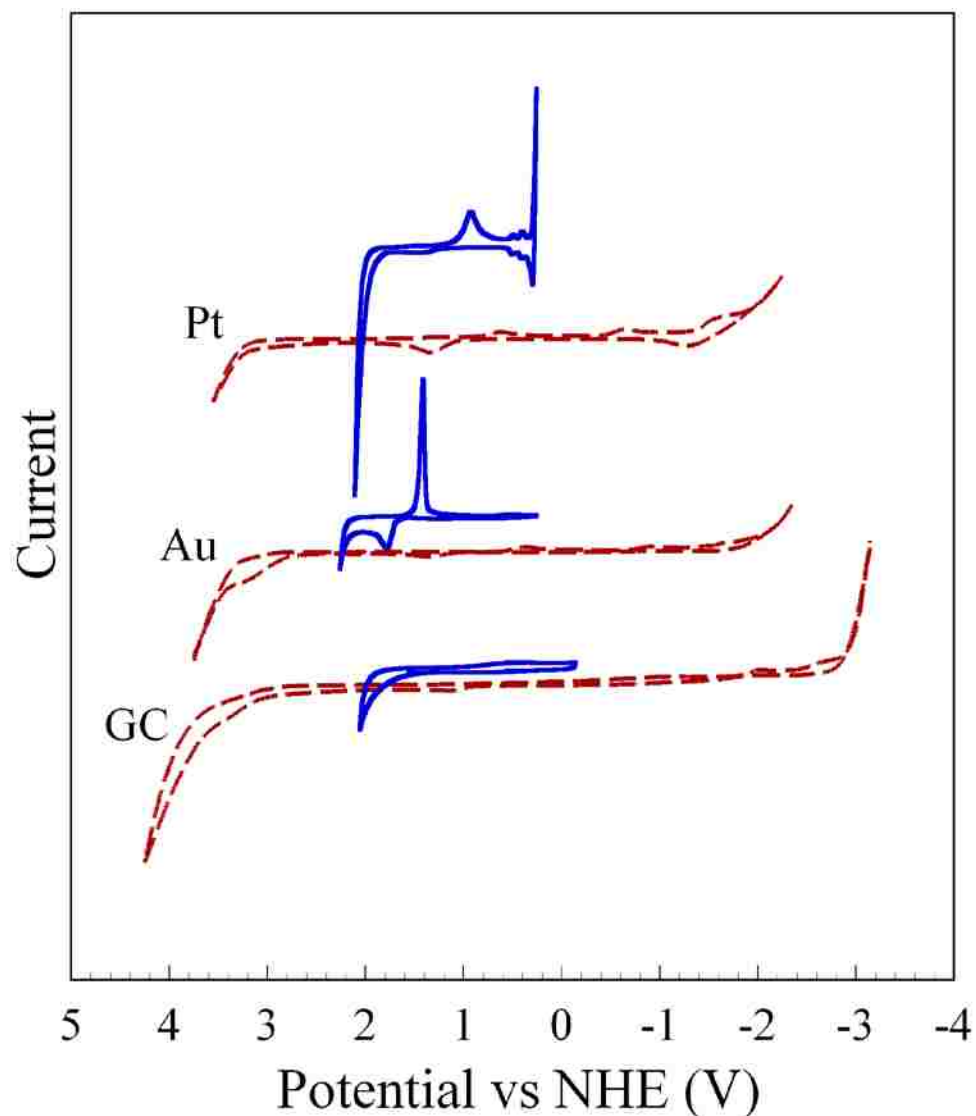
Figure 1.4. Comparison of [Me$_3$N^{n}Bu][TFSI] RTIL cyclic voltammetry background (red, dashed) to aqueous H$_2$SO$_4$ background (blue, solid) using three different working electrodes, glassy carbon (GC), gold (Au), and platinum (Pt), (labeled).

It is clear from Figure 1.4 that the RTIL solvent potential window is much larger than that of the aqueous solution. This large region can be exploited in separations schemes by removing a species from the RTIL solution through the selection of the appropriate electrochemical potential for deposition onto the electrode surface. If more than one species is to be removed from the RTIL solvent, differences in deposition

7

potential for each species can be utilized to separate and remove them individually from the RTIL. For example, it has been previously shown that plutonium electrodeposition can be achieved at -2.1 V vs Ag/AgCl from molten salt eutectic systems.[22] Uranium-metal deposition in the molten salt system has been reported to occur at -1.5 V vs Ag/AgCl.[23] Should both the uranium and the plutonium be present in the molten salt, the above eutectic potentials for electrodeposition should be sufficiently far enough from one another to allow for the *tunable removal* of both actinide components.[24]

The intended use of the actinide dictates the desired level of separation efficiency for this process. The proliferation advantage of the molten salt system is that there are extreme difficulties in obtaining pure plutonium. However, if the goal is to separate the plutonium from the fission products for the purpose of recycling it for further use in the fuel cycle, then the isolated material could be desired. Kinoshita et al reported preferential, but not complete, separation of uranium from plutonium in a U–Pu–Zr alloy fuel.[25] Lebedev et al studied the factors that dictate complete versus partial separations of uranium from common fission product matrixes. They reported that the effects of molten salt temperature and electrode polarization dramatically influence the degree of separation of the uranium from the plutonium in solution. Additionally, they reported that using bipolar electrodes would allow for a tunable degree of uranium separation from fission products.[26]

RTIL solvents and molten salt systems have similarities with respect to their ionic composition, and differences in terms of the temperature conditions under which they are used. As such, they are comparable only to a degree. Both temperature and specific ionic composition of the solvent will affect the potentials under which deposition

occurs.[27]   The key to the success of the previous molten salt electrodeposition example is that the potentials are sufficiently separated such that either plutonium or uranium could be preferentially removed from the RTIL solvent.

The comparison to the molten salt eutectic demonstrates that conditions exist in which actinide separations could be achieved by electrochemically driven deposits of uranium and plutonium species at distinct potentials. It would be expected that some shifting of deposition potentials from the molten salt to the RTIL solvent may occur, but as long as the potentials are still suitably separated, then the design of the separations scheme still applies. While the theory behind this process applies to RTIL, aqueous, and molten salt systems, the advantage of the RTIL solution is that the potential window is up to three times larger than the aqueous solvent while being at substantially lower temperatures than the molten salts.

RTILs have a vast number of potential combinations,[10,11] allowing for a tunable system that will assist in meeting the intended requirements of the anticipated use, specifically for proliferation resistance or fuel refabrication. This allows potentials for deposition to be reached at room temperatures that have not previously been accessible in aqueous solution.   Another advantage is that after the plutonium and uranium are reclaimed and separated from the RTIL, the ionic liquid would then be available for repeated cycles of extraction and electrodeposition. This methodology demonstrates a direct approach to separate and reclaim common fission products from an RTIL solution. As partitioning by potential mediated electrodeposition is the end goal of the possible separation scheme, obtaining a clear understanding of this process is vital, and the use of the RTIL solvent is a necessity.

1.4 Examination of f-elements in the RTIL solvent

Introducing the species of interest into the RTIL system can be problematic due to ligand solubility. In the ionic liquid used in this research, $[Me_3N^nBu][TFSI]$, f-elements cannot always be added directly as commonly available salts. In the literature, as well as in this research, it has been observed that TFSI can form a complex with actinide and lanthanide species.[28] Formation of a complex with the anion creates neutral species that shares a common ligand with the RTIL solution, thus potentially increasing solubility. Forming a complex that shares a common ligand with the solvent also holds potential in reducing cross-contamination of the counter-ligand during extraction schemes. The lack of cross contamination is a direct result from the sharing of the counter-ligand between the extracted complex and the RTIL solution, thus no additional species aside from the actinide of interest are introduced into the RTIL.

Three complexes were synthesized during this research with the TFSI anion . The specific details regarding the synthesis of each product is presented in Chapter 3. These three species, $Sm(TFSI)_3(H_2O)_3$, $UO_2(TFSI)_2$, and $U(TFSI)_3$, were examined to evaluate the solubility and subsequent separation of the f-element complex by electrodeposition.

In Chapter 4, the details on the extraction of $Sm(TFSI)_3(H_2O)_3$ are presented. The extraction of $Sm(TFSI)_3(H_2O)_3$ from aqueous solution was compared to both $SmCl_3$ and SmI_2. The extraction data suggest that forming a complex with TFSI increases the maximum solubility of samarium extracted into the RTIL solution. When a pH of 9.0 and above was achieved, 100% extraction efficiency was observed for the samarium. Once

extracted into the RTIL, electrochemical mediated separation of samarium from the RTIL solution at an Au electrode was achieved.

In Chapter 5, the results from using UO_2CO_3 as a means to introduce uranium into the RTIL are presented. Uranyl carbonate dissolution was achieved by adding an excess of acid, H(TFSI), a species common to the RTIL. The initially insoluble species, UO_2CO_3 can be incorporated directly into the RTIL by argon assisted dissolution via displacing the CO_3^{2-} ligand and subsequent formation of a $UO_2(TFSI)_2$ complex. The displacement of the CO_3^{2-} species occurs through the formation of carbonic acid, and is limited by the amount of H^+ in solution. By adding the H(TFSI), the quantity of H^+ available is increased, and thus increases the formation of carbonic acid and the product $UO_2(TFSI)_2$. The resulting $UO_2(TFSI)_2$ product was determined to be soluble in the RTIL at concentrations of approximately 0.4 M. The $UO_2(TFSI)_2$ was then analyzed using electrochemistry techniques and electrodeposited at Au and GC electrodes.

In Chapter 6, the preliminary results of the direct addition into the RTIL of both $U(TFSI)_3$ and the reaction precursor, $UI_3(THF)_4$, are presented. Both the $U(TFSI)_3$ and the $UI_3(THF)_4$ species were directly soluble in the RTIL at all concentrations examined, up to 0.05 M. For both the $U(TFSI)_3$ and the $UI_3(THF)_4$ complexes, metal deposition was achieved at the same electrochemical potential, indicating that the examined ligands do not appreciably influence the thermodynamic reduction of the uranium species. However, the interactions of the f-species with ions common to the RTIL solvent cannot be ignored for neutral species extraction. As stated previously, there is an advantage to utilizing a species with a common ion to the RTIL in that no additional undesired, or

more specifically contaminant, ligands will be potentially introduced into the ionic liquid during extraction. This is because TFSI anion would already be present in the RTIL.

Each chapter contains summary conclusions for each species, and Chapter 6, in addition to the preliminary U(III) results, presents overall conclusions and recommendations.

This dissertation and the research contained within explored multiple methods of introducing f-elements with varying oxidation states into the RTIL, $[Me_3N^nBu][TFSI]$. Each species was successfully introduced into the RTIL solvent and subsequently removed by electrodeposition. These results demonstrate that the RTIL solvent is a useful tool that can be used to investigate the electrochemical properties of lanthanides and actinides whether they are introduced by ligand displacement followed by complexation, extraction, or direct dissolution. More importantly, in all cases the electrodeposition of the actinides and lanthanides from RTIL solutions was achieved. The methodology outlined in this dissertation will be used to examine alternative methods that may prove useful in future separation schemes.

1.5 Scope of this Research

The fundamental concept of this work was to explore actinide/lanthanide species dissolution, extraction, and electrochemical properties in RTIL solutions. Multiple routes for the introduction of f-species into the RTIL and the evaluation of electrochemical reclamation of species were envisioned and explored.

Chapter 2: Instrumentation and Experimental design

Each section in this chapter contains an overview of the instruments that were used in this work along with a brief description of the experimental methods that were applied.

2.1 Ultra-Violet Visible Spectroscopy

The potential energy of a molecule can be determined by summing its electronic, vibrational, and rotational energies. The energy that a molecule possesses can be assigned specific energy levels, or states. In ultra-violet visible (UV-Vis) spectroscopy, a photon beam is passed through a sample, and absorption causes excitation of electrons within the individual states of the molecules in the sample. These excitations can lead to transitions between the energy levels (Figure 2.1). [29]
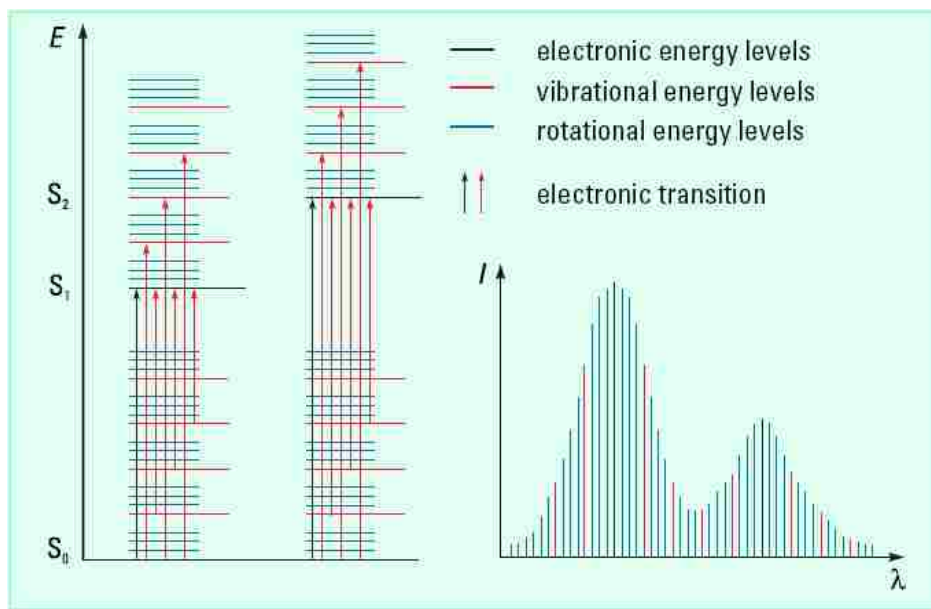
Figure 2.1. Reproduction reflecting electronic transitions and the corresponding spectra from Owen, 2000

Figure 2.1 demonstrates that the various absorption energies are associated with different wavelengths that produce a unique response for each sample. The instrument measures the reference light intensity prior to passing through the sample (I_o), and this value is compared to the intensity of the light after it has passed through the sample (I). The ratio, I/I_o, is referred to as transmittance, T (typically expressed as %T). The relationship between absorbance (A), and transmittance is reflected in Equation 2.1:[29]

$$A = -\log(T) \text{ or } -\log(\%T/100)$$
<div align="right">Equation 2.1</div>

A double beam spectrophotometer setup was used in this work. For this measurement the light was split into two beams before passing through the sample. The first beam (I_o) is passed through a reference sample, and the second beam (I) is passed

through the sample to be analyzed.[30] The result produces a spectrum where the reference

sample absorbances have been accounted for as background. (Figure 2.2).
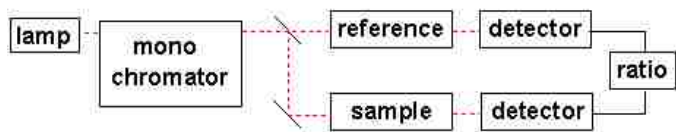
Figure 2.2. Block diagram of a generic UV-Vis double beam setup

There is a linear relationship between the concentration of the sample and the

amount of energy that it absorbed that can be defined by the Beer-Lambert Law. Here,

the concentration for the sample is high enough to be measured, but low enough such that

the absorbance response remains linear.[29,30] The specific linear range will vary for each

species in solution. This region of linear response is governed by the Beer-Lambert Law:
[29,30]

$$A \ = -\log T \ = \ \varepsilon bc$$ Equation 2.2

Where: A=absorbance
T=transmittance
ε=molar absorptivity
b=path length
c=concentration

The instrument will provide the transmittance. Using the relationship described in

Equation 2.1, the absorbance can then be determined. The path length is known based on

the cuvette that was utilized in the experiment. The two potential unknowns remaining in

Equation 2.2 are the molar absorptivity and the concentration.[29] When one of these factors is known, then the remaining unknown can be determined from the spectrum.

UV-Visible spectra can also provide valuable information on solution speciation.[29,30] This is because of the interactions within the sample solution. This includes both intra-molecular interactions that occur between multiple atoms of the species in solution, and inter-molecular interactions that occur between the species dissolved in the solution and the solvent itself. The result of these interactions is absorbance bands that occur at unique energies within the sample cell upon excitation from the beam. These responses within the cell will yield an observable band structure in the UV-Vis spectrum.[30]

2.1.1 UV-Vis Sample Analysis Details

All spectra were collected using a dual beam Cary6000i UV-Vis-NIR spectrophotometer in a 10 mm cuvette. In chapters 3 and 4, the $Sm(TFSI)_3(H_2O)_3$ spectra were collected in quartz cuvettes. For the $UO_2(TFSI)_2$ measurements shown in chapters 3 and 5, reduced volume (1 mL) quartz cuvettes were employed. In the U(III) analysis presented in chapters 3 and 6, air stoppered (3.5 mL) glass cuvettes were used.

2.2 Infrared Spectroscopy

Infrared (IR) spectroscopy is a complimentary technique to UV-Vis because it provides information concerning vibrational and rotational transitions of molecules. When energy in the mid IR region is passed through the sample, the excitation energy is not as high as that of the UV-Vis region and lower energy transitions are induced. These transitions are influenced by the chemical species providing information regarding functional groups and their interactions within the sample.[30,31] In these cases, discrete vibration and rotation levels can be observed. This occurs when the frequency of the energy level is equal to the frequency of the IR light source. Infrared absorption will only occur if the energy of the beam matches the excitation energy of the molecule and if there is a change in the electric dipole moment of the molecule.[3] Several different types of bending and stretching motions can be observed under these conditions. These movements include stretching, scissoring, wagging, twisting, and rocking.[31] These motions yield an observable band structure in the FT-IR spectrum. Each sample will have an individual spectrum that can be used for identification of the specific functional groups contained in the molecule.[30] Additional information on FT-IR fundamentals can be found in the literature.[31]

For this work, a Fourier transform infrared (FT-IR) instrument was utilized. In this method, the IR light passes through the sample and is channeled through an interferometer. Figure 2.3 displays a schematic for a simple interferogram for a monochromatic source.
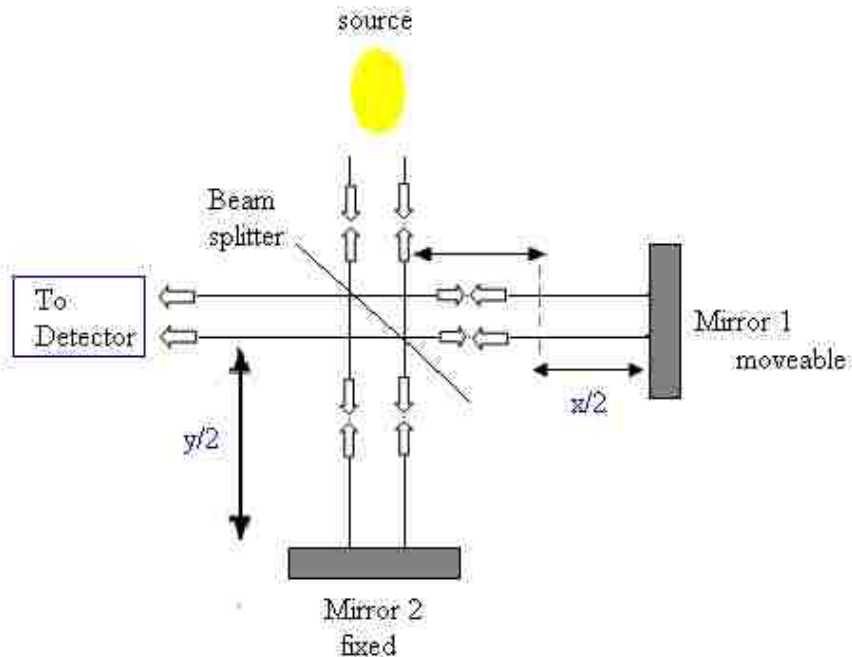
Figure 2.3. Schematic view of a Michelson interferogram for a monochromatic source.

This method enables the total beam intensity to be measured for as many wavelengths that are simultaneously passed though the detector.[31]   Similarly, a background spectrum must also be collected to provide a reference (I_o) to compare against the sample (I). The same principles between absorbance and transmittance that were described in Section 2.1 can be related to this discussion.[30]   After repeating this cycle many times, the computer analyzes this data using complex mathematical operations that process the signal using time and frequency as the domain.[31]   The fundamental concept of this process can also be understood by examining a simplified example using Equation 2.3.

$$I \propto 4r^2t^2c^2E_m^2 \cos^2(\omega t - 2\pi y_1 \upsilon)\cos^2(\pi \upsilon x)$$

Equation 2.3

Where: I=Intensity detected
                            r=reflectance (amplitude)
                            t=transmittance
                            c=constant speed, based on polarization
                            E_m=Average electric field amplitude
                            ω=frequency
                            v=wavenumber (cm^{-1})

Essentially, Equation 2.3 relates the intensity that the monochromator detects to a specific wave number in the spectrum. In practice, a more complicated situation exists in which a polychromatic source is often used. This allows for multiple wave numbers to be analyzed simultaneously, after which a Fourier Transform can be used to process the information. This is done by integrating from wave numbers 0 to v_{max}[19]:

$$I(x) = \int_0^{\upsilon_{max}} I(\upsilon)d\upsilon + \int_0^{\upsilon_{max}} I(\upsilon)\cos(2\pi x)dx$$

Equation 2.4

Using the relationship described in Equation 2.4, the intensity (I) observed in the spectrum for each wave number (x), can be determined after simultaneously collecting the data using a polychromator.[19] The final product of these calculations will infer how much light there is at each wavelength. The resulting information yields the final unique spectral result.

2.2.1 IR Sample Analysis Details

All spectra were taken with Varian 3100 FT-IR Excalibur series using a Smiths detection DurasamplIR in a compartment diamond attenuated total reflectance (ATR) attachment along with Varian Resolutions Pro, version 5.04.009 software. A constant argon atmosphere was maintained during all experiments. Solids were measured using a solid concave tip attachment; solutions were analyzed in a liquid well (Figure 2.4).
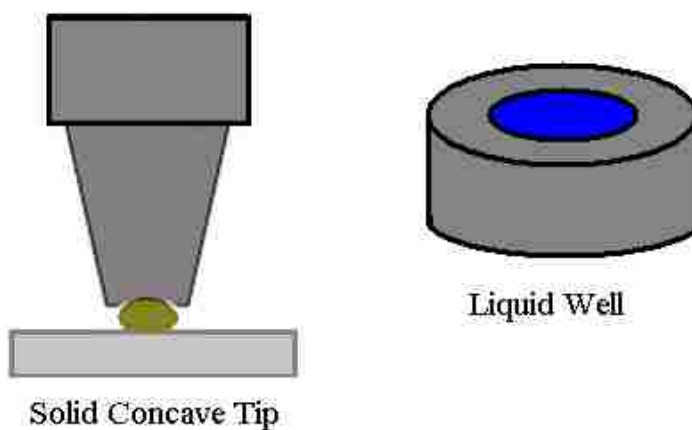
Figure 2.4. ATR accessory pieces for solid and liquid analysis

Chapter 3 presents the spectra obtained during materials synthesis including that of the RTIL used in this work, and $Sm(TFSI)_3(H_2O)_3$. Chapter 4 contains spectra obtained during the analysis and extraction of $Sm(TFSI)_3(H_2O)_3$, and Chapter 5 presents spectra comparing neat RTIL to acidified RTIL to RTIL containing the $UO_2(TFSI)_2$ species.

2.3 Liquid Scintillation Counting

In alpha and beta decay, the particles primarily interact with electrons in the matter they travel through by means of excitation, ionization, or dissociation.[32] Liquid scintillation counting (LSC) is a method that utilizes the photons that can be produced as a result of these excitation interactions; or more specifically, photons can be emitted during de-excitation.[32] To ensure that the maximum amount of photons reaches the detector's photomultiplier tube (PMT), the sample is placed into an organic solvent called scintillation cocktail.[32]

The cocktail contains a scintillator, an emulsifier, and a wave shifter. The scintillator is added to the scintillation cocktail so that the ionizing radiation's excitation energy will be transferred to the solvent, and then transferred to the scintillation molecules. Essentially, this allows each alpha or beta emission to result in a pulse of light.[32] The wave shifter is an organic compound that absorbs the primary scintillator's photons and then re-emits the photon at a longer wavelength. It does this because the photomultiplier tubes used for detection are more sensitive at the longer wavelengths.[33] Finally, an emulsifier or surfactant is added to the scintillation cocktail to ensure sample homogeneity.[33]

Once the photons reach the detector, two photomultiplier tubes (PMTs) are required to ensure that the photons arrive inside of the detector. Once they arrive in the detector volume, they are converted to an electrical current.[33] The results are displayed in units of counts per minute (CPM). An efficiency calibration can be used to relate CPM to the concentration of materials (see Section 2.3.1).[33]

2.3.1 LSC Efficiency Calibration

Matrix and quenching affects can have an impact on the LSC sample counting efficiency. When light is quenched, it has gone through a process where the amount of light coming out of the sample has been reduced.[32,33] This can happen when there is a chemical competition for the excitation energy in the solvent. This situation is a chemical quench. Quenching can also happen optically, which is when the light output from the scintillators is absorbed due to coloring in the sample (Figure 2.5).[32,33]
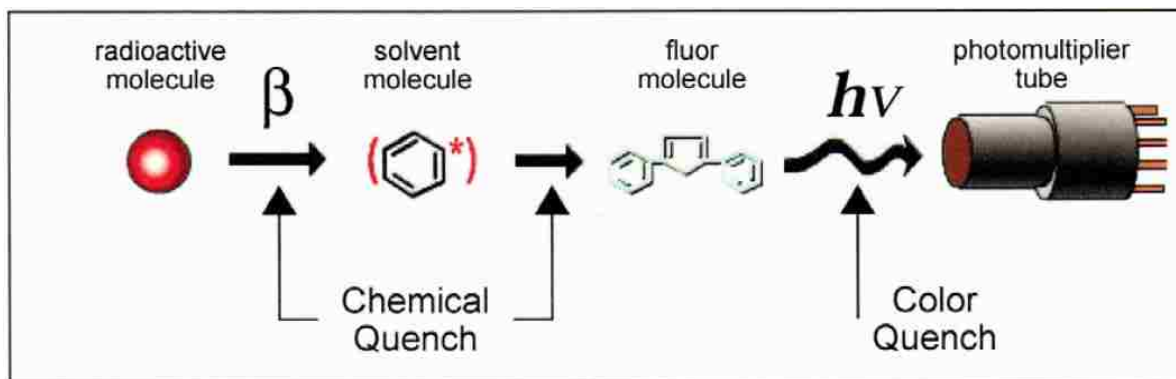
Figure 2.5. Illustration of the scintillation process.[32]

Since quenching will likely always happen, quench indicating parameters (QIPs) were used for normalization. There are two main methods to measure the amount of quenching in the system: Spectral Index of the Sample (SIS) and transformed Spectral Index of the External Standard (t-SIE).[32,33] In this work, t-SIE was utilized. In t-SIE, an external [133]Ba gamma source induces a Compton spectrum in the sample that is measured. The software is able to mathematically analyze the spectrum and provide a value from 0 to 1000, where 0 is the highest amount of quench and 1000 is no quenching.

As quench increases, the t-SIE value decreases, as does the counting efficiency. The relationship between efficiency and quench is demonstrated in Figure 2.6.[33]
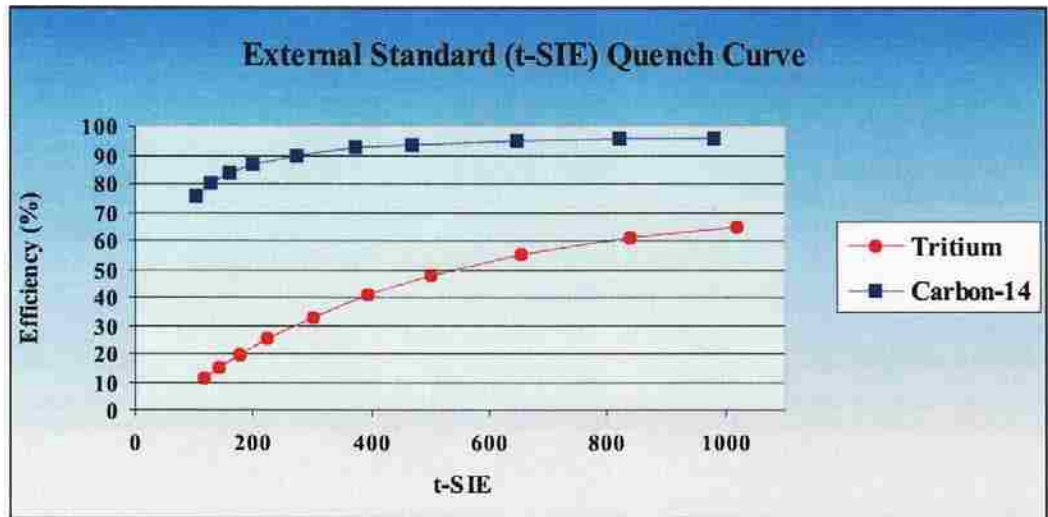
Figure 2.6. Quench curves produced using t-SIE plotted against % efficiency for ^{14}C and ^{3}H β emitters.

For each sample, the LSC instrument provides the CPM as well as the t-SIE value. The actual activity in the sample after correcting for efficiency is represented by decays per minute (DPM). Equation 2.5 reflects the relationship between CPM, DPM, and efficiency.

$$\frac{CPM \times 100}{DPM} = \% \text{ Counting efficiency} \qquad \text{Equation 2.5}$$

Where: CPM = counts per minute
          DPM = decays per minute

In the solubility analysis of the $UO_2(TFSI)_2$ presented in chapter 5, all LSC samples received t-SIE values above 700. Four uranium containing samples of known concentration were analyzed in the RTIL, and the t-SIE values for those samples were in

the range of 700-900. The analysis was replicated five times for each known. In each known sample, the CPM equaled DPM, a 100% efficiency. Therefore after confirming a t-SIE value over 700, for all analysis in this work the CPM value displayed by the LSC instrument was taken to equal the measure DPM activity of the sample.

2.3.2 LSC Instrument parameters

Data was obtained using a Perkin Elmer Precisely Liquid Scintillation Analyzer Tricarb 3100TR instrument running QuantaSmart software. The instrument is capable of partitioning the signal into three energy regions (in the instrumental range of 0 to 2000 keV), that can be set by the user. In this work, the total activity was desired, so the counting region was set to reflect from 100 keV to 1000 keV. A lower energy region was set from 0 to 100 keV. At the high end of the 0 to 100 keV region, a small amount of tailing of the external ^{133}Ba source could be seen. Sample blanks containing only RTIL were also analyzed. The samples were set to count for 45 minutes each, or until the counting error was equal to or less than 2% of the 2σ standard deviation of the total counts.

2.3.3 LSC Sample Analysis Details

Measurements of the ^{233}U were obtained by adding 100 μL of RTIL solution with the ^{233}U tracer to 10 mL of Ultima Gold AB (Perkin Elmer) scintillation cocktail inside of

20 mL plastic LSC vials. While utilizing pipettes allowed for a direct method for obtaining sample aliquots of a pre-determined quantity, all masses were also recorded to reduce potential pipetting errors due to the viscosity of ionic liquid. The ^{233}U was used as a tracer so that the total uranium concentration could be determined as the half-life of ^{238}U is not suitable for scintillation counting of low uranium concentrations. A solid UO_2CO_3 sample containing a mixture of 12 % ^{233}U and 88 % ^{238}U was synthesized for this work. For details on this synthesis and isotopic percentage determination, see Section 3.2.2.

To determine the final total uranium concentrations used in Chapter 5, the following steps were taken:

1. The efficiency was 100%, so that CPM=DPM. This was then converted to activity in Becquerel (Bq):

$$\frac{DPM}{60} = Bq \hspace{4cm} \text{Equation 2.6}$$

2. The decay constant was found using the half life of the isotope:

$$\lambda = \frac{\ln 2}{t_{1/2}} \hspace{4cm} \text{Equation 2.7}$$

Where: $t_{1/2}$=half life (s)

The isotope ^{233}U has a half life of 1.59E5 years and thus a decay constant of 1.38E-13 s^{-1}, whereas ^{238}U has a half life of 4.47E9 years, and decay constant of 4.92E-18 s^{-1}. The five orders of magnitude difference essentially equates to the response being dominated by the ^{233}U isotope at the isotopic molar ratio used for the uranyl carbonate synthesis.

3. The concentration of the sample containing volume (V) was determined by first

   utilizing the relationship between activity and moles of material shown below:

$$A = \lambda N$$
<div align="right">Equation 2.8</div>

Where: A = activity (Bq)
              λ = radioactive decay constant (s^{-1})
              N= number of atoms

Equation 2.8 was rearranged and converted to solution molarity using Equation

2.9:

$$[U]_{total} M = \cfrac{\cfrac{\left(\dfrac{A}{\lambda}\right)}{6.02E23}}{V} \bigg/ \cfrac{\%\,^{233}U}{100}$$
<div align="right">Equation 2.9</div>

Where: A = activity (Bq)
              λ = radioactive decay constant of
                ^{233}U (s^{-1}) = 1.38E-13 s^{-1}
              V = Sample aliquot volume (L)
              6.02E23 = Avogadro's number (atoms/mol)
              $\%\,^{233}U$ = unitless conversion from ^{233}U to $^{total}U$ using the
              percentage of ^{233}U found in the final UO_2CO_3 sample (see
              Section 3.2.2 for this experimental determination)

      In chapter 5, the results are presented from comparing the final concentrations of

uranium in the RTIL to the corresponding UV-Vis data that was obtained during the

experiment.

2.4 Inductively Coupled Plasma Mass Spectrometry

Inductively coupled plasma mass spectrometry (ICP-MS) is a powerful tool that is able to quantitatively measure the majority of isotopes. Introduction of the sample into the instrument varies based on the phase of the analyte.[34] Gas can be directly introduced, and solids are measured by first heating the sample with a laser or heated cell to vaporize the sample. Liquid samples are introduced using a sample introduction system that contains a nebulizer to convert the liquid sample to extremely small droplets which are then moved through the spray chamber into an injector that then injects the liquid droplets into the ICP-MS torch.[34] Samples are introduced into a plasma which ionizes the elements in the sample. The individual ions are then sent through an interface and focusing ion lens, which is directly behind the interface. The ions are separated by their mass to charge ratio as they enter the mass spectrometer; after which they are counted by the detector (Figure 2.7).[34,35]
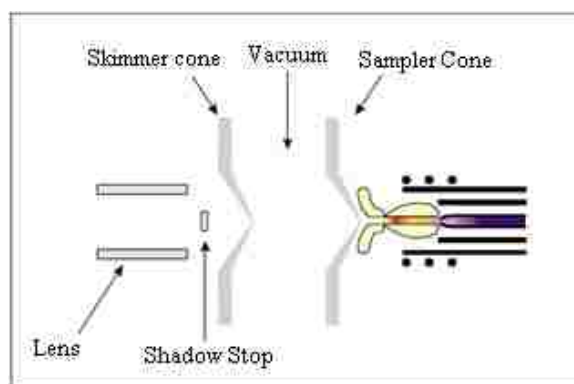
Figure 2.7. ICP-MS filtering lens array

2.4.1 ICP-MS Instrument Parameters

All solid and liquid ICP-MS measurements were taken using an Elan DRC II ICP-MS with Elan software version 3.3 Patch 6 (Build 3.3.16.167e). Solid measurements employed a CETAC LSX-500 laser ablator using DigiLazII Version 1.2 software. Prior to each use, the following manufacturer required settings were used:

Table 2.1. ICP-MS parameters

1	Nebulizer gas flow:	0.90 L/min
2	Argon auxiliary gas flow:	1.20 L/min
3	Plasma gas flow:	15.00 L/min
4	Vacuum pressure:	$< 7 \times 10^{-6}$ torr
5	Radio-frequency power:	1100 Watts

After the initial settings were confirmed, a performance analysis was executed with a tuning-solution that contains multiple analytes in a wide mass range. The results of this analysis were used to ensure that the instrument was working inside of the manufacturer's published parameters for precision and sensitivity of the measurements.

The liquid samples used in the $Sm(TFSI)_3(H_2O)_3$ results presented in chapter 4 were analyzed using a CETAC Technologies autosampler. They were introduced into the ICP-MS via a quartz nebulizer. The instrument was set to introduce each sample to the nebulizer for 90 seconds prior to taking each measurement, from which 5 replicate measurements were obtained. The probe was rinsed in 2% HNO_3 for 60 seconds between samples.

The solid electrode samples presented in chapter 5 were introduced into the ICP-MS instrument by laser ablation. In this technique the solid material can be ionized and

directly introduced into the ICP-MS by irradiation with a laser.[34] The laser was set to a spot size of 20 μm, and each spot was ablated for 45 seconds. Multiple spots in all areas of the electrode were analyzed using this method to obtain information regarding the uniformity of the uranium deposits.

2.4.2 Liquid Sample Preparation

Eight samarium calibration standards were prepared gravimetrically in 2% (wt/wt%) nitric acid from 0 to 300 ppb (0 M to 2.0 μM). The extraction samples used for the samarium analysis presented in Chapter 4 were taken from the aqueous phase. In these experiments, 100 mg samples were placed into a 15 mL centrifuge tube, after which 9.9 g of 2% HNO_3 was added. These samples were shaken for 60 seconds and then analyzed upon completion of each extraction experiment.

2.4.3 Solid Sample Preparation

Methods of electrodeposition from RTIL solution are described during subsequent chapters in this dissertation. In chapter 4, samarium was deposited onto a gold electrode. In chapter 5, uranyl was deposited onto glassy carbon and gold electrodes. In chapter 6, uranium was deposited onto gold electrodes. In all experiments, the electrode surface was carefully rinsed with acetone then dried with a Chemwipe. The electrode exterior was not rubbed, as this could potentially remove the deposit from the surface. Two types

of electrodes were analyzed in this work: A gold sheet and glassy carbon (GC). In the case of the gold sheet, no additional steps were necessary. However, the GC electrode was too long to fit into the laser ablation sample holder, necessitating electrode tip removal for sample analysis.

2.5 Scanning Electron Microscopy

The scanning electron microscopy (SEM) instrument is an effective tool that allows for highly magnified images to be obtained.[36] A filament electron gun is used to send electrons through a vacuum chamber. The electron beam is continuously swept across the sample at high speeds producing a secondary electron response in the sample.[36,37] The image results from the excited electrons being observed at the cathode ray tube. In addition, characteristic x-rays produced in this process can be measured and used to obtain elemental composition of the sample with energy dispersive spectroscopy (EDS), a complimentary SEM tool. [36,37]

Once the electron beam targets the sample, interactions of the electrons with the matter present on the sample are observed. The primary electron source (the electron beam) travels a specific distance into the sample and then collides with another particle.[36] Following this collision, the primary electron will be scattered, and as a result, a teardrop shaped reaction vessel forms. It is in this teardrop reaction vessel where all of the scattering events used in the SEM analysis occur (Figure 2.8). [36]
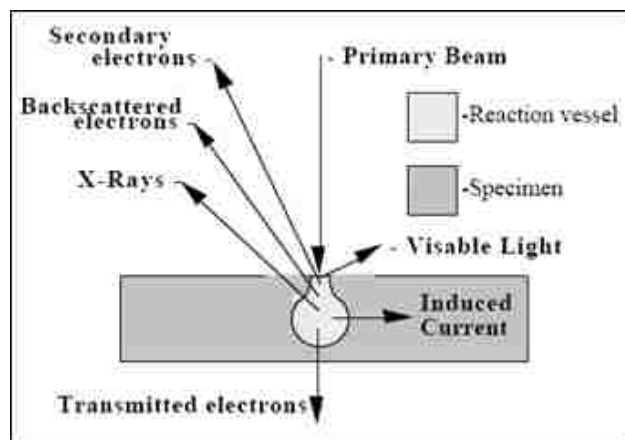
Figure 2.8. SEM Electron scattering reaction vessel.

There are several types of possible scattering events. X-rays are emitted as a result of the ejection of electrons from specific orbits of an atom.[36] It is this aspect that the EDS system utilizes when generating the sample composition information.   The detector is designed such as to minimize the interference of the background x-rays and acquire a spectrum from 0 eV up to over 30 eV.[36] Backscattered electrons occur when the primary electron beam interacts with the sample in such a way that instead of being absorbed into the sample, it instead escapes the sample. These interactions maintain most of the original energy of the electron beam and are used for imaging samples that want relative atomic density combined with topographical data.[8]

Secondary electrons occur when the primary electron is absorbed into the sample, and a lower energy secondary electron is then emitted from the sample. The energy of the secondary electrons is very low, so only those interactions that occur near the reaction vessel surface are measured.[36,37] Still, there are two very important uses for selecting the secondary electron mode when using the SEM instrument: high resolution and excellent topographical information can be obtained.[8] This is because multiple secondary events can occur with each primary event; therefore creating an increased signal, thus better

imaging. In this work, both backscattered and secondary electron images were obtained. Typically, the secondary images were the most clear.

2.5.1 SEM/EDS Sample Analysis Details

SEM and EDS measurements of uranium and samarium electrochemical deposits were obtained using a JOEL JSM-5610 instrument and an Oxford ISIS EDS system with a tungsten filament. All samples were deposited onto gold or GC electrode surfaces. The electrodes were cleaned and prepared in the same matter as for the ICP-MS laser ablation analysis (see Section 2.4.3). Samples for SEM examination must be electronically conductive; however the electrode surfaces are by nature conductive, so no further preparation was required for analysis.   The electro-deposition of various f-element species and the SEM images and EDS results are presented in Chapters 4, 5, and 6.

2.6 X-Ray Diffraction

X-ray diffraction (XRD) is a very useful tool that is compatible with any solid that has crystalline characteristics.[38] From this tool, information about the specific chemical composition and structural orientation can be obtained. All compounds can be described by their crystal lattice structure, the arrangement of the atoms in three dimensional space. The atoms are ordered in a series of repeating planes, with a distance, d, between them.[38] The distance will be different for each material. There are multiple planes in every

crystalline material with their own orientation and distance between them. This is referred to as d-spacing (Figure 2.9).[38]
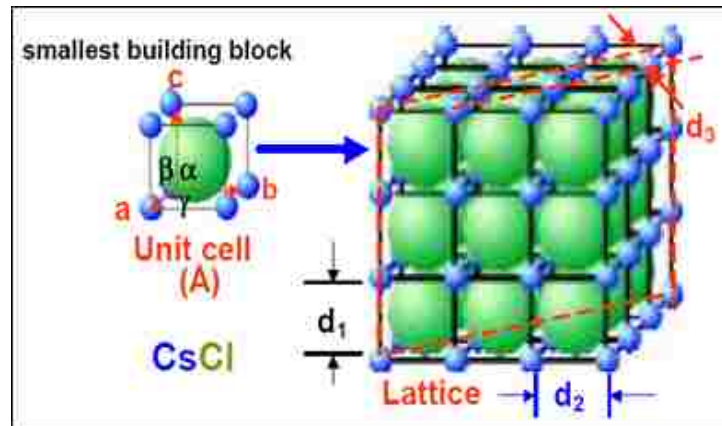
Figure 2.9. Crystal unit cell.

When a monochromatic x-ray beam targets this crystalline solid, it is diffracted when the distance between the x-rays and the planes of the material are different by n wavelengths, this relationship is described by Bragg's law: [38]

$$n\lambda = 2d\sin\theta \qquad \text{Equation 2.10}$$

Where: n = wavelength integer
λ = wavelength of the incident beam
d = distance between planes
θ = angle of the incident beam

The d-spacing of the crystalline material can then be obtained by varying the angle of the incident X-ray beam. A plot can be created with the angles, intensities, and positions obtained during analysis, and a diffraction pattern can be created that will be characteristic of the specific sample being analyzed (Figure 2.10).[38]

33
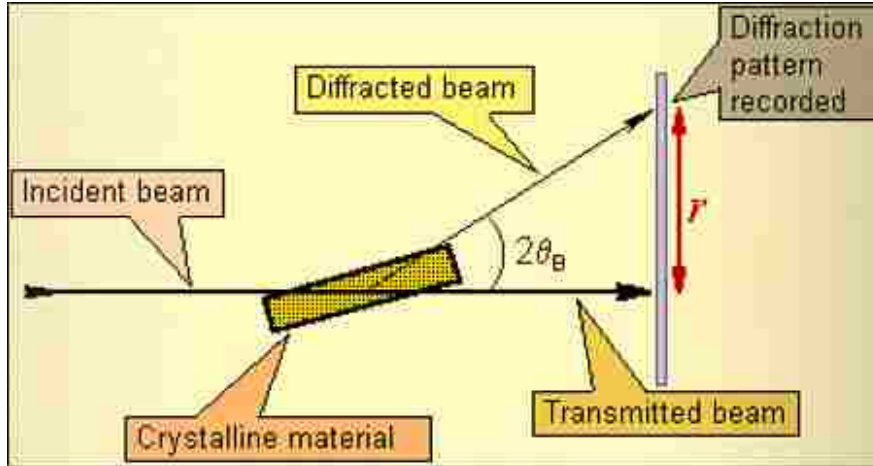
Figure 2.10. XRD sample and detector arrangement.

2.6.1 Powder XRD Instrument Parameters

Powder XRD measurements were taken using a PANalytical X'PERT Pro X-ray

Difraction Spectrometer with the following settings:

Table 2.2. Powder XRD parameters

1	Power:	40 kV/40 mA
2	θ Range:	34 to 58 degrees
3	Steps:	0.05 degrees
4	Slit size:	0.1 mm (receiving)

   The measurements were refined using a lattice parameter including a 2nd order

spherical harmonics texture model. This modeling method can be used to obtain

orientation and particle morphology details.[39] For example, in Section 6.3.1, the XRD

analysis of uranium metal is presented. The determination of the presence and phase of the uranium was made using this method.

2.6.2 XRD Electrode Sample Preparation

Only gold electrodes were analyzed with this technique. They were prepared inside of an argon filled glove box in the same manner as laser ablation (see Section 2.4.3). The electrodes were mounted in the sample holder using putty. The sample holder cap was sealed with vacuum grease and a sheet of plastic tape was placed inside of the sample holder to protect the air sensitive samples (Figure 2.11). After the electrodes were mounted, they were sealed inside a secondary container and taped closed during transport. After transport they were opened and immediately placed onto the powder XRD instrument. The electro-deposition of uranium onto the gold electrodes and the results of the powder XRD analysis are presented in Chapter 6.
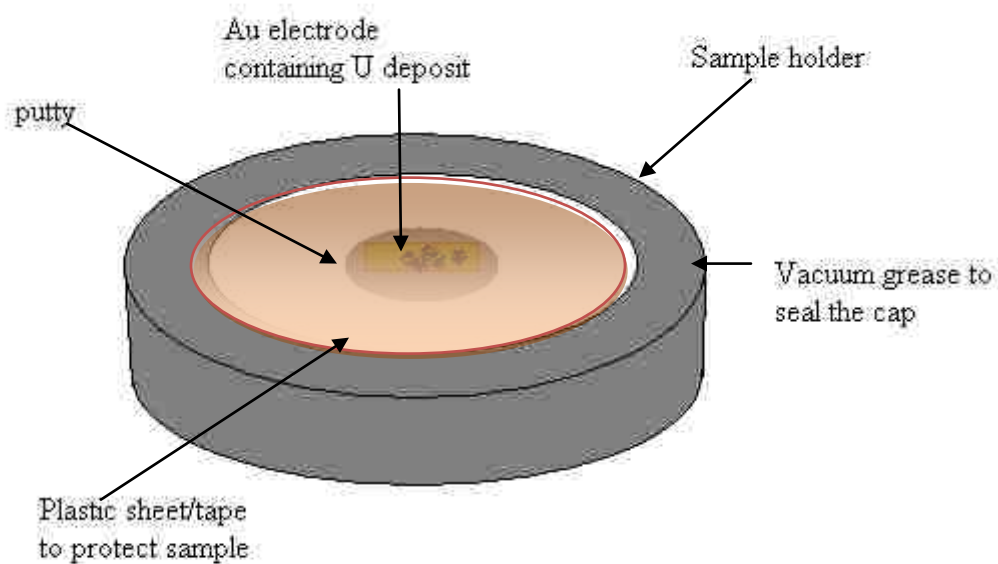
Figure 2.11. XRD Sample holder containing Au electrode

2.6.3 Single Crystal XRD Instrument Parameters

Single crystal XRD measurements were taken using a Bruker Apex II single crystal diffractometer with the following settings:

Table 2.3. Single crystal XRD parameters

1	Power:	60 kV/300 mA
2	θ Range:	20 to 80 degrees
3	Steps:	0.05 degrees
4	Slit size:	0.3 mm (receiving)
		0.1 mm (diverging)

2.6.4 Single Crystal XRD Sample Preparation

The $Sm(TFSI)_3(H_2O)_3$ crystal synthesis procedure is presented in Chapter 3. The crystals were prepared for XRD by removing a small sample and placing it on a slide in paratone oil. A single crystal suitable for analysis was then selected, mounted onto a glass fiber, and placed immediately onto the XRD instrument for analysis.

2.7 X-Ray Absorption Fine Structure

X-ray absorption fine structure (XAFS) is an extremely useful method that can provide information on the coordination, oxidation state, and identity of atoms bound to a known element.[40] Following X-ray excitation of sufficient energy, a core shell electron can be excited to an unoccupied state. This method is typically used at synchrotron sources where the energy of the X-rays can be tuned to the specific energy of the shell that information is desired from, often known as the absorption edge.[41] A double crystal monochromator is utilized to select the correct energy for absorption edge of the element of interest.[40] The resulting spectra can be categorized into two areas: X-ray Absorption Near Edge structure (XANES) and Extended X-ray absorption Fine Structure (EXAFS). These two regions together are often referred to as XAFS (Figure 2.12).
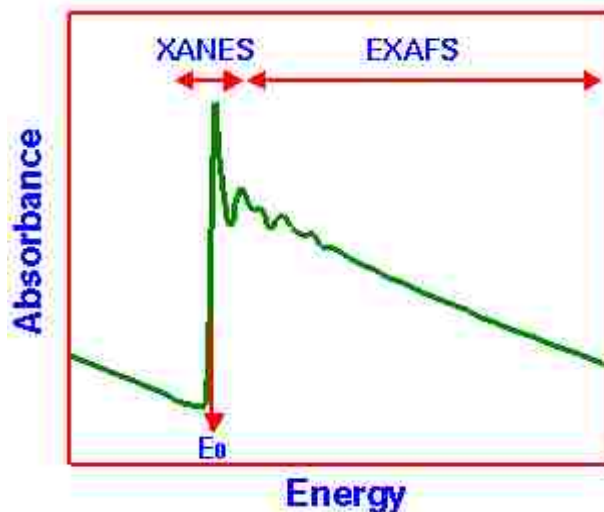
Figure 2.12. XANES and EXAFS regions in an XAS spectrum.[40]

The XANES region is very sensitive to oxidation state and the coordination around the atom of interest.[40] This area in the spectrum extends from the initial energy to approximately 50 eV past the absorption edge. The position of the absorption edge can be used to determine the oxidation state of the atom of interest.[40] This technique was utilized in the analysis on the UO_2 deposited electrode presented in Chapter 5.

The EXAFS region provides information regarding the identity, coordination, and distance of the neighbors surrounding the absorbing atom.[41] In this area, the photoelectrons have transitioned to continuum states. As a result of the energy in this region, backscattered electrons are created from the atom's neighbors. The amplitude of the backscattered electrons when they reach the absorbing atom is energy dependant.[40,41] The result is oscillations in the XAFS spectrum that can be used to determine information regarding the absorbing atom's neighbors.[41] This technique was also applied in the UO_2 electrode analysis in Chapter 5. A more comprehensive review of XAFS techniques can be found in the literature. [40,41]

2.7.1 XAFS Sample Preparation

The electrode sample was prepared by scraping the surface of the electrode to remove the deposit. The sample was affixed to 0.25 μm kapton tape and mounted in an aluminum sample holder. The method of electro-deposition is described in Sections 5.6 and 6.5.

Liquid samples were analyzed using custom-made aluminum liquid sample holder boxes. Several air-sensitive uranium solutions were prepared for analysis (see Chapter 6). After the box was assembled, clear coat nail polish was used to further seal the box from open air (Figure 2.13).

Figure 2.13. XAFS representative liquid sample holder

2.7.2 XAFS Sample Analysis Details

XAFS measurements were performed at the Advanced Photon Source (APS) at the BESSRC-CAT 12 BM station at Argonne National Laboratory. The XAFS spectra were recorded at the U-L_{III} edge (17,166 eV) in fluorescence mode at room temperature using a 13 elements germanium detector. A double crystal of Si [1 1 1] was used as a monochromator. The energy was calibrated using an Yttrium foil (K edge = 17,038 eV). For each sample, four spectra were recorded in the k range [0 - 14] $Å^{-1}$ and averaged. Background contribution was removed using Athena software and data analysis was performed using Winxas. For the fitting procedure, amplitude and phase shift function were calculated by Feff8.2. Input files were generated by Atoms using crystallographic structures of the uranyl hydroxides and UO_2.[42,43] Adjustments of the k^3-weighted XAFS spectra were performed under the constraints $S_0^2 = 0.9$. A single value of energy shift (ΔE_0) was used for all scattering; all the other parameters were allowed to vary.

2.8 Voltammetry

Each of the techniques described in this work rely on the underlying concept that the oxidation states of materials can be probed using an applied voltage. In an electrochemical system, the energy of formation can be evaluated and utilized to observe specific oxidation states under solution based conditions.[44,45] These formation energies

can be obtained, and then utilized to electrochemically deposit a solid species out of the solution and onto the working electrode.

2.8.1 Cyclic Voltammetry and Linear Sweep Voltammetry

Cyclic voltammetry (CV) utilizes a technique in which the voltage is applied to a solution and the current is measured as a response to changes in the voltage over time.[44] The potential begins at an initial voltage, a, and is swept first towards a negative potential, b, then back to a positive voltage, c, and then finally, returns to the initial voltage, a (Figure 2.14).
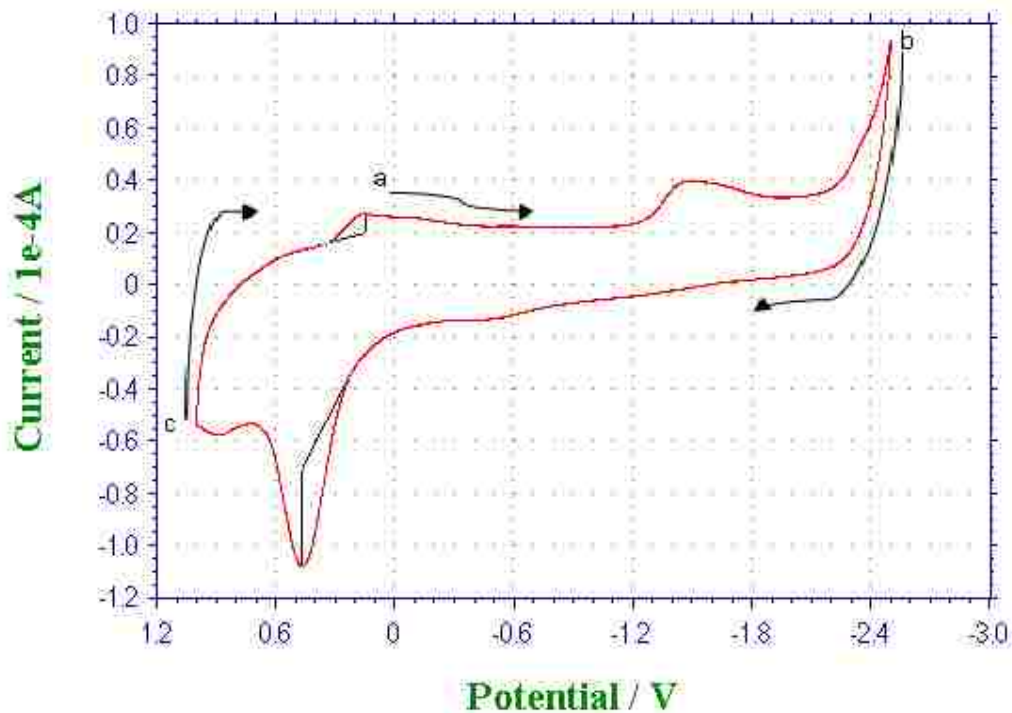
Figure 2.14. Representative screen display during CV of U(TFSI)$_3$ in the RTIL solution. The arrows indicate the direction of the potential as it is repeatedly scanned from points a through c.

41

The current is measured as the potential is varied in this cyclic manner. This type of electrochemical experiment allows for the observation of redox couples in which the oxidation and the reduction of the species of interest can be analyzed.[44] These redox reactions can be as a result of electron transfer reactions or from potential mediated chemical reactions. In the latter example, the applied potential provides the needed energy to drive the chemical reaction. In this case, ligands can be displaced, and new complexes formed during the electrochemical reaction.[44] The current peaks that are viewed during CV experiments are caused as a result of a diffusion layer forming near the surface of the electrode when the current is applied.[44,45] Over time, the measurements obtained will represent the bulk solution, and analysis can be executed with regard to the type of reaction that is taking place. Specifically, in CV, insight into whether an oxidation and reduction mechanism is reversible, quasi-reversible, or irreversible can be found based on the Nernst Equation.[44] In the case of Equation 2.11, the Nernst Equation reflects that the energy in volts is proportional to the natural log of the concentration of the oxidized species divided by the concentration of the reduced species.[44,45]

When $O + ne \leftrightarrow R$

$$E = E^o + \frac{RT}{n\text{F}} \ln\left(\frac{C_o^*}{C_R^*}\right)$$

Equation 2.11

Where: O = oxidized
          R = reduced
          E = energy, V
          R = molar gas constant, 8.31447 J mol^{-1} K^{-1}
          T = temperature, K
          F = Faraday constant, 9.64853×10^{-19} C

The reversibility of the system can also be related to the Randles-Sevcik equation:

$$i_p = (2.69 \times 10^5) n^{3/2} \text{ACD}^{1/2} v^{1/2}$$

Equation 2.12

Where: i_p = peak current
          n = number of electrons
          A = electrode area
          C = concentration
          D = diffusion coefficient
          v = scan rate

If the above equations (Equation 2.11 and 2.12) hold true, then the system can be referred to as reversible. If neither are valid, then it is inferred that the system is irreversible. If one is true, but the other is not, then it is quasi-reversible.[44] In electrochemical reactions, the rate of the electron transfer between the working electrode and the species being reduced in solution defines whether the system is electrochemically reversible. When the electron transfer process happens quickly, the system is said to be reversible. When the electron transfer process happens slowly, the process is defined as irreversible. Finally when the electron transfer rate is neither slow nor fast, the reaction is quasi-reversible.[44] This relationship can be evidenced by deviation from the above equations, which were derived under reversible conditions. The above description explains the most basic underlying concepts. A more thorough explanation on the fundamental theories that govern the electrochemical reactions is presented elsewhere.[44,45]

In the case of reversible electrochemical adsorption, the following relationship is used:[44]

$$i_p = \frac{n^2 F^2 \Gamma A v}{4RT}$$

Equation 2.13

Where: Γ = surface coverage

All remaining terms are defined above

The theory behind Linear Sweep Voltammetry (LSV) is the same as that for CV, with the exception that the sample is only probed in one direction for one scan.[44] Simply put, LSV is half of a CV experiment. While this does not give information regarding the reversibility of a system, it can be utilized to observe the effects of electrodeposition on the surface of the electrode.[44] When the current is set sufficiently negative such that a deposit can be made with each scan, then changes to the surface of the electrode will be observed with each successive scan. For example, in chapter 5 of this work, real-time observations were made as a glassy carbon electrode was changed to a uranyl electrode through electrodeposition. The subsequent voltammetry was altered after the electrode's surface was changed. This can give insight into whether the potential mediated deposition is favored at the original electrode, or on an electrode that already contains the material to be deposited.[44] Specifically, LSV can yield valuable information on the *optimal conditions* for obtaining deposition onto the electrode surface. Additionally, since the theory of LSV is the same as CV, oxidation and reduction reactions can be observed during the half-cycle as previously discussed above. The literature can be consulted for excellent reviews with further fundamentals of CV, LSV and Square wave voltammetry (SWV).[44,45]

2.8.2 Square Wave Voltammetry

Square wave voltammetry (SWV) is a difference technique that takes advantage of a square waveform that is superimposed over a staircase potential.[44] Essentially, the current is recorded twice for each wave cycle; once at the beginning, and once at the end (Figure 2.15). The difference of the current at these two points is then plotted against the applied voltage.
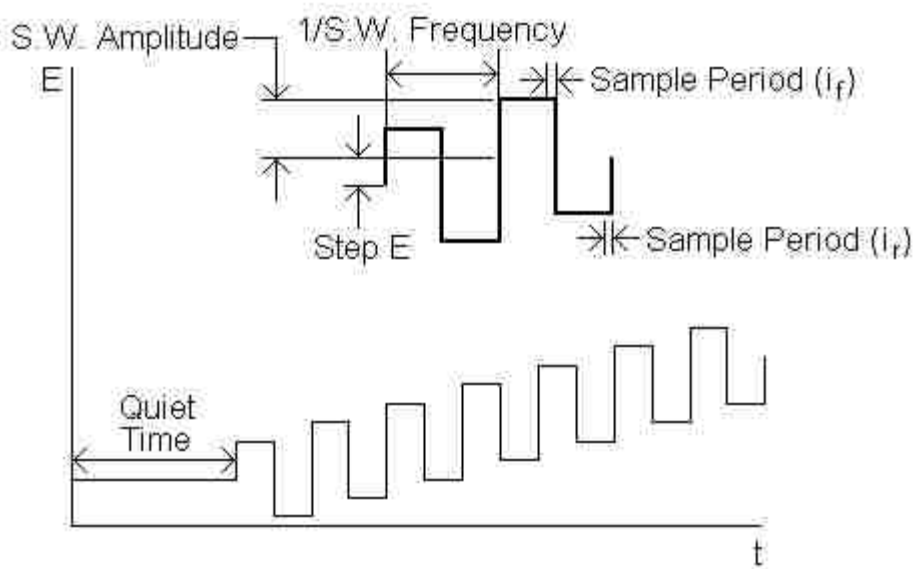
Figure 2.15. Square-wave form in SWV.

The peaks are proportional to the analyte concentration.[44] In addition, given that SWV is a subtractive method, there is a reduction in background interferences that may be evident in CV, thus this method can also be employed to de-convolute the redox peaks observed in CV.   The net current observed in the SWV technique is much larger and more symmetric than the corresponding CV current response because it is the difference

45

in current between the forward and reverse scans. As such, the SWV redox peaks are more resolved from one another. SWV has also been used in the literature for kinetic studies due to the ability to achieve a large number of scans very quickly.[44] The resulting data from the SWV analysis will reflect electrochemically driven reactions as mentioned in Section 2.8.1, specifically electron transfer reactions and electrochemically driven chemical reactions. In summary, one of the main advantages of SWV is a clearer picture of the peak locations as a result of the *more resolved peaks* obtained from this technique. Additionally, the *concentration of the species in the solution* can be obtained from observing the maximum peak current for any given redox reaction.[44]

2.8.3 Reference Electrode

Previous reference electrodes were standardized in aqueous based systems, and thus there is an unknown solubility of the reference redox couples in RTIL solutions. Based on published RTIL work by Saheb et al, a non-aqueous Ag/Ag^+ reference electrode is utilized in all work examined in this dissertation.[46] By using the Ag/Ag^+ electrode in contact with a soluble salt such as silver nitrate, the reference electrode's potential no longer is dependent on the electron transfer process at the interference, scan rate, or potential range; all of which could be affected by the adsorption of species at the working electrode.[46] The Ag/Ag^+ reference has a known potential versus the ferrocene/ferrocenium couple.[44] After measuring the potential for ferrocene in the $[Me_3^nNBu][TFSI]$ RTIL using the Ag/Ag+ reference electrode with a gold working electrode, $E^{'}$ was determined to be -0.173 V. The published value is +0.400 V versus

NHE. The adjustment from Ag/Ag+ to NHE scale was then calculated to be +0.573 V. This process was repeated for platinum and glassy carbon working electrodes, and the offset was unchanged at +0.573 V in those cases as well. This was the conversion utilized for all experimental results contained in this dissertation.

2.8.4 Electrochemical Cell Design and Preparation

In all voltammetry experiments, a three-electrode set up is employed (Figure 2.16). The system was composed of a glassy carbon disc electrode (3 mm diameter) or gold sheet working electrode (1 cm x 1 cm), a Ag/Ag$^+$ (0.1M AgNO$_3$ in MeCN) non-aqueous reference electrode,[46] and a platinum sheet counter electrode (1.25 cm x 1.25 cm).
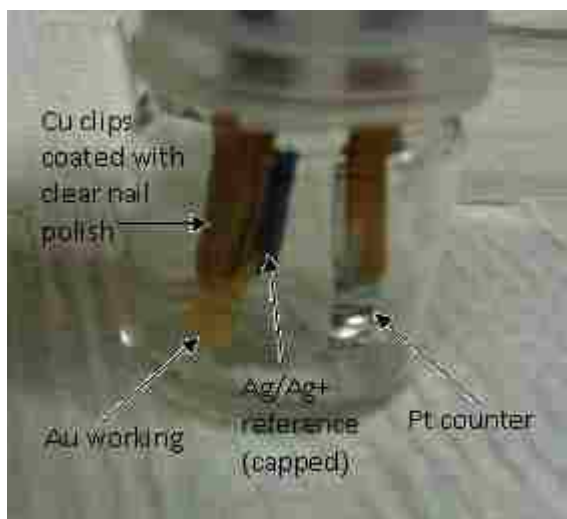
Figure 2.16. Three electrode electrochemistry cell used in experiments.

The working electrodes were freshly cleaned and polished prior to each use. The Reference electrode was not re-used for more than one experiment set. In between any

change in solution conditions, the electrode glass tube was cleaned, the fill solution was replaced, and a fresh vicor tip was attached.   The counter electrode was also cleaned and fired with a torch prior to each use. All electrochemical measurements were made using a CH Instruments CHI 770 bipotentiostat.

2.8.5 Electrochemical Experimental Conditions

For all work the same cell design was utilized as sited above. The solution was added to the analysis cell, and the electrodes were carefully inserted. Many of the experiments utilized low volumes of solution down to 1.0 mL, and this created a unique situation where migration of the solution up the electrode and onto the electrode clips was observed. To prevent this from re-occurring, the cells were coated with clear nail polish on all exposed locations.

All work for Chapters 4 and 5 was performed on the bench-top with no additional changes. The experiments for Chapter 6 were executed inside of an argon filled glove box. Initially, these trials were performed inside of a Labconco glove box that had no output/input ports for the electrochemical cell wire housing. As a result, the entire setup was moved into the glove box (Figure 2.17).

Figure 2.17. Electrochemical setup in the Labconco glove box.

While the equipment did operate, the electronics generated a substantial amount of heat. This caused overheating to the computer, which in turn would shut down during the voltammetry experiments. As a result of this, the temperature had to be carefully monitored. Whenever the temperature exeeded ~35 ^{o}C, the electronics were powered off until the conditions inside of the box returned to ~ 25 ^{o}C. Later studies were repeated using an MBRAUN glovebox that enabled the electrochemical wiring to be inserted through a custom made air-tight plate that fit into the pre-installed MBRAUN input ports. Moving the computer outside of the glovebox resolved the overheating issues, but did not alter the potentials at which the oxidation and reduction processes were observed.

Chapter 3: Synthesis

3.1 Room Temperature Ionic Liquid Synthesis

3.1.1 Materials

All reagents used in the synthesis of the ionic liquid were reagent grade. Lithium bis(trifluoromethanesulfonyl)imide (Li(TFSI)) salt was purchased from VWR. The N,N-Dimethyl-n-butylamine (Me_2N^nBu) and the Methyl Iodide (MeI) were purchased from Sigma Aldrich. All purchased reagents were used as received.

3.1.2 Synthesis of [Me₃NⁿBu][TFSI]

The synthesis was based on the procedure by Bhatt, et al.[47] A 0.72 mol (100 mL) sample of Me_2N^nBu was removed from the refrigerator and placed into a salted ice bath. Over the course of 2 hours, 0.72 mol (45 mL) of MeI was added drop-wise through a column with constant stirring of the resulting mixture. A 100 mL sample of diethyl ether was added to the white precipitate, forming a suspension. Upon addition of 100 mL water, an aqueous and organic phase formed. The layers were separated using a separatory funnel, and the excess aqueous solvent was then removed under vacuum and gentle heating. After 3 hours, a white solid, $[Me_3N^nBu]I$ (169.5 g) was obtained. The solid was dried in a freeze dryer overnight to ensure accurate yield before combining with the anion.

The product, $[Me_3N^nBu]I$, was then dissolved into 10 mL of DI water and 0.703 mol of Li[TFSI] was added. The anion and cation water solutions were then combined into one vessel. The resulting biphasic mixture was then separated using extraction techniques. Frequently, a separatory funnel is employed such that the organic phase can be readily separated from the aqueous phase.[48] These techniques were somewhat modified, as the organic layer was the lower phase; so standard extraction vessels were impractical due to the viscosity of the RTIL solvent. When use of the separatory funnel was attempted, the organic lower phase RTIL clogged the small opening in the vessel, preventing the extraction from proceeding. Instead, the majority of the water was initially removed by decanting. Next, the RTIL was removed with a wide mouthed disposable pipette. To remove any remaining excess iodine, the product RTIL layer was then washed with sodium thiosulfate and DI water. The RTIL, $[Me_3N^nBu][TFSI]$, was then dried with sodium sulfate. The solution was then passed through a column of activated alumina to remove any remaining excess iodine and water.[12] Finally, the RTIL was placed under a vacuum and gently warmed overnight to ensure full removal of any remaining un-reacted reagents and water. The combination of purification techniques described above was based on a thorough review of the literature and multiple refinements to obtain the purest product possible.[12,28,11,10]

The final product $[Me_3N^nBu][TFSI]$ was characterized via IR-spectroscopy (Figure 3.1). All anticipated IR-active functional groups were evident in the spectra (Table 3.1). The bands were labeled using published values in Figure 3.1 to reflect the functional groups that they represent.[48,49] Several batches were made in this manner, and the IR-spectra were used to not only to identify successful synthesis, but also to ensure

that the batches were reproducible. Successful batch reproducibility for this work was primarily indicated by the band maxima occurring at the same wavelength. For all three batches, the maxima were found to occur at consistent wavelengths (Table 3.1).

Table 3.1. Comparison of synthesized RTIL batches IR spectral bands.

Functional Group	Wavelength (cm^{-1})			
	Batch 1	Batch 2	Batch 3	Literature[48,49]
CH_2 and CH_3	1495	1493	1492	1470
	1481	1481	1483	1465
SO_2	1346	1346	1344	1334
	1329	1329	1327	1324
CF_3	1180	1179	1173	1195
SO_2	1134	1132	1132	1138
SNS	1051	1051	1049	1062
CH_3	972	972	972	969
	932	931	932	953
	910	908	908	947
CS	789	789	789	797
SNS	764	764	762	771
CF_3	741	741	741	741
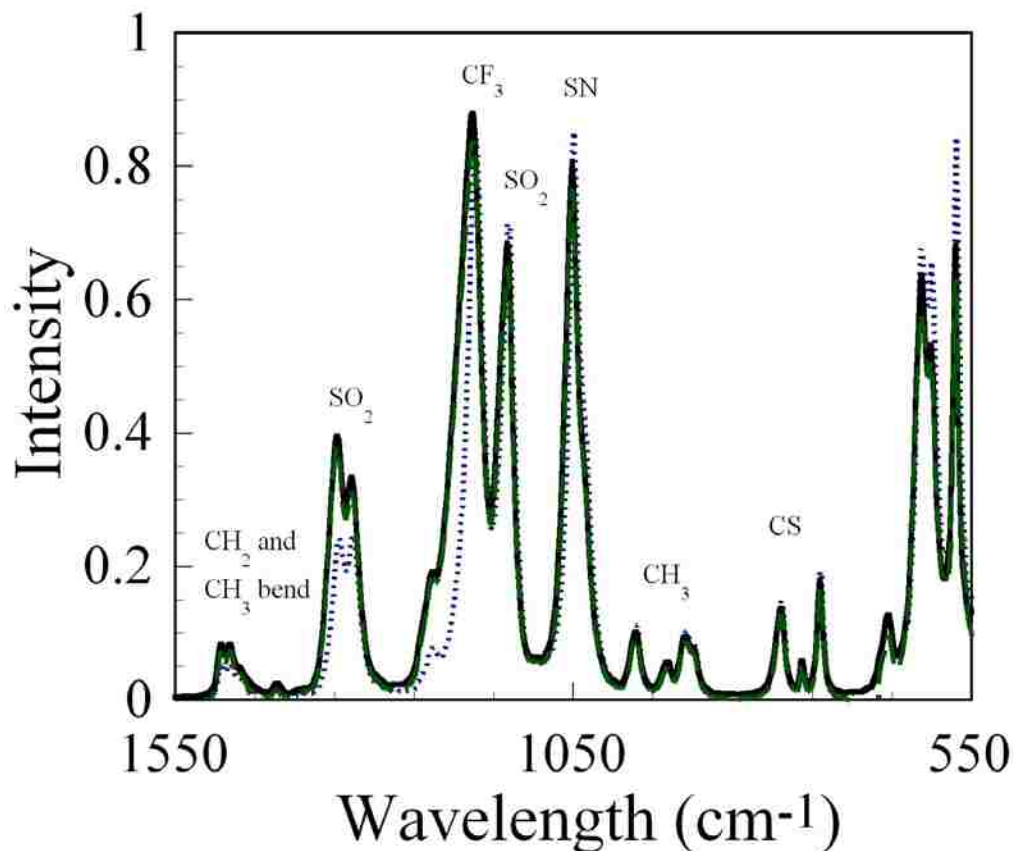
Figure 3.1. IR spectrum of several batches of neat [Me$_3$N^{n}Bu][TFSI]. Batch 1 is the black solid line, batch 2 is the green dashed line, and batch 3 is the blue dotted line. The functional groups responsible for the bands are labeled in the figure.

Following synthesis of each batch, the product was dried and weighed. The initial starting quantities were used to calculate the expected product as demonstrated below.

$$[Me_3N^nBu]I + Li[TFSI] \xrightarrow{H_2O} [Me_3N^nBu][TFSI] + LiI$$

0.703 mol   0.703 mol   0.703 mol
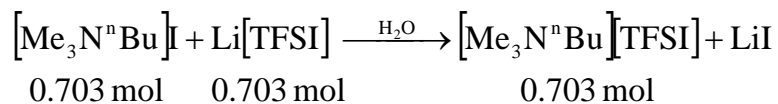
Theoretical Yield :

$$0.703\,\text{mol}\left(\frac{394.85\,\text{g}}{\text{mol}}[Me_3N^nBu][TFSI]\right) = 277.58\,\text{g}$$

Percent Yield :

$$\frac{\text{Actual yield}}{\text{Theoretical yield}} * 100\% = \%\ \text{yield}$$

$$\frac{166.5\,\text{g actual yield}}{277.58\,\text{g theoretical yield}} * 100\% = 60.0\,\%\ \text{yield}$$

This was compared to the final measurement, and a percent yield was determined as shown in Table 3.2.   Each synthesis yielded approximately 60% product after purification.

Table 3.2. RTIL Batch Yields

Batch	Actual Yield	Theoretical	% Yield
1	166.5	277.6	60.0
2	164.6	260.4	63.2
3	161.1	280.1	57.5
		Average	60.2

In addition, for many studies, the amount of water in the system is of interest. A common technique for determining water concentration in a sample is via coulometric Karl Fischer Titrations. In this method, the titration cell is divided into two

compartments. The first compartment contains an anodic solution consisting of sulfur dioxide, imidazole, and iodide in a methanol solution. The sample is injected into the smaller, cathodic compartment. Iodine is then created in an electrochemical reaction in the cell. Any water that comes in contact with the iodine will be titrated until there is no remaining water. The quantity of water is determined by the instrument software by measuring the amount of current that was required to generate the iodine.[50] The water content in the [Me$_3$N^{n}Bu][TFSI] was analyzed with five replicate Karl Fisher titrations. The data from the experiment is shown in Table 3.3.

Table 3.3. Karl Fisher Titration data

Titration	% Water
1	0.285
2	0.290
3	0.283
4	0.281
5	0.286
Average	0.285
Standard Deviation	0.003
Relative Error	0.012

From the data, the RTIL was determined to contain 0.285 ± 0.012 mass % water content.

3.2 Uranyl Carbonate Synthesis

3.2.1 Materials

Uranyl nitrate was obtained from a standard stock in the UNLV Radiochemistry program. This stock is comprised of material that was recycled and obtained from other

universities. The RTIL, [Me$_3$N^{n}Bu][TFSI] was synthesized in this work (see Section 3.1). Sodium carbonate was purchased from VWR.

3.2.2 Synthesis of uranyl carbonate, UO$_2$CO$_3$

The synthesis of the uranyl carbonate was based on previous literature.[51] A 240 mg sample of uranyl nitrate composed of 180 mg ^{238}U and 60 mg of ^{233}U was placed into 50 mL of DI water. These quantities were intentionally selected to obtain a yield a 25% ratio of ^{233}U in the product uranyl carbonate. The final percent composition of each isotope was experimentally determined to be 12.2% ^{233}U. This analysis is described later in this section. The solution was then adjusted from pH 2 to a less acidic condition of pH 5 via slow addition of sodium carbonate with constant stirring. The pH was selected based on published ranges to favor the formation of the mono-carbonate species.[52] The solution was purged with CO$_2$ gas for one week to ensure sufficient time for reaction completion. The resulting solid pale yellow precipitate, UO$_2$CO$_3$, was then separated and freeze dried for 24 hours. An IR spectrum identified the resulting solid as the desired mono uranyl carbonate product (see Section 3.2.3, Figure 3.3).

To verify the composition of ^{233}U and ^{238}U isotopes, a 25.0 ± 0.1 mg solid sample of UO$_2$CO$_3$ product was dissolved into 10 mL of 10% HNO$_3$. A 50 μL aliquot of the sample was then removed, weighed (to reduce volumetric errors), and LSC cocktail was added with a final volume of 20 mL. This solution was then analyzed using liquid scintillation counting. The calculation steps below were taken to determine the percentage of each uranium isotope in the final product:

3. The efficiency was determined to be 100% (see Section 2.3.1), so that

   CPM=DPM: 231200 CPM = 231200 DPM

4. This was then converted to activity in Becquerel (Bq): DPM/60 = Bq:

$$\frac{231200}{60 \, ^{s}\!\big/\!_{min}} = 3853.33 \text{ Bq}$$

5. Using A = λN, the moles of ^{233}U in the sample was determined:

$$\lambda_{233U} = 1.38 \times 10^{-13} \, s^{-1}$$

$$\left(\frac{3853.33 \text{ Bq} \cdot s^{-1}}{1.38 \times 10^{-13} \, s^{-1}}\right)\left(\frac{\text{mol}}{6.02 \times 10^{23} \text{ atoms}}\right) = 4.64 \times 10^{-8} \text{ mol}_{233U} \text{ in } 50 \times 10^{-6} \text{ L solution}$$

$$\frac{4.64 \times 10^{-8} \text{ mol}_{233U}}{50 \times 10^{-6} \text{ L}} = 9.27 \times 10^{-4} \text{ M}_{233U}$$

Original sample volume $= 10$ mL

$$10 \times 10^{-3} \text{L}\left(\frac{9.27 \times 10^{-4} \text{ mol}_{233U}}{\text{L}}\right) = 9.27 \times 10^{-6} \text{ mol}_{233U}$$

4. The ratio of ^{233}U to ^{238}U present in the UO_2CO_3 sample was calculated:

$$9.27 \times 10^{-6} \text{ mol}_{U^{233}} = 9.27 \times 10^{-6} \text{ mol } ^{233}UO_2CO_3$$

$$9.27 \times 10^{-6} \text{ mol}_{233\,UO_2CO_3}\left(\frac{325.005g}{\text{mol}}\right) = 3.01 \times 10^{-3} \text{ g } ^{233}UO_2CO_3$$

$$25.0 \times 10^{-3} \text{ g } UO_2CO_3 - 3.01 \times 10^{-3} \text{ g } ^{233}UO_2CO_3 = 2.20 \times 10^{-3} \text{ g } ^{238}UO_2CO_3$$

$$2.20 \times 10^{-3} \text{ g } ^{238}UO_2CO_3\left(\frac{\text{mol}}{330.055g}\right) = 6.66 \times 10^{-5} \text{ mol } ^{238}UO_2CO_3$$

$$\frac{9.27 \times 10^{-6} \text{ mol } ^{233}UO_2CO_3}{9.27 \times 10^{-6} \text{ mol } ^{233}UO_2CO_3 + 6.66 \times 10^{-5} \text{ mol } ^{238}UO_2CO_3} = 0.122 = 12.2\%$$

The experimentally determined ratio of ^{233}U was then found to be 12.2%. While this

value was lower than the experimental design would have suggested (the synthesis was

designed for a 25% ^{233}U ratio), the liquid scintillation counting sample results were

repeatable. For all experimental result calculations, a ratio of 12.2% ^{233}U was utilized.

3.2.3 Spectroscopy of uranyl carbonate, UO$_2$CO$_3$

An IR spectrum was obtained of the resulting solid uranyl carbonate product

(Figure 3.2). The peaks can be assigned to the functional groups as listed in Table 3.4.
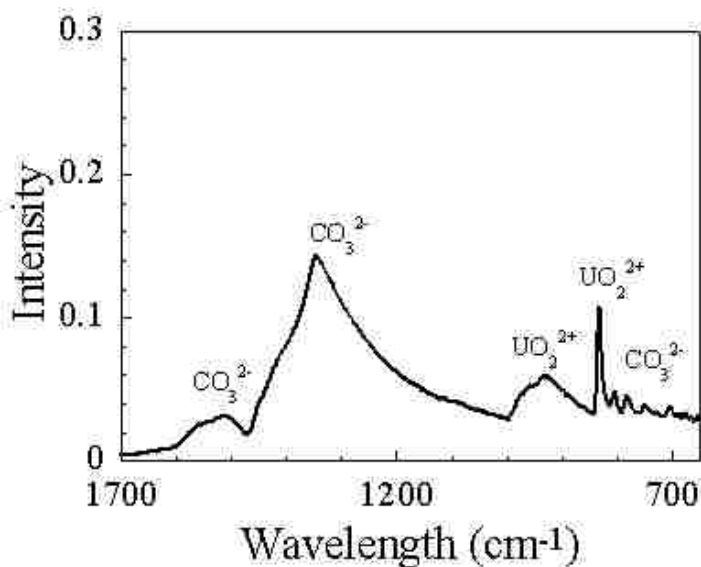
Figure 3.2. FTIR spectrum of solid UO$_2$CO$_3$

Table 3.4. IR assignments for solid UO_2CO_3.

Functional Group	Wavelength (cm^{-1})	
	Product	Literature[9,26]
CO_3^{2-}	1519	1522-1578
CO_3^{2-}	1348	1347
UO_2^{2+}	960	902-932
UO_2^{2+}	933	902-932
UO_2^{2+}	835	833
CO_3^{2-}	808	798-802
CO_3^{2-}	786	726-778
CO_3^{2-}	754	702-778
CO_3^{2-}	707	695-700

The spectrum was consistent with the published literature for the mono-uranyl species.[9,26]

3.3 Sm(TFSI)$_3$(H$_2$O)$_3$ Synthesis

3.3.1 Materials

Reagent grade chemicals were used in the synthesis. Samarium (III) oxide (Sm_2O_3) salt was purchased from VWR. The Bis(trifluoromethanesulfonyl) amine (HTFSI) was purchased from Sigma Aldrich. All purchased reagents were used as received.

3.3.2 Synthesis of Sm(TFSI)$_3$(H$_2$O)$_3$

A synthetic route was designed and followed according to the reaction scheme provided below:

$$Sm_2O_3 + 6HTFSI \xrightarrow{3H_2O} 2Sm(TFSI)_3(H_2O)_3$$
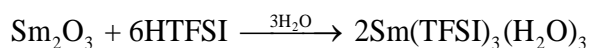
A 1.5 g sample of Sm_2O_3 and 7.3 g of H(TFSI) was placed in a beaker with 15 mL of H_2O. The resulting solution was stirred for 20 minutes, and then placed on the rotary evaporator with gentle heat (approximately $60^{\circ}C$) to remove any excess HTFSI and water. HTFSI has a boiling point of $91^{\circ}C$, which is lower than water, thus any excess of either material should be removed during this step.[53] After approximately 20 minutes, the majority of the excess solvent had been removed, forming an oil. Crystals began to form in the resulting yellow oil while still on the rotary evaporator. At this point, the oil was removed, and a single crystal was isolated for XRD analysis. The remaining oil was returned to the rotary evaporator to attempt to obtain a solid product. Despite this attempt, the product remained an oil with visible crystalline particles contained in the sample. The resulting $Sm(TFSI)_3(H_2O)_3$ was removed and cooled. After drying, the oily product yield was determined to be 85 percent (7.0 g).

3.3.3 Single Crystal XRD for Sm(TFSI)₃(H₂O)₃

Single crystals were placed in paratone oil. Although it was observed that they dissolved in paratone over the course of several minutes, a crystal was obtained and positioned on the tip of a glass fiber. This fiber was then quickly placed onto the diffractometer. The low temperature of the cryostream, which was cooled to 100 K, prevented further dissolution of the sample. The crystal initially indexed as a primitive cubic crystal with a cell parameter of 18.4517(7), comparable to Bhatt et al,[28] and a full sphere of data was collected. Systematic absences and intensity statistics indicated the

chiral spacegroup P2$_1$3, which was consistent with the structure previously encountered.[28] The structure was solved with SIR2004[54] within the WINGX program suite.[55]

Following structure solution, the model was refined against F^2 using SHELXTL.[56] For the two crystallographically distinct TFSI molecules, one refined with reasonable anisotropic displacement parameters while those parameters for the second TFSI ligand were large. The coordinating central N atom appeared to be disordered between two positions. Refinement at variable occupancy lead to two chemically reasonable positions at close to 50% occupancy. The occupancy was fixed at 50% for the final refinement cycles, and the very close values for the anisotropic displacement parameters for both sites suggest this is a very reasonable constraint. The rest of the molecule was allowed to remain on single sites, although the displacement parameters are somewhat large. The ability to locate and refine H atoms on the coordinated water molecules, along with a final R$_1$ of 1.63%, suggests a very accurate structural model in spite of the disorder. For the hydrogen atoms bound to water molecules, these were located in the Fourier map, and refined with the displacement parameter set to 1.2x that of the oxygen to which they were bound. Distances were restrained to 0.82 Å for the final refinement cycle. Refinement of the Flack parameter to essentially zero (-0.0005   +/- 0.0057) indicates that the crystal is homochiral. Refinement parameters are presented in Table 3.5.

The results of the single crystal analysis can be compared to those from Bhatt et al's analysis of La(TFSI)$_3$(H$_2$O)$_3$.[28] In both cases, the f-element is coordinated through the sulfonyl oxgens with a resulting six atom ring structure. They also observed the shorter bond distances of the lanthanum center as compared to the oxygen in the coordinated water. In this work, similar results were observed, with the bond lengths for

the Sm-O (W) of 2.3896(19) Å for each coordinated water. Longer bonds of 2.4639(18) to 2.4888(19) Å were found to exist when examining the Sm-O (TFSI) bond. Bhatt et al also stated that because the negative charge on the TFSI anion is not delocalized to any large quantity, it is not anticipated that TFSI would be strongly coordinating.[28] In reviewing the results from the analysis of the Sm-O (TFSI) and Sm-O (water), this assessment is supported by the longer Sm-O (TFSI) bond lengths.[57]

Table 3.5 Crystal data and structure refinement of $Sm(TFSI)_3(H_2O)_3$.

Empirical formula	Sm C6 H6 F18 N3 O15 S6
Formula weight	1044.85
Temperature	100(1) K
Wavelength	0.71073 Å
Crystal system	CUBIC
Space group	P2(1)3
Unit cell dimensions	a = 18.4517(7) Å a= 90°.
	b = 18.4517(7) Å b= 90°.
	c = 18.4517(7) Å g = 90°.
Volume	6282.2(4) Å^3
Z	8
Density (calculated)	2.209 Mg/m^3
Absorption coefficient	2.437 mm^{-1}
F(000)	4024
Crystal size	0.09 x 0.08 x 0.07 mm^3
Theta range for data collection	1.56 to 26.11°.
Index ranges	-22<=h<=22, -22<=k<=22, -22<=l<=22
Reflections collected	75185
Independent reflections	4186 [R(int) = 0.0431]
Completeness to theta = 26.11°	100.00%
Absorption correction	Semi-empirical from equivalents
Max. and min. transmission	0.7453 and 0.6087
Refinement method	Full-matrix least-squares on F^2
Data / restraints / parameters	4186 / 4 / 306
Goodness-of-fit on F2	1.067
Final R indices [I>2sigma(I)]	R1 = 0.0163, wR2 = 0.0400
R indices (all data)	R1 = 0.0171, wR2 = 0.0403
Absolute structure parameter	-0.001(6)
Largest diff. peak and hole	0.383 and -0.274 e.Å^{-3}

An ORTEP plot is presented in Figure 3.3 below.
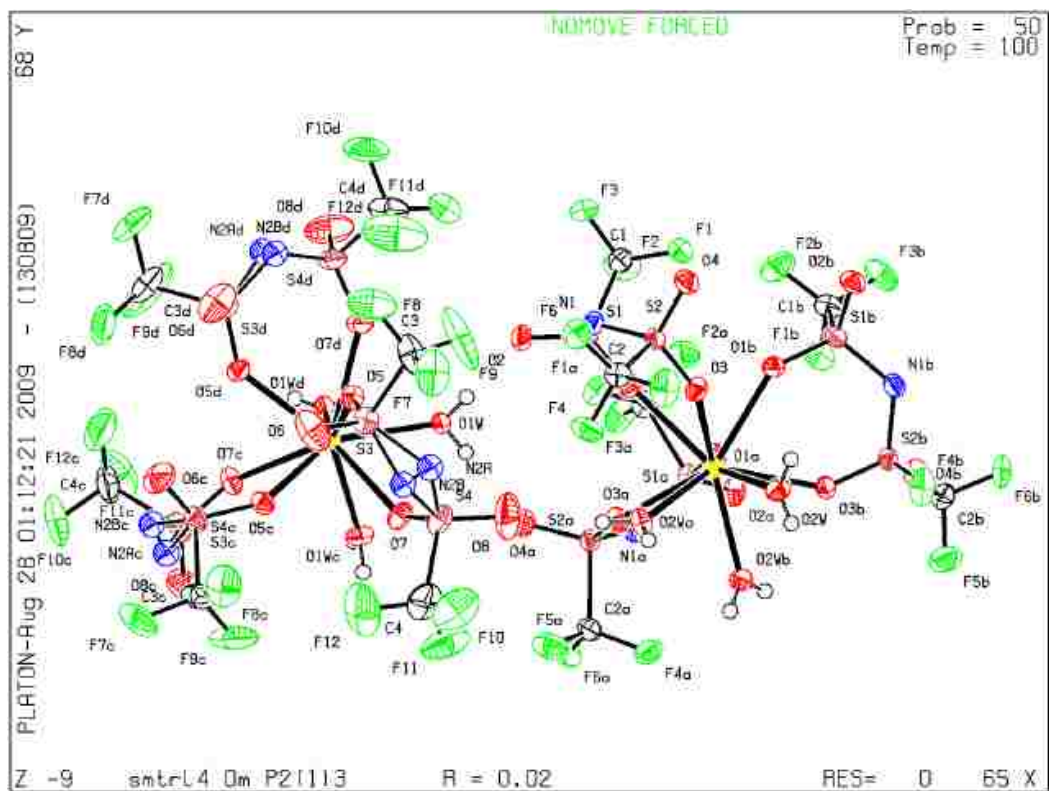
Figure 3.3. Structure of $Sm(TFSI)_3(H_2O)_3$

3.3.4 Spectroscopy of Sm(TFSI)₃(H₂O)₃

After obtaining the crystal structure of the $Sm(TFSI)_3(H_2O)_3$ product, the FTIR spectrum was acquired (Figure 3.4). Table 3.6 contains the assigned bands compared to the literature values.

Table 3.6. FTIR band assignments for 0.5 M Sm(TFSI)$_3$ in H$_2$O

Functional Group	Wavelength (cm^{-1})	
	Product	Literature[28]
OH	1641	1639
SO$_2$	1351	1323
SO$_2$	1327	1307
CF$_3$	1227	1221
CF$_3$	1206	1198
SO$_2$	1143	1138
SO$_2$	1138	1130
SNS	1059	1055
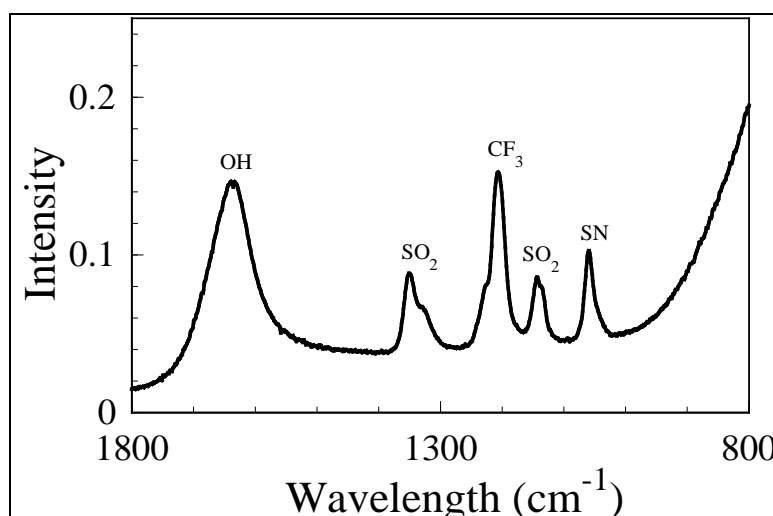
Figure 3.4. FTIR Spectrum of 0.5 M Sm(TFSI)$_3$ in aqueous solution

The Sm(TFSI)$_3$ sample was analyzed while in solution (concentration was 0.5 M), because of the acidity of the oil. The effects of the water are especially notable in the broad shoulder starting at 1000 cm^{-1}. By comparing the reported assignments to those of Bhatt et. al, it was found that this broad shoulder is hiding the additional SNS, CF$_3$, and SO$_2$ bands.[28] The Sm-O band is not IR active, and it was not observed in this spectrum.[28] The functional groups have been labeled in the figure, and the expected IR-active TFSI functional groups (SN, SO$_2$, and CF$_3$) are easily viewed in the spectrum, indicating the

presence of the Sm-TFSI complex in the aqueous solution.   The oily material was extremely acidic, so it was not measured on the FTIR instrument so as to not damage the solid press.

UV-Visible spectroscopy analysis was also utilized to further characterize the product $Sm(TFSI)_3(H2O)_3$. Three concentrations of $Sm(TFSI)_3$ aqueous solutions were prepared and examined. When the analysis was executed, the samarium product was a sticky oil; to remove it from the spatula, a small amount of water was used before the initial mass could be recorded. This was necessary to remove the sample from the spatula. As a result of this methodology, the following concentrations are approximate: 0.1 mM, 3.0 mM, and 4.5 mM. The spectra are presented in two separate figures, as the band at 264 nm is so large that it is difficult to observe changes in the bands above 300 nm when they are presented together. Figure 3.5 presents the full range of the spectra collected, and Figure 3.6 presents the spectra above 325 nm.
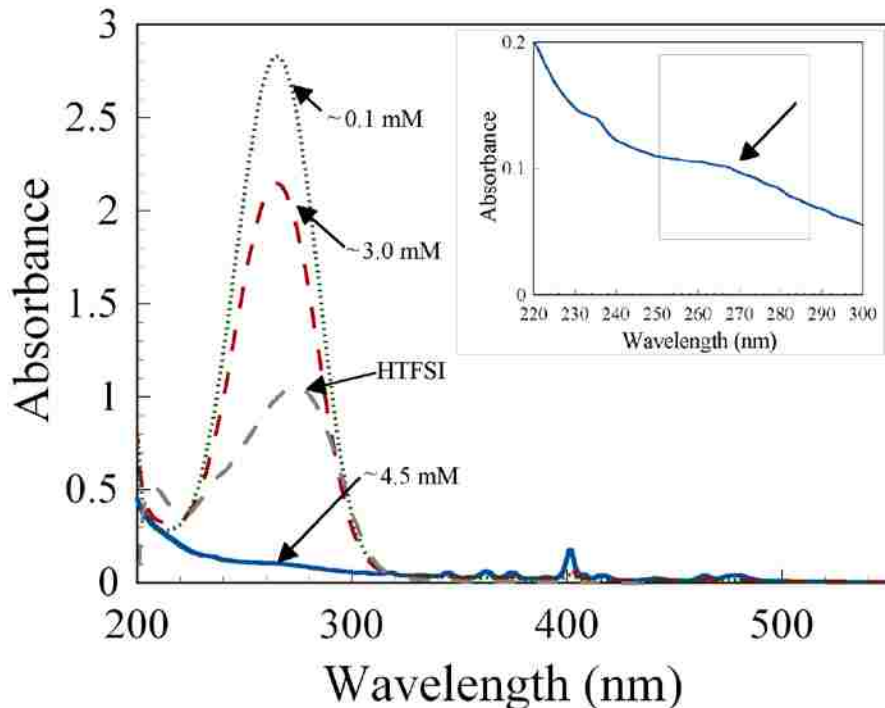
Figure 3.5. Sm(TFSI)$_3$ in H$_2$O as a function of concentration. The blue solid line is the initial ~4.5 mM Sm(TFSI)$_3$ sample, the red dashed line is ~3.0 mM Sm(TFSI)$_3$, and the green dotted line is ~0.1 mM Sm(TFSI)$_3$. The grey dashed line is HTFSI in H$_2$O. Inset is a blow-up for the region of 220 to 300 nm in the ~4.5 mM Sm(TFSI)$_3$(H$_2$O) sample.

In Figure 3.5, it can be seen that the band at 264 nm increases as the Sm concentration decreases (or conversely as the water concentration increases). Duluard et al performed a detailed analysis of lithium salvation in TFSI using Raman spectroscopy. In their observations, they noted a decreasing band with increasing cation concentration at 748 cm^{-1}, while the second band examined, at 748 cm^{-1} increased with increasing concentration. They attributed this finding to the quantity of free TFSI anion in solution as compared to coordinated Li-TFSI species.[58] Umebayashi et al found similar results when examining the band representing free TFSI at 744 cm^{-1} band, which decreased with increasing addition of the lithium cation. They also observed that the TFSI-Li band at 750 cm^{-1} increased as expected with increased lithium addition.[59] As the concentration of

66

water is increased, the availability of protons also increases Thus, in this work, the disassociation of the TFSI anion from the $Sm(TFSI)_3$ complex and subsequent formation of HTFSI could occur with increased quantities with the addition of water. To verify that TFSI does absorb in this region, HTFSI was dissolved directly into water, and measured (Figure 3.5, grey dashed line). It can be seen in the figure that there is a band for the HTFSI in the UV-Vis spectrum that is located at 268 nm in all cases (see inset for blow up of this region for the 4.5 mM sample). This band is then tentatively assigned to TFSI anion that has *dissociated* from the samarium complex and then subsequently formed the HTFSI complex. A detailed analysis of multiple TFSI species in water would prove useful in further confirming this band assignment, but this was outside of the scope of this work.
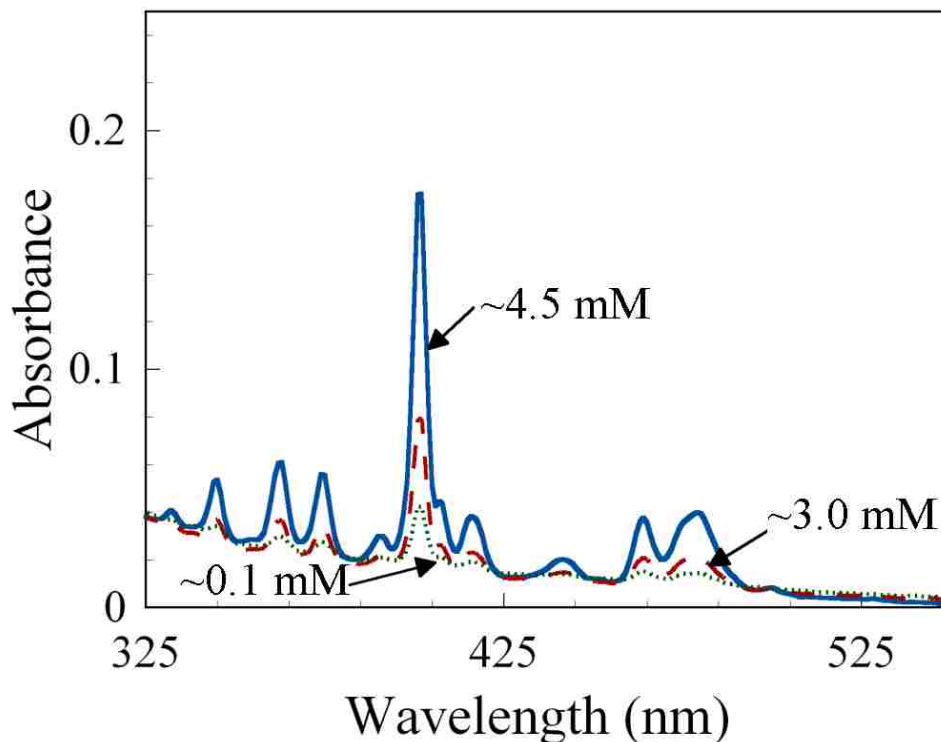
Figure 3.6. $Sm(TFSI)_3$ in H_2O as a function of concentration. The blue solid line is the initial ~4.5 mM $Sm(TFSI)_3$ sample, the red dashed line is ~3.0 mM $Sm(TFSI)_3$, and the green dotted line is ~0.1 mM $Sm(TFSI)_3$.

The bands above 300 nm all decrease with decreasing concentration. A separate figure is included (Figure 3.6) so that the changes in this region with concentration can be more readily observed. A sharp band at 402 nm has been reported as a Sm f-f transition in Sm nitrate complexes, and is consistent with the spectrum observed here.[60] Previous researchers have commented on the complexity of assigning the bands to specific transitions to lanthanide species.[61] As such, while it is indicated from the decreasing absorbance with increasing dilution that the bands from 325 to 500 nm are all related to the $Sm(TFSI)_3$ complex, individual assignments could not be readily identified. The use of molecular orbital theory would allow for a more precise analysis of the UV-Visible spectrum, however this type of analysis was outside of the scope of this research.

3.4 U(TFSI)$_3$ Synthesis

3.4.1 Materials

All reagents used in the synthesis of $U(TFSI)_3$ were reagent grade. Bis(trifluoromethanesulfonyl)amine (HTFSI) was purchased from Sigma Aldrich. The RTIL, $[Me_3N^nBu][TFSI]$, was purchased from Solvionic. All purchased reagents were purged with argon gas prior to use to remove any excess oxygen content. The $UI_3(THF)_4$ complex was obtained from a previous synthesis performed at UNLV.

3.4.2 Synthesis of U(TFSI)₃

All reactions were performed in an argon filled glove box. The $UI_3(THF)_4$ (s) was obtained from a prior synthesis based on a procedure by Avens et. al.[62] The $U(TFSI)_3$ synthetic route was designed and executed according to the scheme provided below:

$$\text{HTFSI} \xrightarrow[\text{THF}]{\text{KH}} \text{KTFSI (s)} + H_2(g)$$
$$UI_3(THF)_4 \xrightarrow[\text{THF}]{3K(TFSI)} U(TFSI)_3 + 3KI\text{ (s)}$$
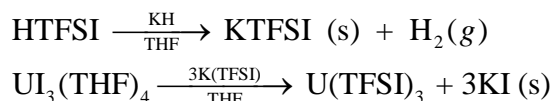
K(TFSI) was synthesized by adding 0.01 g of KH to an air and water free solution of tetrahydrofuran (THF). A 0.07 g sample of HTFSI was added to the solution. The mixture was stirred for three hours to ensure time for reaction completion. The resulting pale yellow solid, K(TFSI), was separated from the THF solution by decanting the excess solution, then allowing the remaining THF to evaporate. The mass of the dried solid product was 55.6 mg (theoretical yield was 61.8 mg, 90% yield). A 0.03 g sample of $UI_3(THF)_4$ (s) was dissolved into an air and water free THF solution and combined with 0.015 g K(TFSI). A slight excess of K(TFSI) was used to ensure reaction completion. The resulting clear pale yellow solution was then stirred for 24 hours. The final solution was orange-red, and contained an off white solid, KI precipitate. The resulting mixture contained the KI solid was then filtered through a cotton filled Pasteur pipette three times to separate KI (s) from the product THF solution containing the $U(TFSI)_3$. The THF was evaporated to leave a solid product $U(TFSI)_3$. The mass was recorded as 66.9 mg, with a 74% yield.

The product is air sensitive. Any attempts at FTIR analysis resulted in inconsistent spectra, as after repeated data collection using the same sample, the bands had visible changes. This was also indicated by the UV spectrum, which was measured first in a sealed sample holder, and again after the cuvette had been opened and a sample used for FTIR analysis. The UV spectra evidenced changes in the band shape and positions after the sample had been exposed to air. Examination by cyclic voltammetry reflects no presence of iodine response in the observed oxidation and reduction processes.

3.4.3 Spectroscopy of U(TFSI)$_3$

The final U(TFSI)$_3$ product in THF solution was compared to the starting material of UI$_3$(THF)$_4$ in the THF solvent as well as iodine in a THF solution (Figure 3.5). Stoppered specialty cuvettes were utilized for the analysis. The samples were prepared and sealed with the stoppers while still in the glove box. Additional precautions were taken to prevent unwanted introduction of air by placing a parafilm over and around the stoppers. The sealed cuvettes were then placed in a secondary, double-sealed container and removed from the argon filled glove box. The samples were immediately analyzed by UV-Vis spectroscopy.
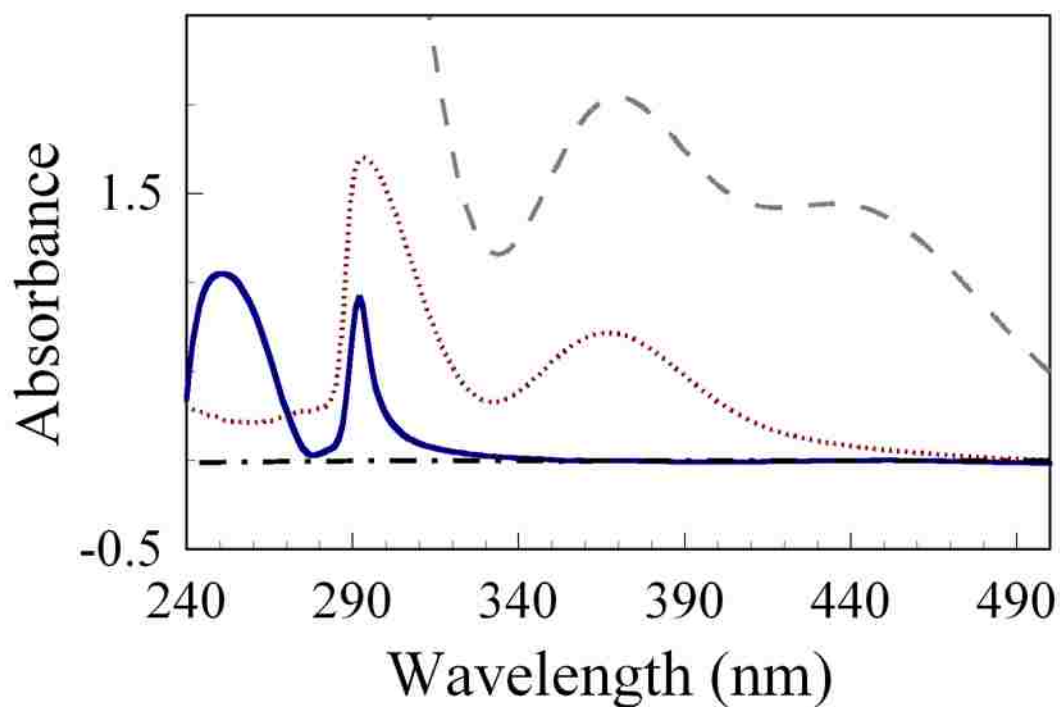
Figure 3.5. UV-Vis spectra of blank reference, (black dotted dashed), 5mM $U(TFSI)_3$ in THF (blue solid), 5mM $UI_3(THF)_4$ in THF (red, dotted), and I_2 in THF (dashed grey).

The U(III) samples were analyzed in the THF solvent against a blank solution containing neat THF solution. The spectrum indicated by the black dotted and dashed line in Figure 3.5 is a blank reference sample containing only the THF solvent. The red dotted line is the spectrum of $UI_3(THF)_4$ and the blue solid line is the spectrum of $U(TFSI)_3$. For comparison, they grey dashed line represents the spectrum of I_2 in THF. The band locations are presented in Table 3.7.

Table 3.7. Comparison of UV-Vis wavelengths of
5mM $U(TFSI)_3$ and 5mM $UI_3(THF)_4$ in RTIL.

Product	Wavelength (nm)		
$U(TFSI)_3$	-	293	251
$UI_3(THF)_4$	368	293	-
I_2	368	-	-

71

Literature on various U(III) complexes is available. [20,63] UV-Vis can be used as a tool to confirm oxidation states by the location of known band positions. However, the "fingerprint region" for identifying a trivalent uranium complexes is above 800 nm.[20] No data was collected in this region. Since the $U(TFSI)_3$ complex was never exposed to air or water, it is assumed that the oxidation state of the uranium complex was unaltered by the synthetic process. Additionally, the observed reduction waves in the electrochemistry of the $U(TFSI)_3$ are consistent with that of the $UI_3(THF)_4$ (See Section 6.3.1). This provides further support that the species remained the 3+ oxidation state.

There is a band centered at 368 nm in the spectrum of the $UI_3(THF)_4$ that is no longer present in the product $U(TFSI)_3$. From reviewing the literature, multiple examples can be found of iodine containing complexes that absorb in this region.[64,65] Additionally, the spectrum of I_2 in THF was obtained for comparison. It can be seen in the figure that there is a band at 368 nm for both the I_2 as well as the $UI_3(THF)_4$ species. The band at 368 nm is not evident in the spectrum of the $U(TFSI)_3$. This is further evidence that the band at 368 nm is present as a result of the iodine in solution. The loss of this band, as assigned to iodine, also indicates that the synthetic reaction to form the product $U(TFSI)_3$ was complete.

The band at 293 nm is visible in both the initial $UI_3(THF)_4$ and the final $U(TFSI)_3$ product spectrums. Both U(III) species were synthesized with THF solution, both complexes could potentially have some THF solvent coordination in the product. As mentioned previously, the final product could also be $U(TFSI)_3(THF)_X$, as opposed to simply $U(TFSI)_3$. A literature search reveals many instances in which THF was used as a synthetic solvent and yielded some degree of coordination in the final product.[66,67] As

such, a band in the UV-Vis band at 293 nm is tentatively assigned to a response related to U-THF complexation.

The spectrum of the final $U(TFSI)_3$ product also has an emergent band at lower wavelengths, with a strong absorbance at 251 nm, indicating the appearance of a new species. This is in the region of the HTFSI band that was observed in the aqueous samarium system, where TFSI reflected an absorption maximum at 268 nm (section 3.3.4). Other spectra taken during this research also include a band in this region when TFSI was in solution. In the discussion of the $Sm(TFSI)_3(H_2O)_3$ complex in Section 3.3.4, the presence of the band at 268 nm was assigned to TFSI. The spectra of UO_2TFSI_2 includes a band in the region of 270 to 290 nm (Section 5.5.1). HTFSI dissolved into the RTIL resulted in a single band, at 270 nm, when analyzed via UV-Vis (Section 5.5.1). Therefore, based on the previously observed spectra of other TFSI complexes analyzed in this research, the emergent band in the $U(TFSI)_3$ product appears to be consistent with the interaction of the uranium with the TFSI in solution.

While the $UI_3(THF)_4$ species contains a metal and an ionic species, this complex has only been reported to contain absorption bands as a result of coordinated bonds.[20] The $UI_3(THF)_4$ is a pentagonal bipyramidal complex where the central uranium atom forms a covalent bond with the 3 iodine species, as well as to the 4 oxygens in the THF rings.[62] As such, in previous literature, it has only been observed to have covalent bonds in the corresponding spectrum.[62]

Further information, such as single crystal structure of the $U(TFSI)_3$ complex would be needed to identify the specific type of bonds that are formed here. Given that there have been cases of the TFSI anion forming both charge transfer complexes as well

as covalent bonds,[47,28,68,69] both could be argued to exist in the $U(TFSI)_3$ species by the UV-Visible spectrum shown here. As such, the band in the $U(TFSI)_3$ spectrum at 251 nm is proposed here to indicate an interaction between the TFSI species and the uranium in solution. However at this time, it cannot be identified as absorbance based on the electronic transitions associated with the ligand interacting weakly with the uranium, or as a covalent or a CT relationship between U-TFSI by this information alone.

One final key point to note is the absence of a series of finger-like bands centered around 430 nm that would be an indication of the formation of an aqueous uranyl complex; and specifically, hydrolysis having occurred in the air sensitive U(III) species.[70] While analyzing the raw data on the UV-Vis instrument, even when zoomed into this region, there were no visible bands. The absence of these peaks is a positive secondary indication that the reaction proceeded without the introduction of water into the system.

Chapter 4: Extraction and Evaluation of Samarium in the RTIL Solvent

4.1 Introduction

One of the most appealing aspects of the RTIL solvent is that it can be multi-functional.   Specifically, it can be used both as an extraction solvent and an electrochemical solvent simultaneously. Following an extraction of samarium from the aqueous phase into the RTIL, it can then be removed from the RTIL by potential-mediated electrodeposition. There is a shortage of studies reflecting the use of the ionic liquid solution for both methods; however the potential uses are immense, especially when applied to the areas of actinide extraction and possible separation schemes.

RTIL solutions have also been examined as solvents for extraction and separation of fission products and actinides.[14,15,16,17,71] Comparisons between the extraction of f-elements using n-dodecane and RTIL systems have been primarily focused on eliminating n-dodecane as the solvent, while maintaining tributylphosphate (TBP) as a complexing agent.[19,72] Previous studies have demonstrated that extraction of f-elements into the RTIL solution in place of n-dodecane is complicated by aqueous anionic species.[72]

For example, the *extraction* of UO_2^{2+} into a RTIL solution using TBP is influenced by the nitrate concentration in the aqueous environment.[72,21]   The neutral $UO_2(TBP)_2(NO_3)_2$ complex is favored as the extracted species, following a linear trend with respect to increasing nitric acid concentration into n-dodecane. In comparison, the

extraction is non-linear with respect to increasing nitric acid concentration when the RTIL, 1-alkyl-3-methylimidazolium/TFSI, was used in the extraction.

The extraction of $UO_2(TBP)^{2+}$ occurs through the exchange of the imidazolium cation in the RTIL at low nitrate concentration, while the neutral complex is favored at high nitrate concentration allowing partitioning without ionic exchange. The extraction of $UO_2(TBP)^{2+}$ was equivalent or enhanced when compared to n-dodecane for increasing HNO_3 concentration when the PF_6^- was used in place of TFSI. The results suggest that the choice of anion may be critical in the solvent extraction of uranium in RTIL when TBP is used, while extraction without TBP may be the key to eliminating the cross-over contamination of RTIL in the aqueous environment.[73]

Lanthanide elements contain electrons in the 4f shell, whereas actinides contain electrons in the 5f shell. The coordination chemistry and solvation behavior of elements containing f-electrons is very different than that of elements containing only p or d electrons.[74] Any examination of electrochemical reduction or extraction processes, such as those presented in this Chapter for samarium will benefit in gaining a better understanding of those properties both in terms of extraction behavior as well as electrochemical behavior.

Currently, to electro-deposit both rare earth metals, such as samarium, as well as actinide elements, molten salt technology is used.[74] As a result of containing f-electrons, both actinides and lanthanides are extremely electropositive and they typically require rather large reduction potentials[74] which cannot be accessed aqueous solution without competing solvent reactions. However, sufficiently negative potentials for electrodeposition can be reached in a RTIL solution.[74] Samarium can also be used to

make comparisons to americium and curium, as all three elements are preferentially found in the trivalent oxidation state.[74]

This chapter will focus on the extraction of samarium into the RTIL, [Me$_3$N^{n}Bu][TFSI], from Sm(TFSI)$_3$(H$_2$O)$_3$ dissolved into aqueous solution. As outlined above, samarium was selected because of interest in rare earth recovery. It was also utilized because electrodeposition of the metal species would be a useful tool for comparison to the electro negativity that is often also required for deposition for actinide species. Electrochemical comparisons can be made between the samarium and actinide species regarding the oxidation and reduction reactions that occur in the RTIL with respect to f-electrons. The work presented in this Chapter was initiated with an extraction from the samarium species in aqueous solution to the RTIL. By examining the extraction conditions, it was found that the extraction efficiency was dependant on the pH of the aqueous phase. At an aqueous pH of 9.0, 100% extraction efficiency was observed. In addition to achieving an efficient extraction of the samarium into the RTIL, the mechanism of the extraction was also examined. Following introduction of the samarium into the RTIL solvent, electrochemical analysis of the oxidative and reductive processes are evaluated, and finally electrodeposition of Sm metal from the RTIL solution at a glassy carbon working electrode is demonstrated.

4.2 Methods

4.2.1 Reagents

The synthesis of the $Sm(TFSI)_3(H_2O)_3$ solid was described in Section 3.1. SmI_2 and $SmCl_3$ solids were obtained from Sigma Aldrich and used as received andstored in a desiccator after opening. The RTIL solvent, $[Me_3N^nBu][TFSI]$, was purchased from Solvionic (France). Nitric acid solutions were prepared with reagent grade acid (ACS reagent grade, Merck KGaA, Germany) and de-ionized (DI) water (18 MΩ, Millipore, USA). ColorpHast pH test strips were used for all pH analysis, and were purchased from VWR.

4.2.2 Extraction Experimental Design

All aqueous solutions were prepared such that they initially contained 0.15 M samarium. To verify the initial concentration, a sample aliquot of 100 μL was removed and added to 10 mL of 2% HNO_3 in a 15 mL centrifuge tube and the pH recorded as pH 2.5 ± 0.3. Next, 10 mL of this initial samarium solution was added to a pre-weighed 50 mL beaker and the mass recorded. An equal volume 10 mL of RTIL was added to the beaker. The new mass and pH were recorded.

A time zero sample aliquot of 100 μL was removed from the aqueous layer and added to 10 mL of 2 % nitric acid for Sm analysis by ICP-MS (For ICP-MS parameters, see Section 2.4). The subsequent measurements were each taken by removing a 100 μL aliquot from the aqueous layer after 1, 5, and 7 hours of the phases being placed into contact with each other. The times and masses were recorded at each sampling to

minimize the experimental error. In addition, to maintain constant volume, 100 μL of the RTIL phase was removed each time a sample was taken from the aqueous phase. The experiment was repeated in triplicate.

4.3 Discussion

4.3.1 Extraction into the RTIL solvent

There has been an increasing interest in the use of RTILs as the solvent in extraction; however the vast majority of recent reports also add either a diluent or extractant to the RTIL solvent to increase the extraction efficiency.[75,76,77,78] Previous studies have reported that no reaction occurred for Sr^{2+}, without the addition of a crown ether extractant to the RTIL. The study also noted that increasing the acid concentration decreased the extraction efficiency.[75] Other studies reported on the effects of the aqueous layer pH on the effectiveness of the extraction of several divalent species. In these experiments, no crown ether was added. In many cases, by approximately pH 6, 100% extraction efficiency was observed.[77] Others also observed results that pointed to tailoring extraction effectiveness when having multiple species in solution by exploiting observed pH dependency on extraction efficiency.[1]

When the extraction was initiated in the experiments performed in this Chapter with no additional diluent or added acid, only 9 % of the samarium was extracted into the RTIL Previous researchers conducted a detailed study on the effects of the pH of the aqueous layer on the extraction efficiency of several RTIL solvents. They conducted analysis using [bmim][PF6], [hmim][PF6], [omim][pf6], nitrobenzene, chloroform, and

toluene. In each experiment, 1 mL of RTIL was placed in contact with 5 mL of aqueous solution. The aqueous phase total volume included a 10^{-2} mol/L buffer and 10^{-5} to 10^{-4} mol/L of M^{2+} (M=Mn, Co, Ni, Cu, Zn, Cd, or Pb) species. It was observed that the highest system efficiency was reeached between pH 5-7.[77]

This comparison was utilized on the basis of examining extractions of a metal species into an RTIL system with no added extracting agent. Since these metals are in the 2+ oxidation state, and the research performed in this dissertation focused on the 3+ oxidation state, there would be expected changes in the strength of the resulting extracted metal complex based on the different oxidation state of the metals.[79] However, the comparison was still useful for examining the process of a metal extracted into a RTIL.

An excerpt of the findings for one of the RTILs examined are summarized in Table 4.1, below.

Table 4.1. Comparison of RTIL Extraction Results for Mn^{2+} extracted into [bmim][PF$_6$] [77]

RTIL	Metal Species	~Aqueous pH	~Extraction Efficiency
[bmim][PF$_6$]	Mn^{2+}	4	0
[bmim][PF$_6$]	Mn^{2+}	4.7	5
[bmim][PF$_6$]	Mn^{2+}	5	20
[bmim][PF$_6$]	Mn^{2+}	5.3	50
[bmim][PF$_6$]	Mn^{2+}	5.7	75
[bmim][PF$_6$]	Mn^{2+}	6	99

Upon further investigation of the conditions of the experiments performed for this Chapter, the pH of the aqueous layer was determined to be 2.5 $\pm$ 0.3 which would coordinate with a region of low extraction efficiency in studies discussed above.[77]

Following this observation, repeated extractions were performed by adding NaOH to decrease the acidity of the aqueous phase. Sodium hydroxide was selected for this procedure, as it was not expected to alter the conditions of the species in the RTIL phase because it was not expected to cross over into the RTIL solution. The two phases were kept at a constant equal volume, such that $V_o/V_{aq} = 1$. The Extraction efficiency (E%), which also represents the percent of samarium extracted into the RTIL, was then calculated as follows[80]:

$$E\% = \frac{D}{D + \dfrac{V_o}{V_{aq}}} \times 100\%$$

$$D = \frac{[Sm]_o}{[Sm]_{aq}}$$

Equation 4.1

Where: E% = Percent Efficiency for the extraction
D = Distribution coefficient
V_o = Volume of the organic phase
V_{aq} = Volume of the aqueous phase
$[Sm]_o$ = Samarium concentration, organic phase
$[Sm]_{aq}$ = Samarium concentration, aqueous phase

Extraction efficiency was utilized instead of the distribution coefficient, D, so that a comparison of the work done in this Chapter could be made against published work from literature reviewed.

With increasing pH of the aqueous phase, improved extraction efficiency was obtained (Figure 4.1). At pH 9 ± 0.3, 95 % extraction efficiency occurred within 1 hour, and 100 % extraction efficiency was observed within 5 hours of the phases being placed in contact with each other.

There have been examples of acidifying the aqueous phase to increase concentration crossover to the organic RTIL phase. In fact, all references reviewed indicated that low aqueous pH decreased the extraction efficiency. At pH values of 0, typically, no extraction occurred.[75,76,77] Additionally, the initial aqueous pH of the samarium extraction was 2.5. Under this condition, only 7% of the samarium was extracted into the RTIL. Lowering the aqueous pH levels was not considered a viable method for increasing extraction based on previous results.

An alternative route to increase extraction efficiency may have been to acidify the RTIL phase by adding an organic acid. The theory is that if the RTIL's acidity was lower than that of the aqueous phase's acidity, the samarium in solution may have extracted based on preference towards the more acidic solution. However, this experiment was not performed in this dissertation.
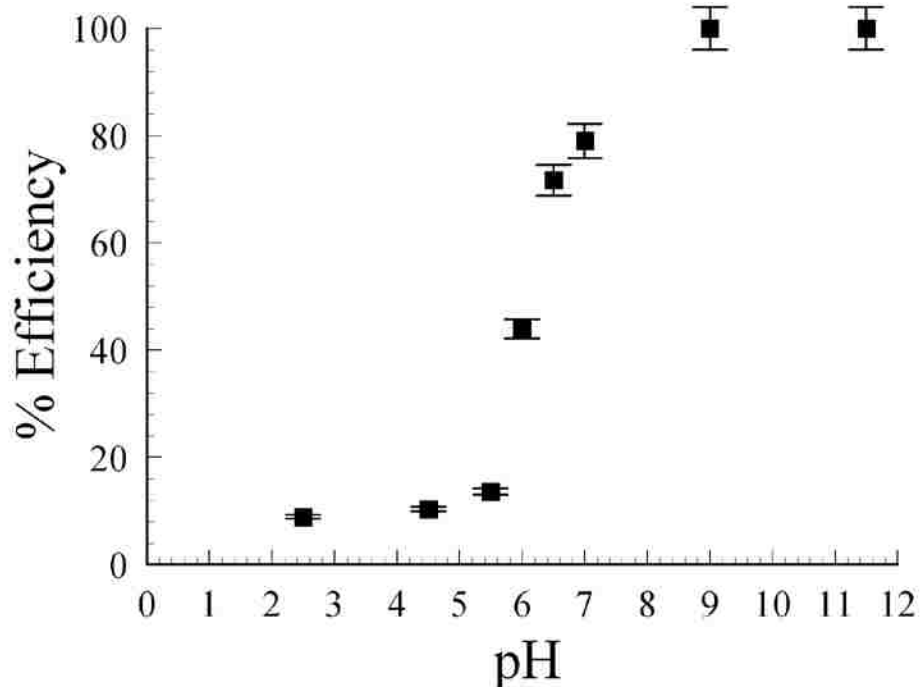
Figure 4.1. Efficiency of samarium extracted into the RTIL as a function of pH.

Clearly, the effects of the aqueous layer pH cannot be ignored when considering the extraction potential of the RTIL solvent. The pKa of the HTFSI super acid has been reported to be -14 to -16.[81] Strong acids, by definition, are almost completely dissociated in aqueous solution.[48] Thus, the initial aqueous conditions indicate that any HTFSI in solution would likely be dissociated. This may also carry through to the Sm-TFSI complex. However, with the increasing aqueous pH, the TFSI in solution may re-associate. One possible mechanism for the extraction may be that the Sm-TFSI complex dissociates initially in aqueous solution, and as the pH is increased, the species re-associates and crosses over into the RTIL.

In all extractions, the acidity of the RTIL was also measured using pH indicator strips, and it was consistently found to be pH 5.5. At the time of this experiment, there were no references for measuring the acidity of the RTIL. As such, this technique of verifying the proton salvation conditions of the RTIL has not been previously documented. Litmus paper was selected because the color change is the result of a chemical reaction associated with species within the paper. These reactions are indicative of acid or base content which is relevant to the measurement of the acidity of the RTIL. With the caveat that there may be additional error associated with this method of measuring the RTIL's acidity, these results indicate that even as the extraction progresses, the RTIL's acidity remains constant. In addition, this demonstrates that adding sodium hydroxide to the aqueous layer has no observable affect on the acidity of the RTIL phase. Additional extraction experiments were performed to determine the primary driving force for the extraction mechanism. Specifically the research was

designed to find if the aqueous pH, oxidation state, or speciation play an important role in the extraction efficiency. Several species were evaluated at their initial pH of 2.5 in water, and at an aqueous pH of 6.5. This process was repeated for $Sm(TFSI)_3$, $SmCl_3$, and SmI_2. The data shows that at pH 6.5, the extraction efficiency of samarium into the RTIL beginning with $Sm(TFSI)_3$ in water was highest at 72%. Similarly, starting with $SmCl_3$ in water yielded 48% efficiency, and SmI_2 was 43% efficient. These results are also presented in Table 4.2.

Table 4.2. Comparison of extraction results for $SmCl_3$, SmI_2, and $Sm(TFSI)_3$ into the RTIL.

Initial Species	Initial Solid Species Oxidation State	Extraction pH	% E
$SmCl_3$	3	6.5	48 ± 2.4
SmI_2	2	6.5	43 ± 2.1
$Sm(TFSI)_3$	3	6.5	72 ± 3.7

While SmI_2 is expected to oxidize in water, the analysis was still performed. Additionally, the UV-Vis spectrum was collected of the extracted species in RTIL from the SmI_2 system. The resulting spectrum yielded a markedly different band structure than that of the $SmCl_3$ or $Sm(TFSI)_3$, thus indicating that there were observable differences between the two systems. These results will be discussed further in Section 4.3.2.

Given that $Sm(TFSI)_3$ and $SmCl_3$ are initially in the +3 oxidation state, and the final pH was 6.5 for both extractions, the only difference between the two complexes is the TFSI and the chlorine ligand. In this comparison, the extraction was nearly 25% more efficient for $Sm(TFSI)_3$ when compared to $SmCl_3$. When comparing the extraction of $SmCl_3$ with SmI_2 the results were similar with $SmCl_3$ extracted at

slightly higher efficiency. However, when the error is factored in, the extraction efficiencies of the $SmCl_3$ and the SmI_2 are effectively equivalent. When considering the initial SmI_2 complex in solution, any Sm(II) that oxidizes to Sm(III) could potentially form a SmI_3 complex upon any re-complexation. However, there would be insufficient iodine to allow for all of the samarium in solution to form this complex, leaving some samarium as ionic Sm(III) or Sm(II) in solution. Additionally, addition of NaOH to the aqueous layer could allow for the formation of $Sm(OH)_3$ as follows:

$$SmCl_3 \text{ (aq)} + 3NaOH \text{ (aq)} \rightarrow Sm(OH)_3 \text{ (s)} + 3NaCl$$
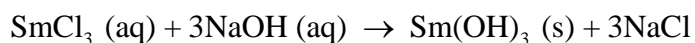
If any solid $Sm(OH)_3$ formed before the extraction was completed, this would have also resulted in a lower total extraction efficiency, as less samarium would be available in solution to cross over into the RTIL phase.

The findings presented in Table 4.2 indicate that the extraction of samarium into the RTIL from $Sm(TFSI)_3$ in water is more favorable than either $SmCl_3$ or SmI_2 from aqueous solutions at the same pH. In this case, having a shared counter-ion on the samarium complex and the RTIL used for the extraction resulted in the most favorable extraction among the conditions analyzed. Or, as mentioned above, the sodium hydroxide addition may have removed some of the samarium from solution by formation of the solid $Sm(OH)_3$ species, thus limiting the extraction potential of the $SmCl_3$ system. Additional extraction studies of Sm in other RTIL solutions with common anions between the complexes and the ionic liquid would be useful in assessing the role of the anion in extraction processes, but it was outside the scope of the dissertation.

Returning to the literature reviewed, an analysis was completed by previous researchers comparing the results of extractions from an aqueous solution 10% acetonitrile and 90% water (v/v%) into pristine RTIL of Cu^{2+} and CuL_2 at multiple acid concentrations, where $L=PF_6$. The RTIL used also contained the PF_6 anion, $[C_4mim][PF_6]$ The concentration of Cu^{2+} was measured using Atomic absorption spectroscopy. It was found that the extraction efficiency of uncharged Cu^{2+} was zero at all pH values analyzed, however uncharged CuL_2 was observed in successful extractions. The results reflected that extraction of only the ionic species was less successful than extractions of species beginning with a metal-ligand.[1]

In the results presented from the work in this Chapter, extraction of samarium beginning with the $Sm(TFSI)_3$ complex was more efficient than beginning with the $SmCl_3$ or SmI_2 species. When comparing the findings of the literature that was discussed in the previous paragraph[1] with the results observed in this Dissertation, all data collected from the experiments performed in this Chapter indicate that a highly efficient extraction depends on the initial ligand to which the extracted samarium was complexed with. In the results presented here, extraction of samarium beginning with the $Sm(TFSI)_3$ complex was more efficient than beginning with the $SmCl_3$ or SmI_2 species. Based on the information available, both from the presented literature reviews and experiment, it appears that the shared ligand between the extracted species and the RTIL increases the efficiency of the extraction markedly. These results, as presented here, are likely either do to the affects of extracting the Sm-TFSI into a RTIL solution containing the TFSI anion or due to an undesired formation of samarium precipitate in aqueous solution with the increasing addition of NaOH.

4.3.2 Spectroscopy

UV-Visible spectra were taken of the $Sm(TFSI)_3$ in both aqueous and RTIL solvent (Figure 4.2). In these experiments, a double beam was used, where the solvent spectrum was ratioed against the sample spectrum (see Section 2.1.1). Specifically, the $[Me_3N^nBu][TFSI]$ solvent was used as a blank for the $Sm(TFSI)_3$ sample in RTIL solvent; and water was used as a blank for the $Sm(TFSI)_3$ sample in aqueous solution. The speciation details of the band structure in the aqueous system were discussed in Section 3.3.4, in Figures 3.5 and 3.6. The discussion here will focus on the differences between the two solvents in terms of observed band structure.
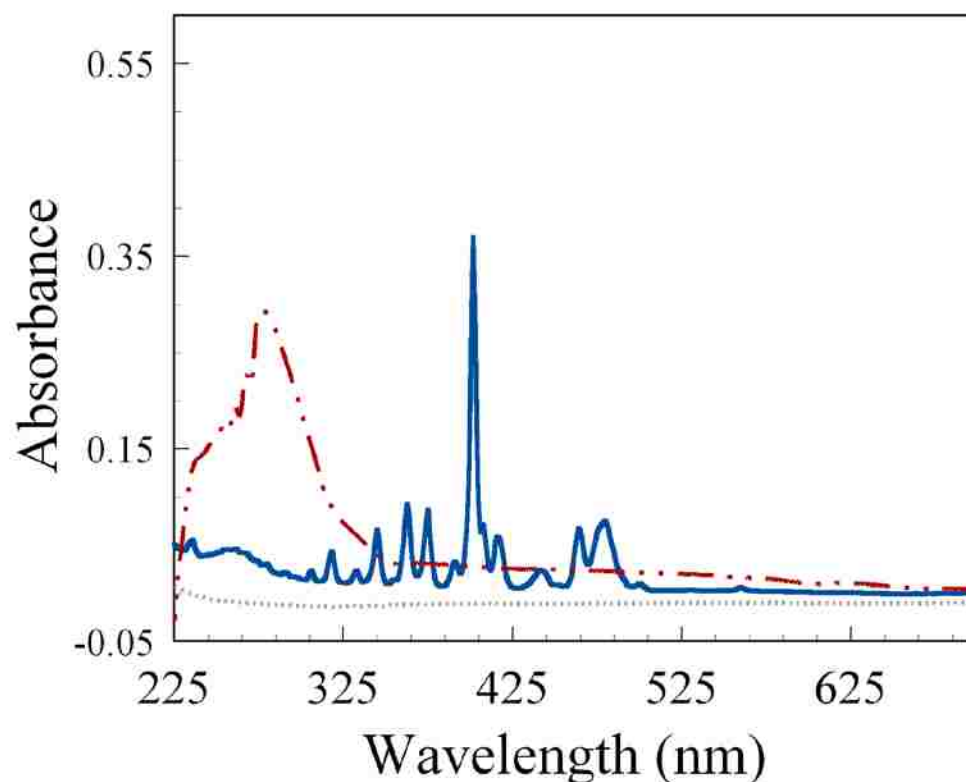
Figure 4.2. UV-Visible spectra of 0.03 M $Sm(TFSI)_3$ in RTIL (red, dotted dashed) and 4.5 mM $Sm(TFSI)_3$ in H_2O (blue, line), and the RTIL blank (grey, dotted). Concentrations are prior to dilution of the aqueous samarium solution from 0.28 M.

There is a clear change in the spectrum of the extracted samarium in the RTIL solvent when compared to the spectrum of the $Sm(TFSI)_3$ in water. As mentioned above, in Section 3.3.4, the samarium UV-Vis spectroscopy was discussed at length. In that Section, the sharp band observed in this work at 402 nm was referenced to literature reviewed in which it was reported as a Sm f-f transition in Sm nitrate complexes.[60] Additionally, HTFSI was dissolved into water and observed at 264 nm. Based on experimental indications from the work performed in this Dissertation and behavior from the referenced literature, band at 264 nm was assigned to TFSI anion that has *dissociated* from the samarium complex and then subsequently formed the HTFSI complex.[58,59] In the aqueous system, there are a number of intense absorbance bands representing f-f transitions in the region from around 310 to 500 nm. Conversely, in the RTIL solvent, the fine spectral bands have been lost in place of a notable increase over the RTIL blank baseline when observing the minimum absorbance over the region starting from around 750 and extending down to 320 nm. Also in the RTIL there is an intense asymmetric band at about 270 nm, at the end of which are a series of maxima on the shoulder. This experiment was repeated 3 times.

Changes in the extracted species spectrum have been noted in examples from the literature as well.[1] Previous researchers recorded the UV-Vis spectrum of dithizone in the aqueous phase, as well as dithizone extracted into an RTIL. In the aqueous solution, there were two bands observed, one at ~440 nm, and the other at ~620 nm. However, when the spectrum was observed in the RTIL, only one broad band was found, at ~480 nm, along with an increase in the remaining spectrum where the resulting minimum absorbance never drops below ~0.15. In their case, the researched presented that the

proton of the dithizone was extracted partially solvated into the ionic liquid.[1] Further studies would need to be conducted to fully understand the reasons for the changes in the spectrum of the extracted species from that of the aqueous species.

In Section 3.3.4 the band at 268 nm for water spiked with HTFSI was discussed (Figure 3.5). As mentioned above, this experiment was performed to verify that HTFSI does have an absorbance band in this region. The results indicated that TFSI had dissociated from the samarium complex and re-associated with the water in the aqueous solution to form HTFSI.[58,59] This analysis methodology was repeated by spiking RTIL with excess HTFSI, and the emergent band remained at 268 nm. Based on the detailed discussion in Section 3.3.4 that was summarized above, the band observed in the $Sm(TFSI)_3$ in RTIL spectrum at 270 nm is then attributed to an interaction involving the HTFSI species in solution.[58,59]   These results suggest that the solvent the complex is measured in directly affects the bands seen in the spectrum.

The lack of fine structure observed in the extracted samarium in the RTIL is not isolated to this single instance. In all RTIL spectra observed in this dissertation, only two or three very broad bands were identified. Upon examining the literature with commonly found RTIL solvents, a pattern of broad spectra appeared.[82,83,84,85,86]

In the literature reviewed, $EuCl_3$ solutions in [Bu-mim][TFSI] showed similar absorbance at 320 nm.[87] In other examples, there was a broad band observed in the absorption spectrum at 280 nm in a dichloromethane solution containining tetrabutlyl ammoniu chloride and Eu.[83] Still other researchers observed two broad bands, one at 375 nm, and one at 490 nm when examining the UV-Vis absorption spectra of $PdCl_2$ in [tetraalkyl phosphonium][TFSI]. In this case, the observed bands were assigned to d^5

electron transitions as well as ligand-metal charge transfer interactions.[85]   Yet another

example using the spectrum of [1-FcPyl$^+$][TFSI]$^-$ in dichloromethane reflected three

broad bands; one at ~395 nm, one at ~500 nm, and one at ~975 nm.[86]   The sheer volume

of instances where the broad bands are demonstrated is an indication this type of broad

spectra is not atypical when examining an RTIL. Further studies beyond the scope of this

work would be required to have a full understanding and confirmation of this

observation.

UV-Visible spectroscopy was also utilized to ensure that the extracted species

with NaOH addition to alter the aqueous pH to 6.5 was unchanged from the extracted

species with no added base, where the aqueous solution was left at it's initial pH of 2.5

(Figure 4.3).
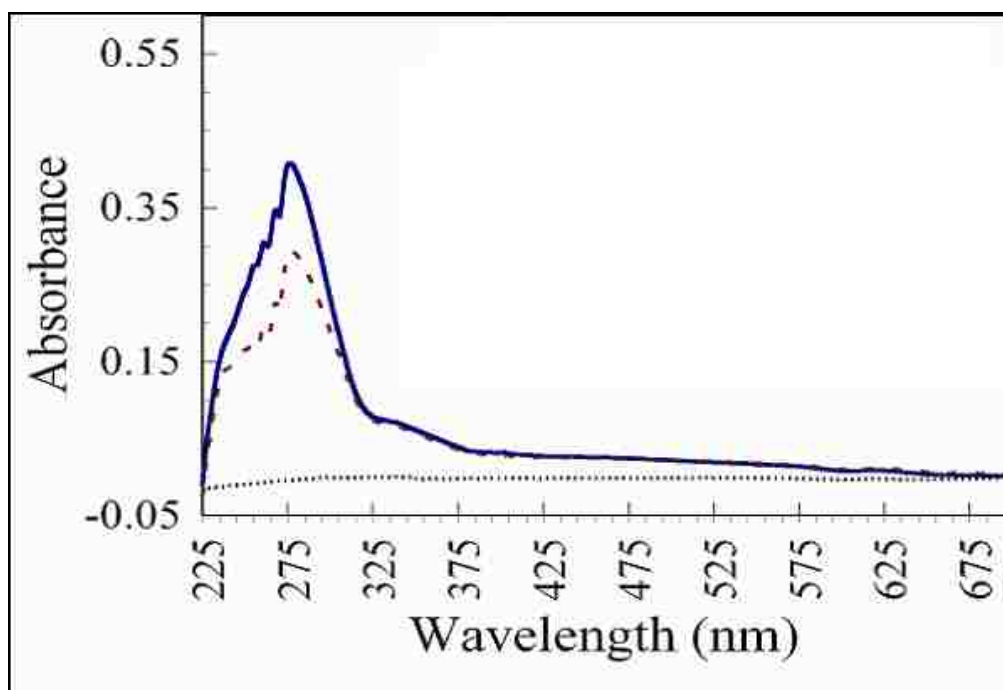
Figure 4.3. UV-Visible spectra of 0.025 M samarium extracted into the RTIL from a pH
2.5 aqueous solution (red, dashed, bottom), and 0.030 M samarium with NaOH added to
the aqueous layer to a final pH of 6.5 (blue, solid, top), and RTIL baseline (black, dotted)
Samples were collected after 0.5 hours of phase contact. The inset is provided to zoom
into the region of 225 to 325 nm.

The samarium sample was added directly to water, and mixed. The resulting aqueous samarium solution was then evenly divided and used for the two separate experiments. This experiment was designed to qualitatively analyze if there was any change in speciation between the two systems. The samples that were used were obtained after 0.5 hours of extraction progress. This was an additional extraction that was performed separately from the previously outlined experiments for the purpose of evaluating the UV-Vis spectra. It was performed separately so as to not interfere with the overall solution volume or ratio of the liquid phases. Other than the maximum intensity, all bands are in the same positions with no observable shifting. Based on the results depicted in the spectra, it can be observed that addition of NaOH to the aqueous solvent does not appear to affect the species that is extracted into the RTIL.

Finally, the UV-Vis spectrum of samarium extracted into the RTIL from SmI_2 in water was observed. This experiment was performed to determine if there was an notable difference in the band structure of the extractions beginning with SmI_2 compared to starting with $Sm(TFSI)_3$ or $SmCl_3$.
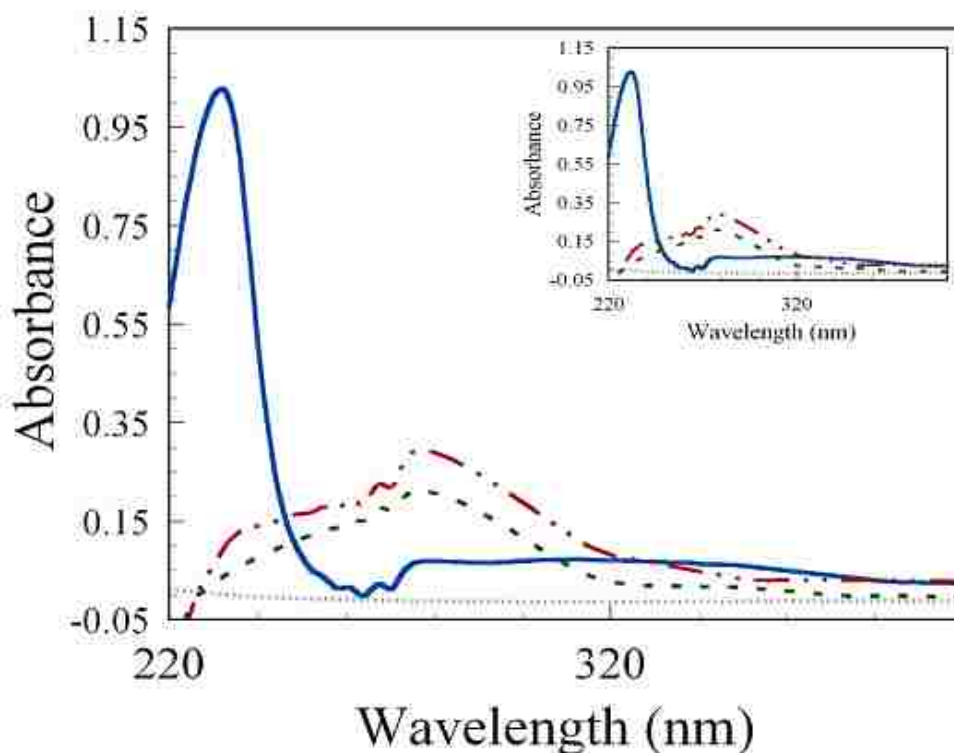
Figure 4.4. Samarium extracted into a RTIL solution from SmI_2 in water (blue line. 0.025 M Samarium extracted into RTIL from $Sm(TFSI)_3$ in water (red, dotted dashed line) 0.02 M Samarium extracted from $SmCl_3$ in water (green, dashed). Baseline (dotted grey line).

In Figure 4.4, it can be seen from the UV-Vis spectrum of the samarium extracted into the RTIL that there is a notable change in the observed bands when beginning with SmI_2 in aqueous solution when compared with the samarium extracted from $Sm(TFSI)_3$ or $SmCl_3$. The resulting spectrum of the samarium in RTIL when initially beginning with $SmCl_3$ in water is remarkably similar to the spectrum that results from beginning with $Sm(TFSI)_3$. However, on close observation there are two shoulders appearing on the $Sm(TFSI)_3$ extraction spectrum that are not present on the $SmCl_3$ spectrum; one at 238 and the other at 335 nm.

The only change in these systems is that of TFSI; therefore the additional bands could be as a result of either free or complexed TFSI being introduced into the RTIL solution. As discussed above, adding HTFSI acid to pristine RTIL solution resulted in a band at 268 nm. Spiking the final samarium extraction solution with HTFSI may have provided additional insight into these additional bands; however this experiment was not completed in this research. The spectrum of the extraction from SmI_2 is completely different than that of the other two, with an intense band at 210 nm. The results are clear in that the extractions starting with each species did indeed affect the species observed in the RTIL.

The variations in the species introduced into the aqueous phase are likely the cause of these noted differences in the observed band structure. As discussed previously, the Sm-TFSI shared anion complex may be extracted as the complexed species, whereas the $SmCl_3$ and SmI_2 initial species may be extracted as ionic samarium. Additionally, there is the possibility of formation of $Sm(OH)_3$ precipitation interfering with this extraction in the latter extractions. A detailed modeling study and experiment designed to gain a deeper understanding the nature of the extraction would aid in gaining more information into the mechanism, but this was not performed in this dissertation.

4.3.3 Electrochemistry

In order to obtain an understanding of the potential mediated oxidation and reduction processes, the RTIL solvent containing the extracted $Sm(TFSI)_3$ complex was evaluated using cyclic voltammetry (CV). A quartz crystal microbalance (QCM) was utilized to obtain an understanding of the processes involved in the deposition of Sm onto

93

the electrode surface.   Finally the potential driven electro-deposition of Sm was performed at a constant -1.8 V versus NHE at glassy carbon electrodes to achieve a samarium metal deposit on the surface of the electrode.

Figure 4.5 is a representative CV with the corresponding QCM response of the samarium extracted from aqueous $Sm(TFSI)_3(H_2O)_3$ into the $[Me_3N^nBu][TFSI]$ solution. The solid lines, blue, red, and green, are the   voltammograms obtained from analyzing the samarium in the RTIL solution at the end of the 1st cycle, the 20th cycle, and the 50th cycle, respectively. The potential was varied beginning under reducing conditions to 1.5 V versus NHE and cycled to + 2.1 V versus NHE using a quartz crystal microbalance (QCM). The resulting current and frequency was measured as the potential was varied. The dashed black line is the background response of the RTIL alone. These elements are also labeled within the figure. There are three reduction waves that can be observed in the 50th cycle in Figure 4.4; one at 1.2, one at 0.4 V and the other at -0.3 V versus NHE. In addition, there are four oxidation waves that can be seen in the 50th cycle at 1.5, 1.2, 0.4, and -0.2, V versus NHE. These results are presented in Table 4.3.

Table 4.3. $Sm(TFSI)_3$ in RTIL oxidation and reduction
process peak maxima potentials.

Band #	Reduction (V)	Oxidation (V)
1	1.2	1.5
2	0.4	1.2
3	-0.3	0.4
4		-0.2

By evaluating the changes in frequency as the potential is varied, an understanding of the resulting bands at each reduction and oxidation step can be gained.

As mass is deposited onto the electrode, the corresponding response from the quartz crystal will shift to lower frequencies.[88]   Thus the mass of material deposited is proportional to the frequency observed. In the case of the reduction of samarium onto the electrode surface, the results must be closely examined.
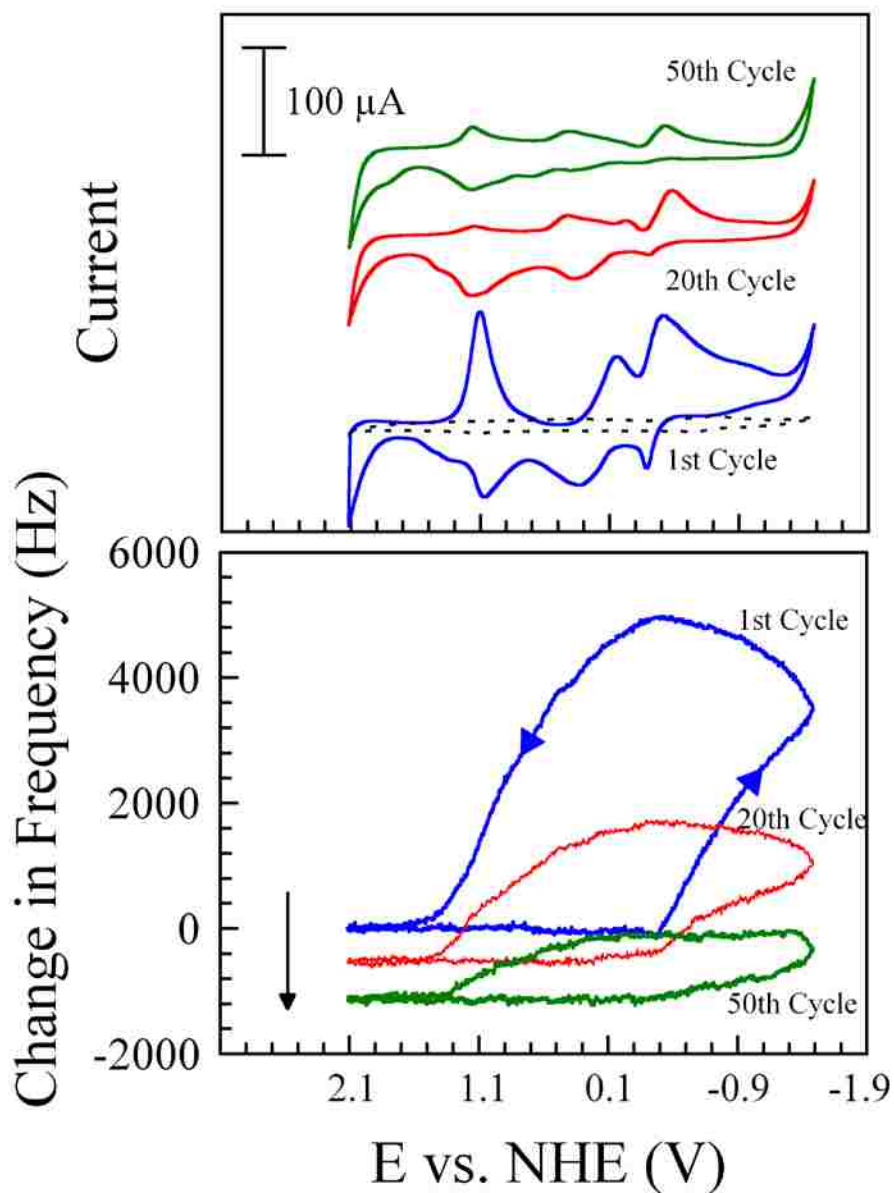
Figure 4.5. Cyclic voltammogram and corresponding QCM measurements taken at 100 mV/s of [Me$_3$N^{n}Bu][TFSI] alone (dashed line), and Sm(TFSI)$_3$(H$_2$O)$_3$ in [Me$_3$N^{n}Bu][TFSI] (solid lines, blue=1st cycle, red=20th cycle, and green=50th cycle).

In Figure 4.5, the first CV cycle (blue, labeled) is shown in the top section, and the corresponding QCM measurement is reflected (blue, labeled) in the bottom section. The arrows indicate the direction of the CV scan as they relate to the changes in observed frequency. The frequency increased as the potential was cycled to negative, reducing potentials; and subsequently decreased as the current was cycled towards positive potentials. This is not a typical response for the case when electrodeposition is occurring, as a decrease in frequency as the potential is made more negative would be expected.

One possible explanation for the unexpected increasing current response under reducing conditions is viscoelasticity. When a material has viscoelastic properties, it behaves as both viscous and elastic materials would respond.[88] It has been reported in the literature that an increase in the frequency was observed from the QCM as the deposition of aluminum occurred at the electrode surface from an RTIL solution. This result was attributed to a viscosity decrease as a result of anion decomposition.[88] To examine if this was the case in this research, a background scan of the RTIL was obtained (Figure 4.6). If the anion was decomposing and dramatically affecting the viscoelasticity of the system, then the background should reflect this by an increase in frequency. This was not observed, as when reviewing Figure 4.6 (green, labeled) the CV response is shown with the QCM response below it.
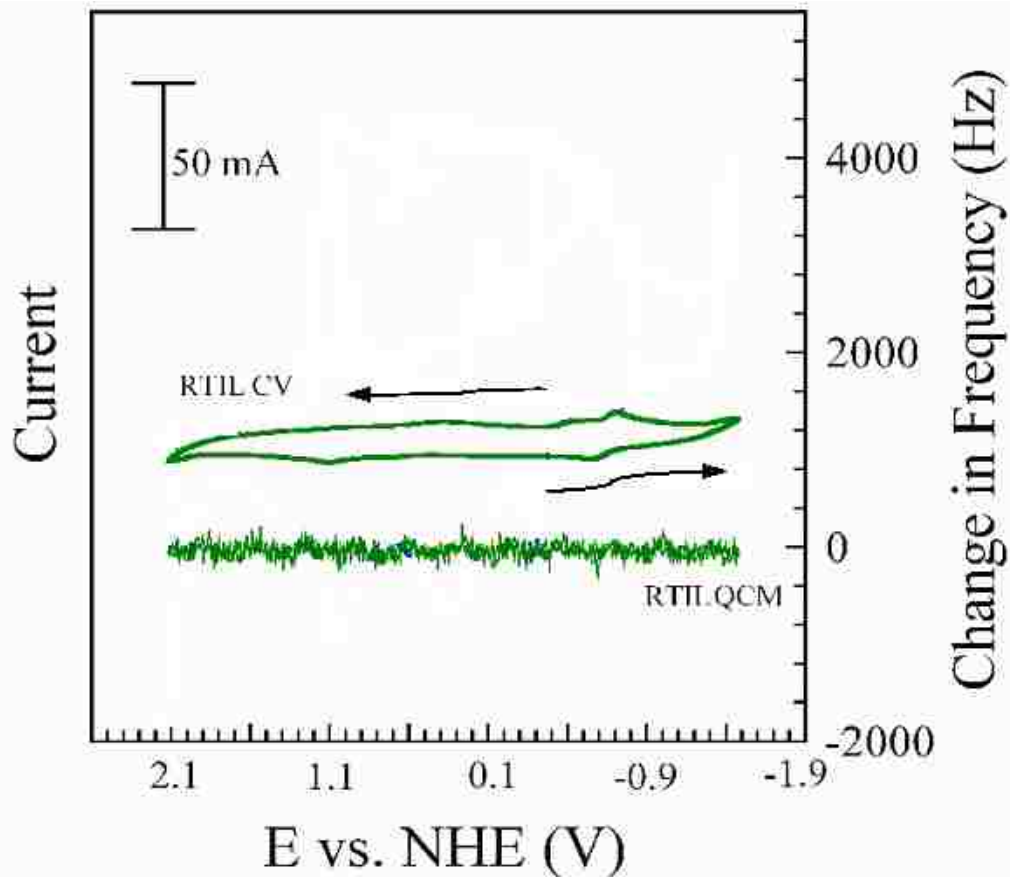
Figure 4.6. QCM and corresponding CV for the RTIL background (labeled). The arrows indicate the direction of the potential.

It can be seen in Figure 4.6 that the QCM background had a consistent current of zero with respect to frequency as the CV was obtained. As a result of this finding, it is considered unlikely that the increase in current under reducing conditions is caused entirely by viscoelasticity. However, it should be noted that it is also possible that there is some combination of RTIL degradation mixed with the TFSI ligand displacement from samarium that causes a slight change in the viscosity near the electrode surface as the ligand desorbs.

The mechanism for samarium deposition can then be inferred from these findings. The frequency begins to increase under reducing conditions at -0.1 V versus NHE. An increase in frequency reflects that there is less mass on the surface of the electrode. As the cycle reverses towards more positive potentials (from -1.5 V to -0.1 V), the frequency initially continues to increase. At -0.1 V under continued oxidizing conditions, the frequency begins to decrease. A decrease in frequency is associated with increasing mass on the surface of the electrode. An overall decrease in frequency from cycle 1 (Figure 4.4 (blue, top)) to cycle 50 (Figure 4.5 (green, bottom)) was observed.

A stepwise deposit, in which the initial deposit contains a Sm-TFSI complex, is indicated from these results. A samarium-TFSI complex has a greater mass than samarium alone. The displacement of the TFSI anion from the electrode surface under further reducing conditions would account for the increase in mass as the potential is decreased. The frequency then decreases during each cycle as the mass on the electrode surface increases when the free TFSI$^-$ in solution re-complexes to the samarium. The QCM results also indicate that with the completion of each full cycle, the total mass on the electrode surface has increased. As the number of cycles increases, more Sm(0) is left on the face of the electrode.

The Sauerbrey equation can be used to determine the mass of materials that were deposited onto the surface of the electrode:[89]

$$\Delta f = \frac{2 \times f_0^2 \times \Delta m}{A \times \left(\rho_q \mu_q\right)^{1/2}}$$

Equation 4.1

Where:

Δf = measured frequency shift
f_0 = resonant frequency of the fundamental mode of the crystal
Δm = mass change per unit area (g/cm^2)
A = piezo-electrically active area
ρ_q = density of quartz, 2.648 g/cm^3
μ_q = shear modulus of quartz, 2.947×10^{11} g/(cm $\times$ s^2)

The Sauerbrey equation could be solved for the mass of the deposit on the electrode surface, however it must be proven to be valid under the conditions of the system first.[89] Specifically, it has been found if the deposit is not uniform, or if the solution is too viscous, the Sauerbrey equation is not valid.[89-90] In addition, the fact that the resonant frequency of the crystal in air is not the same as the resonant frequency in liquid should be taken into consideration.[90] One way to do this would be to plot the known mass deposited against the frequency change. The mass of the deposits obtained in this Chapter were not measured by another means, so this is not possible.

In summary, it is proposed that samarium initially is deposited still partially complexed to the TFSI ligand, and as the potential is decreased, the TFSI ligand is removed. Scheme 4.1 illustrates this concept. These findings do not dictate that this is the only process occurring at each wave, as it is possible that the Sm(II)/Sm(III) oxidation step is occurring simultaneously with the Sm-TFSI re-formation on the surface of the electrode. The results reflect that the Sm-TFSI species is first electrodeposited together on the electrode, and then the TFSI is removed at more negative potentials.

TFSI   TFSI   + 2(TFSI)$^-$

Sm   2e-   Sm

Au Electrode   Au Electrode
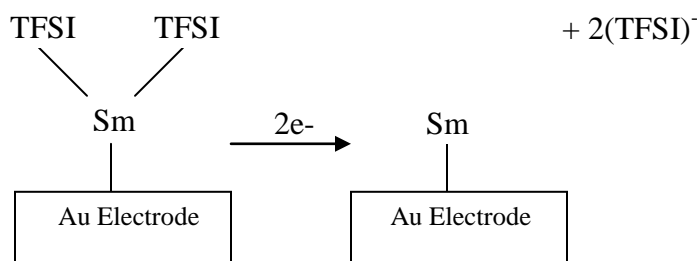
Scheme 4.1. Proposed mechanism for the reduction to Sm(0) at the electrode surface.

Previous reports of reduction to samarium metal in aqueous systems have been found at much more negative potentials, near -2.7 V.[48]   Parrish et al reported electrodeposition at -2.1 V from SmOTf in a RTIL solution, which shares many functional groups with the TFSI anion selected for this work.[91] These findings are of particular interest given the deposition in this system occurred between -0.33 for the Sm-TFSI complex and -1.5 V for Sm(0). This is still thermodynamically more favorable than the deposition from the SmOTf complex. The results suggest that the electrodeposition of samarium from solutions in [Me$_3$N^{n}Bu][TFSI] of extracted Sm(TFSI)$_3$ is more favorable than previous systems reported in the literature. A more thermodynamically favorable deposit may make it possible to obtain larger quantities of material from deposition from the RTIL solution in shorter time scales.[92]

The initial samarium deposition occurs at -0.33 V, and as the potential is swept in the negative direction the TFSI ligands are removed until approximately -1.5 V. At this point all of the TFSI ligands appear to have been removed from the electrode surface. Thus, the instrument was set to maintain a sufficient over-potential to create a driving force to allow for bulk Sm(0) deposition to occur. The deposit was desired to reach a

quantity suitable for further analysis with SEM and EDS. (Section 2.5.1)Thus, a constant

potential of -1.8 V versus NHE was selected, and the current response was measured as a

function of time (Figure 4.7).
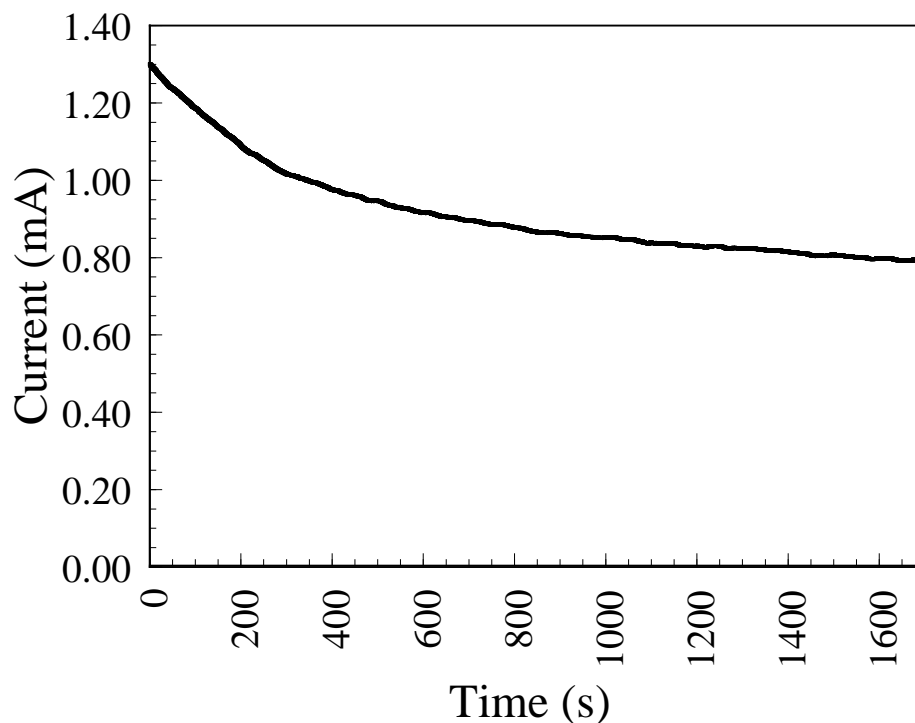
Figure 4.7.   Potential mediated deposition of Sm from a solution of 0.05 M Sm(TFSI)$_3$(H$_2$O)$_3$ in [Me$_3$N^{n}Bu][TFSI].

The current response is directly proportional to the amount of samarium in the

RTIL solvent, so a decrease in the current indicates a decrease in the amount of samarium

in the solution, or conversely, an increase in the amount of Sm deposited at the electrode

surface.[44]   Additionally, a plateau may indicate that the potential is not sufficient for

further depositon.At 1600 s, the rapid change observed in the current response had

slowed, and the electrodeposition process was stopped. The electrode was then removed

from solution, cleaned (see Section 2.4.3), and measured with SEM and EDS to obtain

101

images of the Sm deposit and electrode surface as well as to determine the elemental composition of the deposit.

4.3.4 Analysis of the electrodeposition

Following successful potential mediated electrodeposition of the samarium onto the electrode, it was analyzed via SEM and EDS. In the SEM image shown in Figure 4.8, the deposit of samarium can be seen on a gold sheet electrode. The samarium is in the grey ridges in the center of the image, and the light lines creating a grain look to the electrode surface is the surface of the gold electrode.
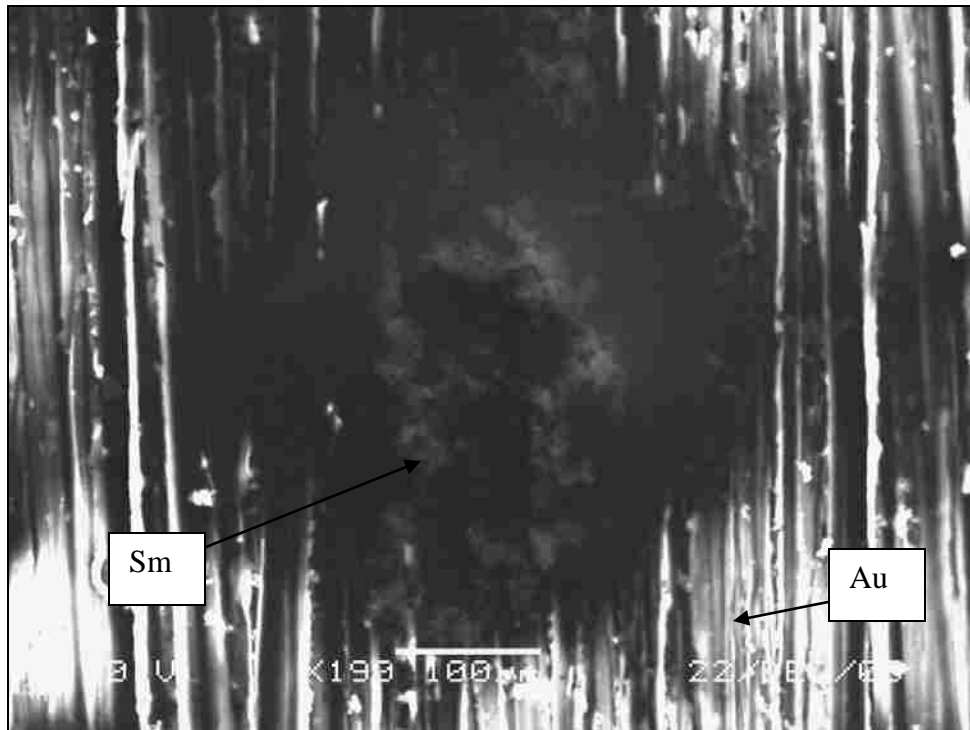
Figure 4.8. SEM image of samarium deposit on the gold electrode.

The EDS analysis presented in Figure 4.9, below, confirmed the elemental composition of the deposit.   In this case, the samarium deposit was not very large, so the gold dominated the count response.
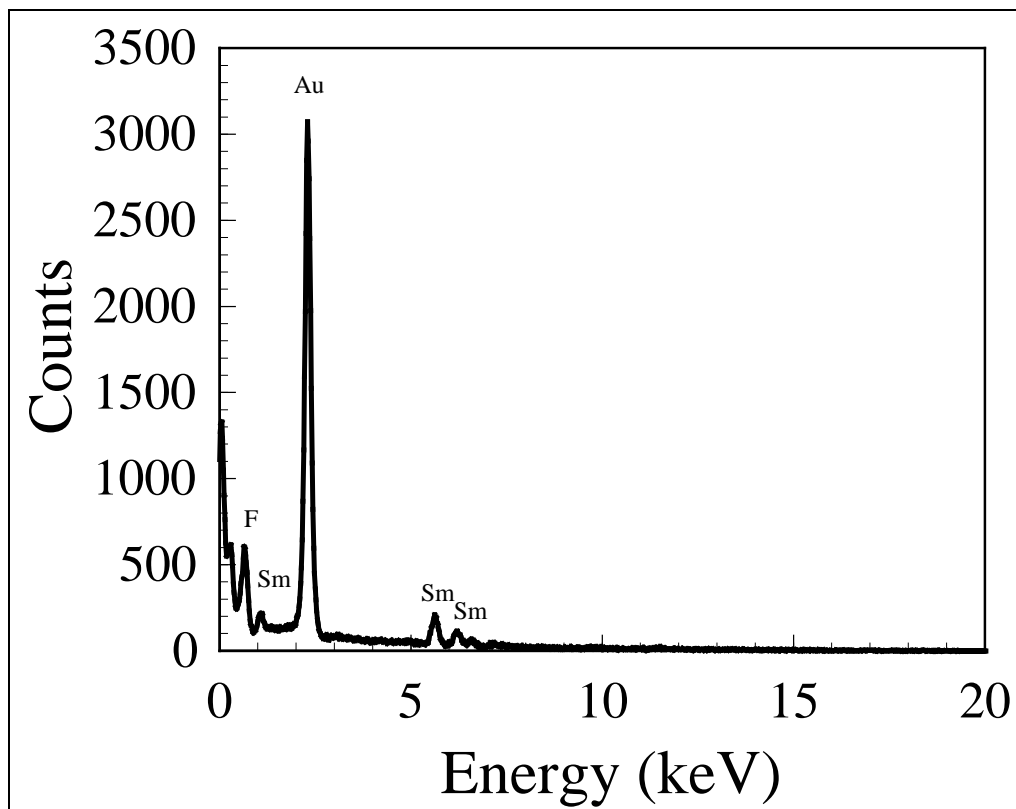
Figure 4.9. EDS of samarium deposit on the gold electrod.

In Figure 4.9, it can be seen that the EDS analysis shows the presence of samarium onto the surface of the gold electrode, with no indication of oxygen at 5.5 keV. Given the EDS is able to detect oxygen content down to 0.5 weight percent, this is further support of samarium metal deposition.[93]   Additionally, the occurrence of fluorine in the spectrum is further support to the proposed mechanism of Sm deposition through removal of the TFSI ligand during the reduction at the electrode surface. If they were present, the EDS would successfully be able to identify many of the other elements present in the TFSI species including oxygen, nitrogen, and sulfur. Elements lighter than carbon cannot

be seen.[94] The ionic liquid is very viscous, and the electrode was intentionally left partially wet during transport, and then cleaned just before analysis.

4.4 Conclusions

In this research, the extraction of samarium from the starting material of $Sm(TFSI)_3$ in water into an RTIL solution was shown to be extremely effective. The extraction was achieved with no additional extractant added to the system, but was found to be dependent on the pH of the aqueous layer. An extraction efficiency of 100 % was found to be possible within 5 hours at and above pH 9.0.

Once the samarium was extracted into the RTIL solvent, studies of the oxidative and reductive properties of the species indicated that deposition of a Sm-TFSI complex occurs at -0.33 V versus NHE. As the scan continues to more negative potentials, all of the TFSI is removed from the Sm-TFSI that was initially deposited at the surface,. Sm(0) is found at the electrode surface by -1.5 V versus NHE, which is over 1.0 V more electropositive than previous literature reports of samarium in aqueous based systems.[91] The samarium deposit was successfully obtained and measured using SEM and EDS. The deposit was confirmed to be samarium metal, with no visible oxygen at the electrode surface as indicated by the EDS analysis of multiple spots. Most importantly, this research shows the potential of the RTIL solvent to be used as both the extraction solvent as well as the electrochemical solvent from which separation via electrodeposition of f-elements has proven feasible.

Chapter 5: Argon assisted dissolution of uranyl carbonate

5.1 Introduction

Uranyl carbonate species are often studied because of their ability to interact in natural environments, their strong interaction of the metal with the ligand, and the ability to manipulate carbonate concentration through control of atmosphere.[95] For uranium found in nature, UO_2^{2+} has been reported to be a very mobile species that is easily sorbed to organic materials.[96] As a result of this high mobility in natural environments, as well as concerns with potential dangers from migration from uranium mines and nuclear waste, obtaining a more thorough understanding of the uranyl species is extremely important.[96]

Carbonates are the primary uranium species under basic conditions, therefore this high valence uranium complex may be readily found in nature.[96] As a result of the high stability of the complex, carbonate extractions are an advantageous method employed for uranium separations.[96] In addition, uranyl carbonates have been reported to have a dominating affect when considering speciation under the aqueous conditions as reported at the Hanford site when examining the Vadose Zone pore waters.[97] In those studies, the researchers noted that the uranyl carbonate was the primary mobile species that was observed migrating beneath the surface. Finally, uranyl carbonate is a component of some reprocessing schemes, in which the UO_2 is separated by precipitation as uranyl carbonate.[98]

A more detailed understanding of the dissolution of UO_2CO_3 and the speciation and electrochemical behavior of soluble species in the RTIL, [Me3NnBu][TFSI], is then

useful for both environmental and reprocessing purposes. However, there must be appreciable solubility of the actinide species in the RTIL to be useful for any envisioned applications. The direct dissolution and electrochemical reclamation of f-elements from complex mixtures are also relevant in understanding the fundamental application of RTIL solutions in reprocessing, solvent extraction, reclamation, and sequestering of nuclear waste and reusable materials.

This chapter presents the evaluation of the dissolution of UO_2CO_3 in neat and acidified RTIL [Me_3N^nBu][TFSI] using UV/VIS spectroscopy and liquid scintillation counting. The properties of the carbonate ligand are specifically exploited to increase the solubility of the f-element species into the RTIL. The complexation and speciation of the soluble uranium species is evaluated providing insights into the dissolution mechanism of UO_2CO_3 and interaction of U(VI) species with RTIL solution. Finally, electrochemical measurements are used to probe the oxidation/reduction properties of soluble uranium and to evaluate the potential dependent deposition from RTIL.

5.2 Methods

5.2.1 Reagents

All reagents used were reagent grade. Lithium bis(trifluoromethanesulfonyl)imide (LiTFSI) salt was purchased from VWR. The bis(trifluoromethanesulfonyl)amine (HTFSI) was purchased from Sigma Aldrich. All purchased reagents were used as received. See Chapter 3 for further details on the synthesis of the RTIL (Section 3.1) and the uranyl carbonate (Section 3.2).

5.2.2 Dissolution of UO₂CO₃

The reaction was initialized after placing 0.3 g of finely ground uranyl carbonate containing 12.2%   by mass ^{233}U along with 55.4 g of [Me₃NⁿBu][TFSI] in a 50 mL centrifuge tube (See Section 3.2 for further information on the isotopic ratio). Constant stirring of the reaction vessel contents was executed using a spin vane with a continuous argon gas purge (Figure 5.1).
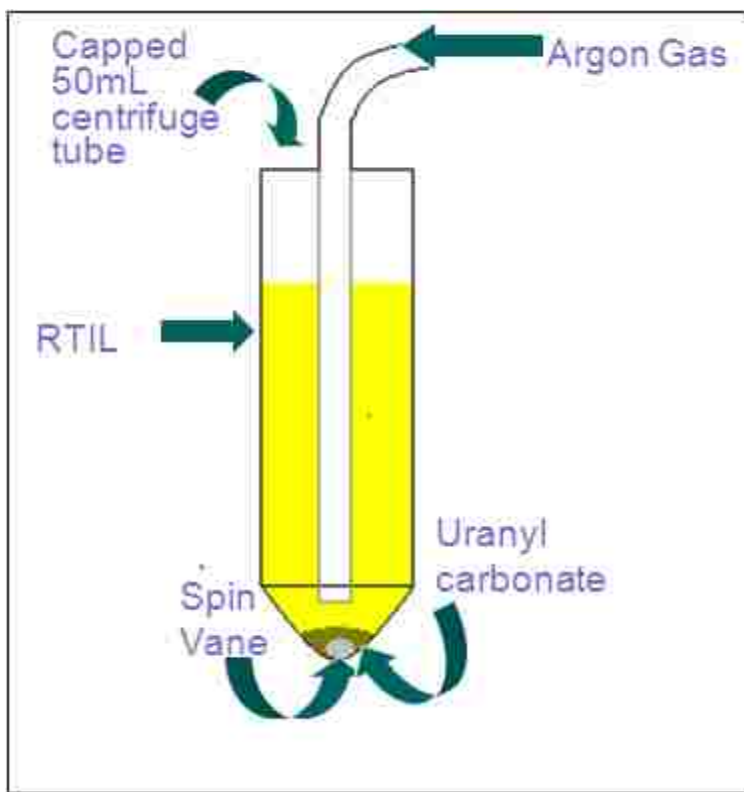
Figure 5.1.   Graphic schematic of the experimental setup for the uranyl carbonate dissolution.

The centrifuge tube was disconnected from the gas and centrifuged for 10 minutes at given time intervals. An aliquot was removed and saved for analysis via liquid

scintillation counting, UV-Vis spectroscopy, cyclic voltammetry, and linear sweep voltammetry (LSV). These methods were described in detail in Chapter 2. Aliquots were removed and analyzed over the course of 80 days.

5.3 Discussion

5.3.1 Solubility of UO_2CO_3 in $[Me_3N^nBu][TFSI]$

The dissolution of UO_2CO_3 in stirred RTIL was evaluated after one week in the absence of an argon gas purge. There was no observable response above the baseline for soluble uranyl using either UV/Vis or liquid scintillation analysis for this sample. The solubility of UO_2CO_3 and formation of $UO_2(TFSI)_2$ complex in $[Me_3N^nBu][TFSI]$ was also monitored using UV/Vis spectroscopy after initiating an argon purge of the system. Figure 5.2 presents selected results of this experiment.
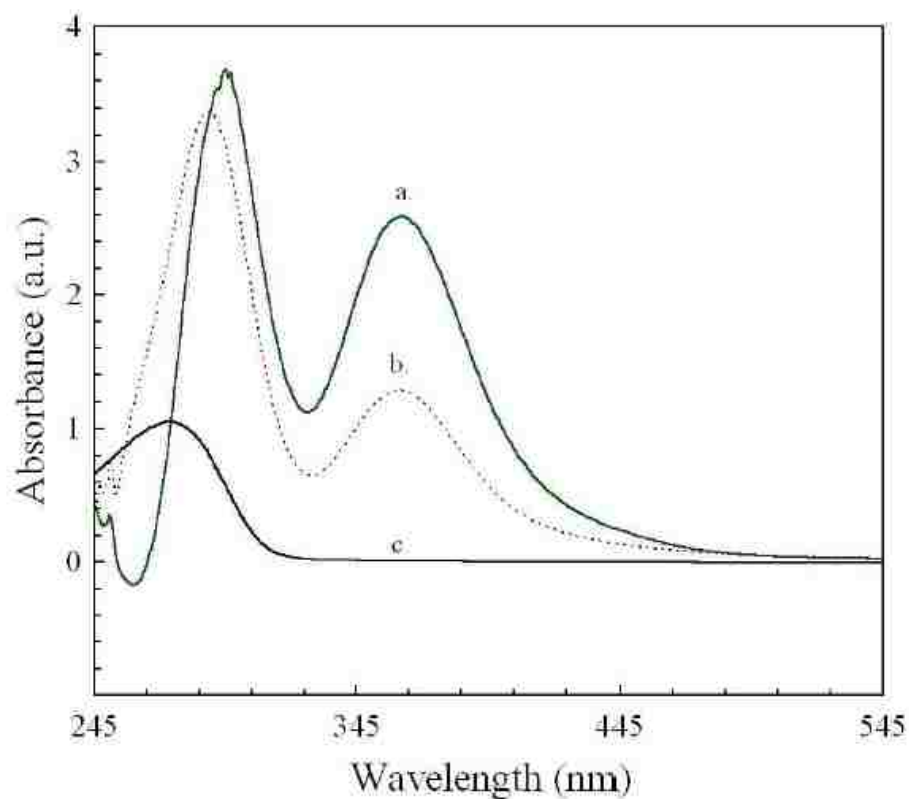
Figure 5.2. UV-Vis spectra of a. Soluble 96 μM uranyl in [Me$_3$N^{n}Bu][TFSI] after twenty-eight days of argon purging, b. Soluble 60 μM uranyl (diluted from 6.4 mM) in [Me$_3$N^{n}Bu][TFSI] after addition of HTFSI. and c. HTFSI in [Me$_3$N^{n}Bu][TFSI].

The increase in solubility with argon gas purge indicates that the dissolution may be tied to the displacement of CO_3^{2-} from the UO_2CO_3. However, displacement of CO_3^{2-} should only be influenced by argon gas if the carbonate ion is converted to H_2CO_2 followed by decomposition to water and CO_2 which can then be degassed from solution. Free UO_2^{2+} in the absence of the carbonate ligand can then form a complex with TFSI depleting the anion from the RTIL. The lack of protons available in the RTIL hinder the dissolution of the UO_2CO_3 in [Me$_3$N^{n}Bu][TFSI]. Thus dissolution is limited based on the dissociation of water which has minimal concentration in the system (0.285 % by weight, see Section 3.1 for RTIL water content determination). An increase in proton

concentration should produce carbonic acid and hastening dissolution in the RTIL, Scheme 5.1.

$$2 \; F_3C-\overset{\overset{O}{\|}}{\underset{\underset{O}{\|}}{S}}-\overset{\ominus}{N}-\overset{\overset{O}{\|}}{\underset{\underset{O}{\|}}{S}}-CF_3 \quad \longrightarrow \quad UO_2(TFSI)_2$$

$$UO_2CO_3 \; (s) \; + \; 2H^+ \quad \longrightarrow \quad UO_2^{2+} \; + H_2CO_3$$

$$H_2O \; + \; CO_2 \quad \xrightarrow{\; Ar \; (g) \;} \quad CO_2 \; (g)$$
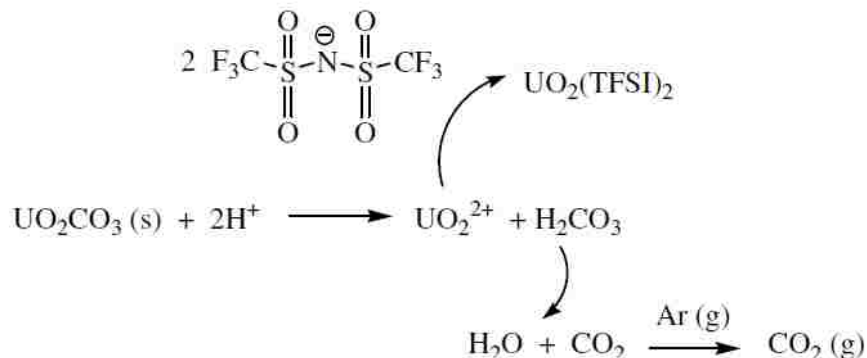
Scheme 5.1. Possible dissolution mechanism for UO_2CO_3 in $[Me_3N^nBu][TFSI]$

The dissolution of UO_2CO_3 (s) was examined after addition of HTFSI to the RTIL to evaluate the proposed mechanism. Solid HTFSI appeared to be fully dissolved upon visual inspection after adding to the RTIL containing solid UO_2CO_3. The UV/Vis spectrum was examined to ensure the complex formation was consistent with the species formed in the absence of acid.

For example, Figure 5.2a shows the spectra for UO_2CO_3 dissolution in RTIL without acid at 28 days for comparison with acidified UO_2CO_3 in RTIL in Figure 5.2b. Minor spectral differences are observed after the addition of HFTSI in terms of the shape and wavelengths for the absorbances for both bands. The decrease in TFSI anion during complex formation is likely not observed in Figure 5.2b because additional TFSI anion is provided in the form of acid. For comparison, the spectrum of HTFSI in $[Me_3N^nBu][TFSI]$ is also provided, Figure 5.2c. The spectrum shows a single band at ~275 nm associated with the TFSI ligand consistent with the band observed for acidified

RTIL. This band is also consistent with the observed location of the TFSI anion from the discussion of $Sm(TFSI)_3(H_2O)_3$ in water from Section 3.3.4. The data again supports the lower wavelength band corresponding to absorbance associated with the TFSI anion in the RTIL and the proton concentration. The spectra also suggest that the addition of HTFSI influences the direct dissolution of UO_2CO_3, in RTIL. This could be based on the loss of carbonate ligand through the formation and decomposition of carbonic acid. Additional experiments would be necessary to monitor the formation of carbonic acid to verify this statement.

An additional consideration is that of reduction of the U(VI) species during the dissolution process. However, given the preferential hexavalent oxidation state of uranium in aqueous solution[96] it is unlikely that there would have been a change in oxidation state during the dissolution process. Additionally, for the uranium to reduce, the $TFSI^-$, $Me_3N^nBu^+$, or the CO_3^{2-} would need to oxidize. A strong reducing agent would be required to reduce the U(VI) species. It is doubtful that any of the available species would have this capacity. Assuming there is no change in oxidation state of the uranium species it is expected that the $UO_2(TFSI)_2$ complex could form.

The resulting spectra of the RTIL soluble uranium species (Figure 5.2) are markedly different than the spectra that would be expected of uranyl in an aqueous solvent. In the RTIL, the fine structure that is observed in the aqueous solvent is lost. Figure 5.3 provides an example of the spectrum of uranyl nitrate dissolved into water for comparison.
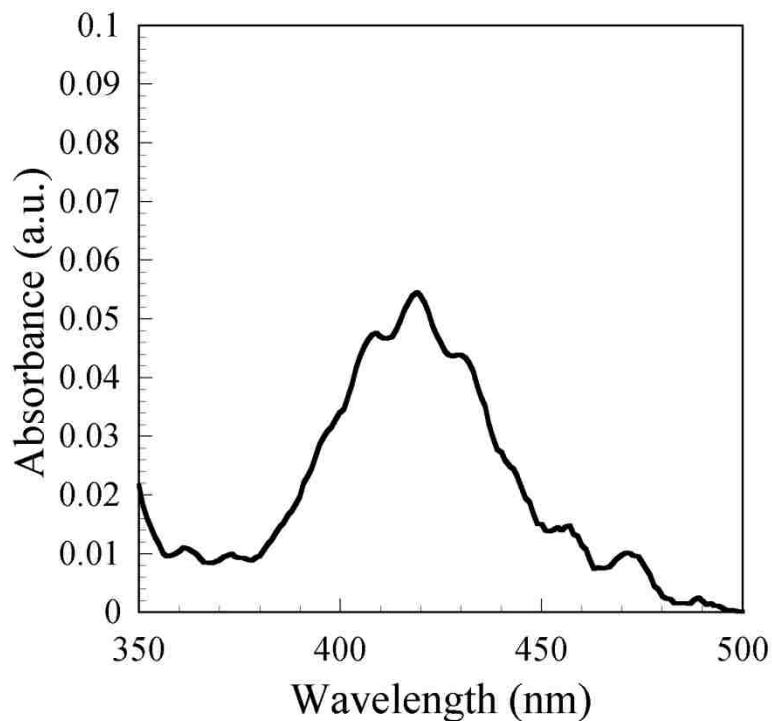
Figure 5.3. Representative UV-Vis spectrum of uranyl under aqueous conditions.

As demonstrated in Figure 5.3, typically free UO_2^{2+} absorbance is observed between 414 – 425 nm in aqueous media.[99,100] Absorbance below 500 nm is consistent with soluble uranium in the hexavalent oxidation state.[100] It can be noted by comparing the spectra in Figure 5.2 to that of Figure 5.3 that the shape of the bands resulting from soluble uranyl in the RTIL has lost the fine structure that is visible in the aqueous solution. Additionally, the wavelength for the soluble uranium species' absorbance in RTIL (359 nm) is lower than those reported for U(VI) species.   However, the uranyl species has been shown to exhibit a strong absorbance below 400 nm in the NaCl-2CsCl eutectic systems.[27] Other researchers have also reported absorbances from 190 to 400 nm of uranyl complexes formed with Schiff bases using an acidic catalysis. They concluded that the bands in this region were from the U(5f)-Schiff Base(O) ligand to metal charge transfer band.[101]

The UV-Vis spectroscopic responses for various times are provided in Figure 5.4. The spectra were collected using a blank cell containing pure RTIL, $[Me_3N^nBu][TFSI]$, and a sample cell containing aliquots of soluble uranium in RTIL purged with argon gas. Any increase in absorbance represents either the emergence of new species in the solution due to the dissolution of the $UO_2CO_3(s)$ or a change in chemistry of the RTIL itself. In contrast, negative absorbance is potentially indicative of the depletion of RTIL species from the solution due to possible complex formation with soluble uranium.

From the Figure, a shift can be observed in which band (287 or 359 nm) has the higher maximum absorbance as the number of days are increased. In addition, the amplitude of the negative absorbance observed at 268 nm decreases during the course of the time period observed.
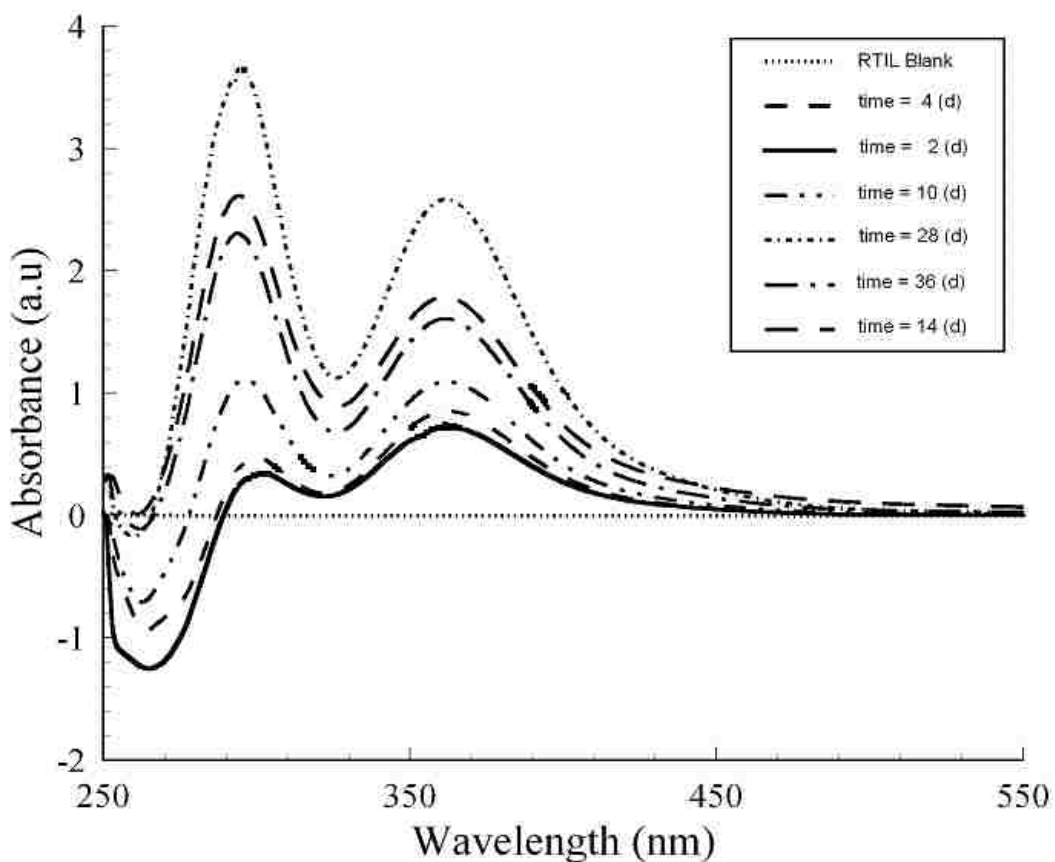
Figure 5.4. UV-Vis spectra of [Me3N^{n}Bu][TFSI] background and soluble uranyl in [Me$_3$N^{n}Bu][TFSI] after various days of argon purging. The uranyl concentrations as obtained from LSC for each time are provided in Table 5.1.

Below 1 a.u, the band at 359 nm has a higher absorbance than the band at 287 nm. At approximately 1 a.u., both bands appear to have very similar maxima; however by 2 a.u., the band at 287 nm has a higher absorbance than the band at 359 nm. There appears to be a correlation between the negative absorbance and maximum absorbance observed, however the inability to deconvolute the overlapping bands with the available data obtained in this dissertation prevents a valid continuation of this analysis. The TFSI ligand has been reported to form complexes both through the nitrogen center as well as

114

the sulfonyl oxygens,[68] thus the two bands could represent the formation of a uranium-TFSI complex through two different atoms within the TFSI complex.

Given the observed changes in the resulting spectrum of the soluble uranium species in the RTIL, a secondary analysis method was utilized. Comparison of the absorbance and LSC data is a useful method for determining if the dissolution and increase UV/Vis absorbance is due to soluble uranium in the RTIL. Before attempting to correlate these two methods, a single UV-Vis band was selected by first examining each individual band.

The absorbance band at 287 nm is well below the typically reported absorbance wavelengths of uranium in aqueous or RTIL solution. Therefore the band is not likely solely due to complex formation between soluble uranium and TFSI. In addition, the band at 287 nm presented maximum absorbance well above 3. In regions of high absorbance, the linear relationship of concentration with molar absorptivity as written in Beer's law becomes questionable. Thus absorbances above 3 were not ideal for a correlation with uranium concentration in solution. The band at 359 nm was then selected for making comparisons against the LSC data. Unfortunately, to perform UV-Vis analysis, LSC, and electrochemical analysis, an aliquot of at least 1.5 mL was required. As a result, not all LSC samples were analyzed with both techniques. A smaller fraction of samples, obtained at 2, 4, 10, 14, 21, 28, and 36 days were selected to have large enough sample volumes removed in which both LSC and UV-Vis techniques could be performed. Therefore, these are the only samples that were used for the comparison of techniques and the derivation of the molar absorbtivity.

The time dependent concentration for the argon assisted dissolution of UO_2CO_3 in RTIL is provided in Figure 5.5 and Table 5.1 based on LSC measurement of the total uranium concentration. As explained above, a portion of these samples were also utilized for obtaining the UV-Vis spectra provided in this section. The Table presents the relevant sample information necessary to determine the total uranium concentrations as demonstrated in Chapter 3. Those samples that were also analyzed with UV-Vis are italicized.

Table 5.1. LSC results and relevant sample data used for calculations. Italicized results indicate that both UV-Vis and LSC was performed on the same sample.

Time (d)	Sample Mass (g)	Sample V (L)	DPM from LSC	A (Bq)	Atoms	Mols	[U-233] (M)	[Total U] (μM)
0	0.0863	6.12E-05	0	0.00	0.00E+00	0.00E+00	0.00E+00	0.00
2	*0.0872*	*6.18E-05*	*104*	*1.74*	*1.26E+13*	*2.09E-11*	*3.38E-07*	*2.77*
4	*0.0637*	*4.52E-05*	*217*	*3.61*	*2.62E+13*	*4.35E-11*	*9.63E-07*	*7.89*
6	0.0562	3.99E-05	795	13.25	9.60E+13	1.59E-10	4.00E-06	32.80
10	*0.0594*	*4.21E-05*	*369*	*6.15*	*4.45E+13*	*7.40E-11*	*1.76E-06*	*14.39*
14	*0.0577*	*4.09E-05*	*878*	*14.64*	*1.06E+14*	*1.76E-10*	*4.31E-06*	*35.30*
17	0.0399	2.83E-05	1840	30.67	2.22E+14	3.69E-10	1.30E-05	106.93
21	*0.0339*	*2.40E-05*	*932*	*15.54*	*1.13E+14*	*1.87E-10*	*7.78E-06*	*63.77*
28	*0.0260*	*1.84E-05*	*1068*	*17.80*	*1.29E+14*	*2.14E-10*	*1.16E-05*	*95.25*
36	*0.0880*	*6.24E-05*	*1244*	*20.73*	*1.50E+14*	*2.50E-10*	*4.00E-06*	*32.78*
42	0.0863	6.12E-05	6317	105.29	7.63E+14	1.27E-09	2.07E-05	169.73
49	0.0842	5.97E-05	7013	116.88	8.47E+14	1.41E-09	2.36E-05	193.12
56	0.0936	6.64E-05	7223	120.39	8.72E+14	1.45E-09	2.18E-05	178.93
78	0.1153	8.18E-05	8505	141.76	1.03E+15	1.71E-09	2.09E-05	171.04
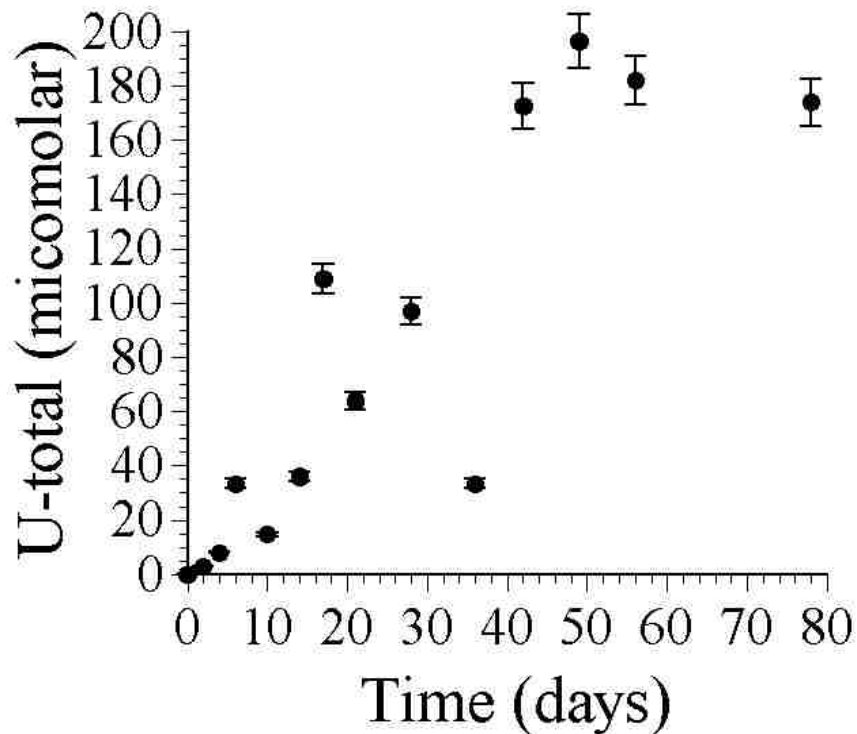
Figure 5.5. Total concentration of soluble uranyl in [Me₃NⁿBu][TFSI] as a function of time from liquid scintillation counting as shown in Table 5.1.

It is interesting to note that the dissolution of UO_2CO_3 and increased solubility of the uranium in [Me₃NⁿBu][TFSI] is influenced by argon degassing of the solution within two days. It is clear from the plot that the dissolution of UO_2CO_3 in RTIL is relatively slow with the maximum concentration of ~195 μM at approximately 50 days. It can also be seen from the Figure that the concentration does not increase steadily over time, but has several distinct decreases, including a fairly substantial decrease at 10 and 36 days. The experiment was run in triplicate and the concentration was consistently lower at this time period, indicating that it is not a statistical outlier. It is not clear why the soluble uranium would decrease at this point. However, a comparison using the UV/Vis

absorbance data shown in Figure 5.5 with the LSC data presented in Table 5.2 at the

same time is consistent with the observed decrease (Figure 5.6).

y = mx + b		
	Value	Error
y	0.79198	0.10459
x	21149	2204.9
Chisq	0.16192	N/A
R	0.97389	N/A
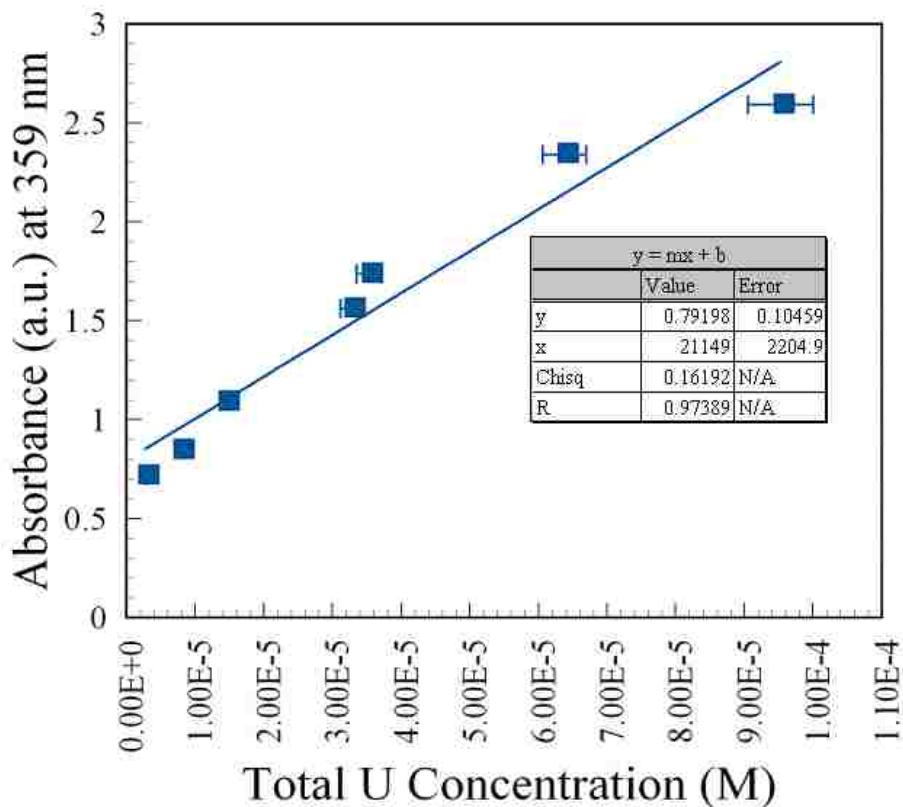
Figure 5.6. Plot of absorbance maxima at 359 nm from the spectra presented in Figure 5.4 versus total concentration of soluble uranium from LSC measurements shown in Table 5.1. This information is also listed together in Table 5.2.

Table 5.2. UV-Vis absorbance at 359 nm and LSC uranium concentrations for all samples that were analyzed by both techniques.

Days	Absorbance (A) at 359nm	[U-total] (M) - Determined from LSC
2	0.717	2.77E-06
4	0.846	7.89E-06
10	1.09	1.44E-05
14	1.736	3.53E-05
21	2.34	6.38E-05
28	2.59	9.53E-05
36	1.56	3.28E-05

The LSC and UV-Vis data presented above initially suggests that the absorbance at 359 nm is linked to the dissolution of UO_2CO_3 in RTIL and the corresponding increase of soluble uranium species. In addition, an estimate of the molar absorptivity can be obtained from the plot. The molar absorptivity estimated from the slope of the line using the linear regression shown in Figure 5.6 was shown to be $2.1\times10^5 \pm 2.2\times10^4$ L*mol^{-1}*cm^{-1}. However, the molar absorptivity value is at least an order of magnitude higher than many previous uranium species.[102] The magnitude of the molar absorptivity and the shift to lower wavelengths as compared to the previously reported free uranyl ion suggests that additional analysis should be performed before concluding that this is the correct extinction coefficient for uranium in the RTIL. Additionally, as described above, the atoms (nitrogen or oxygen) within the TFSI ligand that are responsible for the formation of the uranium-TFSI complex must be considered.

To further test the molar absorptivity as determined from the linear regression shown in Figure 5.6, it was recalculated individually for each sample using Beer's Law:

$$A = \varepsilon bc$$

$$\varepsilon = \frac{A}{bc} \qquad\qquad\qquad \text{Equation 5.1}$$

Where:

> A = Absorbance at 359 nm
> b = path length = 1 cm
> ε = Molar Absorbtivity
> c = concentration, M

The data for each sample is provided in Table 5.3. These results were also plotted to observe the change in molar absorptivity with time (Figure 5.7):
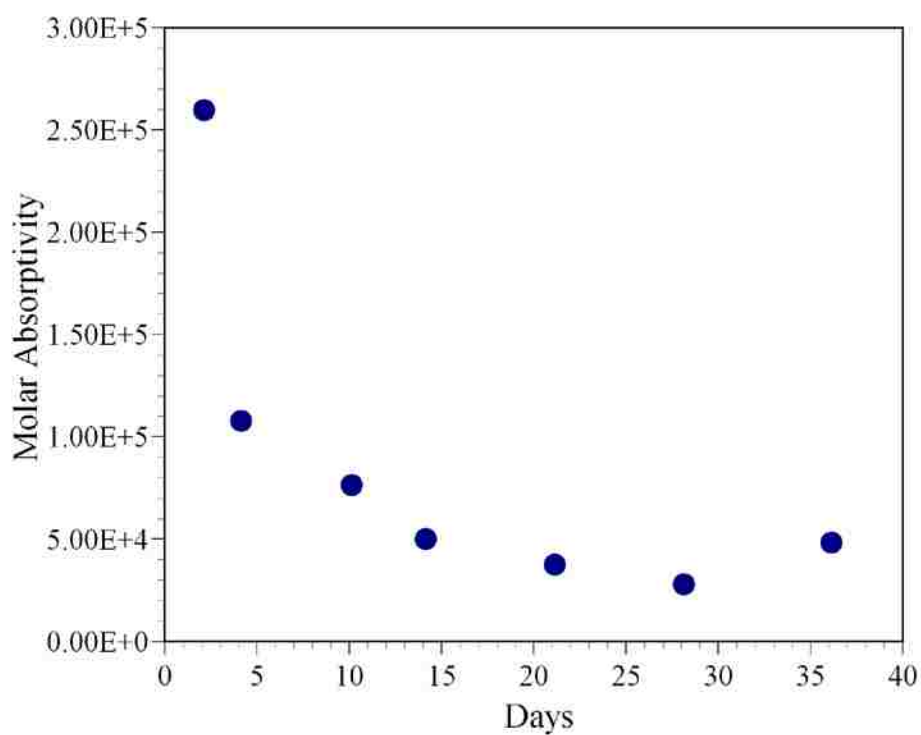
Figure 5.7. Molar absorptivity calculated for each sample, plotted as a function of time (days).

It is interesting to note that the molar absorptivity appears to initially fall dramatically in the first 4 days of the experiment, and then it steadily decreases through

120

28 days. The final point, at 36 days, appears to slightly increase, but it could also indicate reaching a plateau. Additional data points would be required to ascertain if this is the case.

Table 5.3. Molar absorptivities calculated at A=359 nm for each sample using the sample information shown in Table 5.2.

Days	Absorbance (A) at 359nm	[U-total] (M) - Determined from LSC	Molar Absorptivity
2	0.717	2.77E-06	2.59E+05
4	0.846	7.89E-06	1.07E+05
10	1.09	1.44E-05	7.57E+04
14	1.736	3.53E-05	4.92E+04
21	2.34	6.38E-05	3.67E+04
28	2.59	9.53E-05	2.72E+04
36	1.56	3.28E-05	4.76E+04
		Average	8.61E+04
		Standard Deviation	8.08E+04

It can be seen from Table 5.3 that the average molar absorptivity calculated by using Equation 5.1 is $8.61 \times 10^4 \pm 8.08 \times 10^4$ L*mol^{-1}*cm^{-1}. This can be compared with the molar absorptivity as determined from the linear regression, 2.11×10^5 L*mol^{-1}*cm^{-1}. If correctly assigned, these values should be in agreement. However, they are 86% different from each other. In addition, it can be seen from the table, that the initial molar absorptivity, at 2 and 4 days, are much closer to the linear regression determination. As the experiment continues, the molar absorptivity decreases. This was also seen in Figure 5.7. These results suggest that while the emergent band in Figure 5.4 at 359 nm may be related to the increase of uranium in the RTIL solution through the increase of another species, such as TFSI, it is not directly from the uranium itself.

Further spectroscopic analysis was performed using a new sample in which additional HTFSI acid was added directly to the RTIL solution containing UO_2CO_3 solid. The experimental set up detailed in Section 5.2.2 was otherwise mirrored. The initial results reflected an additional emergent band at 465 nm. The location of this band was more consistent with previously observed uranyl in solution.[99,100] However the maximum absorbances below 400 nm exceeded 10 a.u., which prevented further use of this raw data. The sample was diluted to obtain lower absorbances, but unfortunately this also caused the emergent band to no longer be visible. Further experiments would be necessary to validate that the preliminary observed band at 465 nm was the uranyl response in the RTIL solution.

It would have been useful to have LSC and UV-Vis data for every sample point, but the volume required to obtain a sample for UV-Vis analysis was much greater than the volume that was required for LSC analysis. The sample aliquots removed during the experimental procedure were designed to not overly perturb the original system. The goal was to have less than 10% of the total starting volume removed during the course of the entire experiment. As such, only a portion of the samples were examined with both techniques. The emergent band viewed in the raw data of the undiluted spectrum of UO_2TFSI_2 with added HTFSI in RTIL provides further question to the validity of the assignment. The bands at 287 and 359 nm are more likely indirectly caused from increasing TFSI in solution, which results from the UO_2TFSI_2 complex formed during the dissolution process as presented in Scheme 5.1 through the displacement of the carbonate ligand from the uranyl by acidification. Additional spectra would be useful in confirming that the band assignments, but this experiment was not performed during this dissertation.

5.3.2 FTIR Spectroscopy

Complex formation between the UO_2^{2+} cation and $TFSI^-$ anion has not be extensively studied using IR spectroscopy. However, theoretical calculations and experimental IR spectroscopy have been performed on the TFSI ligand and LiTFSI salt providing band assignments for the SO_2, CF_3, SNS, and CS functional groups.[47,103] The use of FTIR spectroscopy in our studies is further complicated by the high concentration of the RTIL relative to the soluble $UO_2(TFSI)_2$ that would be present. The FTIR spectra of LiTFSI, RTIL [Me_3N^nBu][TFSI], and UO_2CO_3 in RTIL [Me_3N^nBu][TFSI] after 40 days are presented in Figure 5.8.
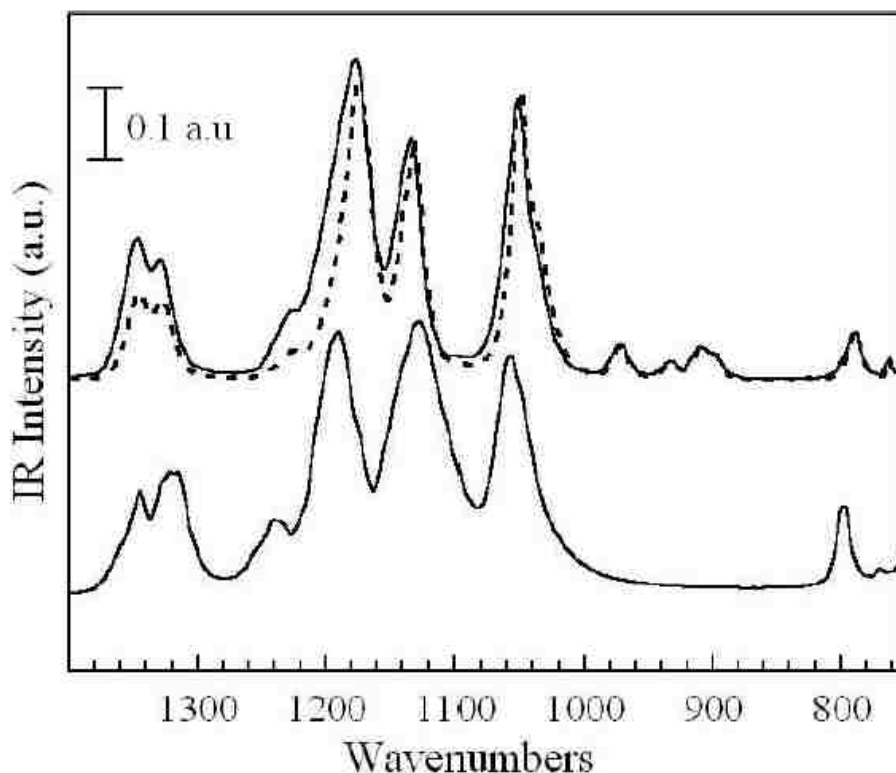
Figure 5.8. FT-IR spectra of solid LiTFSI (bottom), RTIL [Me_3N^nBu][TFSI] (top, dashed line) and soluble UO_2^{2+} in [Me_3N^nBu][TFSI] (top, solid line).

The characteristic bands from 1050 – 1400 cm^{-1} encompass the TFSI functional groups SNS, SO_2, and CF_3. For comparison, the spectral bands from 900 – 1000 cm^{-1} are indicative of the Me_3N^nBu cation. These characteristic IR bands for the cation are absent in the spectra of LiTFSI confirming the assignments. The neat RTIL solution compares favorably with the literature with bands for SO_2 at 1345, 1327, and 1131 cm^{-1}, respectively. The CF_3 and SNS functional groups can be observed at 1174 and 1049 cm^{-1}, respectively in the IR spectrum. Similarly, the band assignments at 1347, 1329, and 1132 cm^{-1} are given to the SO_2 functional group present in the solvent RTIL, $[Me_3N^nBu][TFSI]$. The CF_3 and SNS functional groups are observed at 1179 and 1051 cm^{-1}. Table 5.4 presents the comparison of these bands. The modest shift to higher wavenumbers for all the bands associated with the TFSI anion is certainly not conclusive proof that UO_2^{2+} and TFSI form a complex.

Table 5.4. Comparison of the location FT-IR bands of RTIL containing soluble UO_2^{2+} against literature values for neat RTIL.

Functional Group	Wavelength (cm^{-1})	
	Product	Literature[47,103,68,104]
SO_2	1345	1323
	1327	1307
CF_3	1218	1221
	1179	1198
SO_2	1131	1138
SNS	1051	1055
CH_3	972	969
	935	953
	910	947

However, the shape and change in relative intensity of the bands is indicative of the formation of the $UO_2(TFSI)_2$ complex.[47,103] Previous reports have found that the TFSI anion can coordinate with a metal center through the sulfonyl oxygens as well as the nitrogen center.[47,103,68,104] The SO_2 doublet has been attributed to the symmetric and asymmetric stretching and changes in the intensity and shape of the two bands can be ascribed to changes in concentrations of the conformers when the TFSI ligand is bound.[103]

The FTIR spectra of RTIL $[Me_3N^nBu][TFSI]$, UO_2CO_3 in RTIL $[Me_3N^nBu][TFSI]$ after 40 days, and $UO_2(TFSI)_2$ in RTIL $[Me_3N^nBu][TFSI]$ after addition of HTFSI are presented in Figure 5.9.
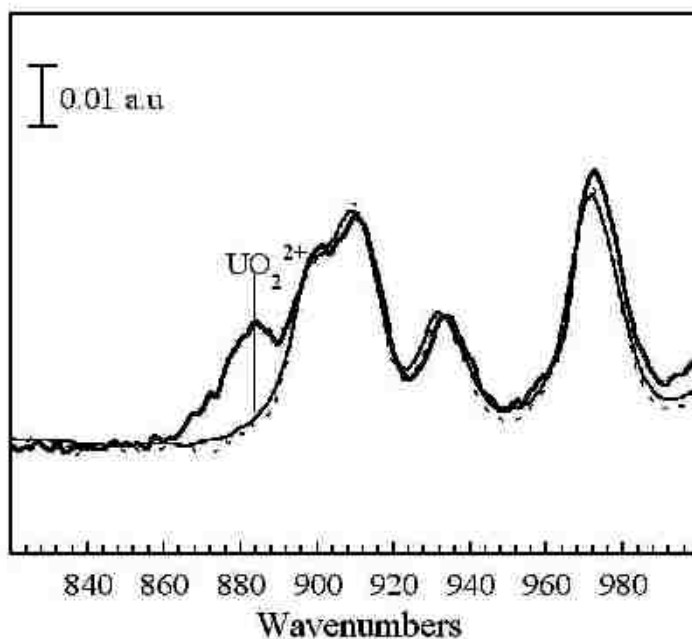
Figure 5.9. FT-IR spectra of RTIL $[Me_3N^nBu][TFSI]$ (dashed line), soluble UO_2^{2+} in $[Me_3N^nBu][TFSI]$ (solid line), and soluble uranium in $[Me_3N^nBu][TFSI]$ after the addition of HTFSI (solid line, bold).

125

The IR spectra for the $UO_2(TFSI)_2$ in RTIL $[Me_3N^nBu][TFSI]$ and UO_2CO_3 in RTIL $[Me_3N^nBu][TFSI]$ after addition of HTFSI are indistinguishable in the spectral regions between 1050 and 1400 cm^{-1} with respect to band position and relative intensity. In contrast, the spectral region associated with soluble UO_2^{2+} shows an increase in band intensity from 850 – 900 cm^{-1}. There is no direct comparison to soluble UO_2^{2+} in RTIL available in the literature. However, there is data for uranyl formed from laser ablated uranium with gaseous H_2O_2 which note emergent bands between 700 and 900 cm^{-1} encompassing neutral deposits of UO_3, UO_2 and UO, respectively.[105] All of these species are oxide forms of uranium, which are a suitable for fundamental comparison with the oxygen containing uranium species examined in this Chapter.

The uranyl functional group also has vibrations reported around 914cm^{-1} in the complex $UO_2ClI \cdot 3DMSO$. Previous literature also noted that the bonding atom in the uranyl functional group was very sensitive to the complex in which it is bound to.[106] Therefore the emergent band centered at 884 cm^{-1} in Figure 5.9 is designated as UO_2^{2+} for $UO_2(TFSI)_2$ in RTIL $[Me_3N^nBu][TFSI]$ after addition of HTFSI. This data also demonstrates that a much higher concentration of soluble UO_2^{2+} is achieved with the addition of HTFSI through the direct dissolution of UO_2CO_3, when compared to the pristine RTIL solution.

5.3.3 Electrochemistry

The electrochemical response of soluble uranium as a function of time is provided in Figure 5.10.
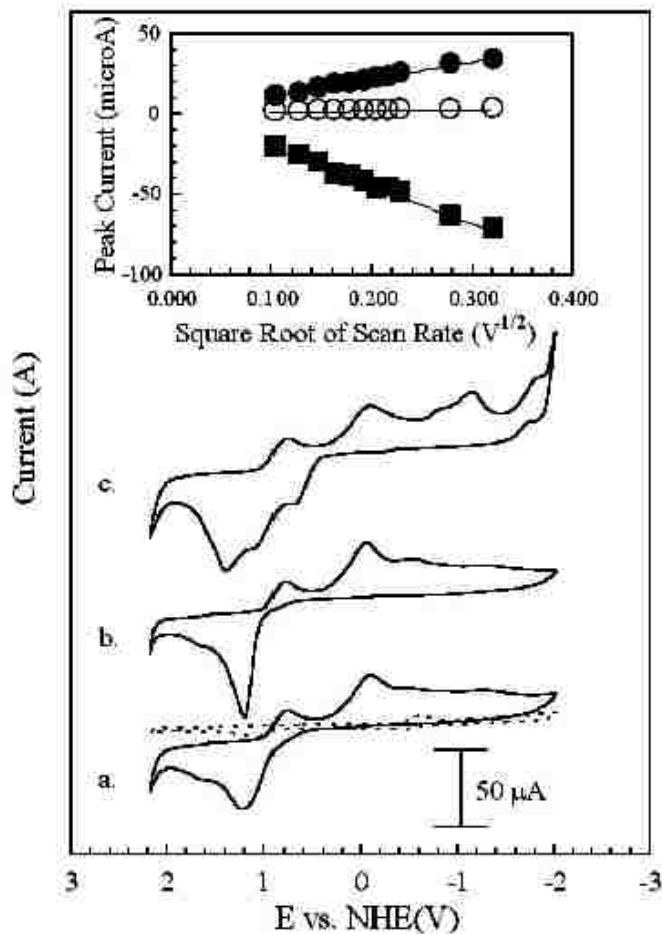
Figure 5.10. Cyclic voltammetric response of, RTIL [Me$_3$N^{n}Bu][TFSI] (dashed line), a. Soluble UO$_2^{2+}$ in [Me$_3$N^{n}Bu][TFSI] after two days of argon purge, b. Soluble UO$_2^{2+}$ in [Me$_3$N^{n}Bu][TFSI] after four days of argon purge, and c. Soluble UO$_2^{2+}$ in [Me$_3$N^{n}Bu][TFSI] after forty days of argon purge. Scan rate =100 mV/s. Inset: Scan rate dependence for voltammetric waves for soluble UO$_2^{2+}$ in [Me$_3$N^{n}Bu][TFSI] after two days of argon purge.

Following centrifugation, an aliquot without any visible UO$_2$CO$_3$(s) was removed from the solution of [Me$_3$N^{n}Bu][TFSI] to obtain each cyclic voltammogram at a given time. For clarity, only select times are displayed in the figure. The background for pure [Me$_3$N^{n}Bu][TFSI] is provided in the figure (dashed line). The cyclic voltammetric response for UO$_2$(TFSI)$_2$ in RTIL [Me$_3$N^{n}Bu][TFSI] after two days of purging shows

discernable oxidation/reduction processes associated with the soluble uranium species in RTIL, Figure 5.10a. A similar voltammetric response is observed for the RTIL solution after 4 days in Figure 5.10b. There are two reduction waves that can be observed in the voltammetric response at 0.75 V and -0.10 V. A single oxidation wave is observed at 1.21 V in the cyclic voltammetric response.

Previous electrochemical studies of uranium ions in RTIL solutions have been conducted using alkyl imidazolium cations with various inorganic anions. In some cases species such as UCl_6^{2-} are directly incorporated into the RTIL after forming a complex with the common cation. For example the oxidation/reduction of UO_2^{2+} has been examined in 1-butyl-3-methyl-imidazolium RTIL solutions with various anions.[71,107] The electrochemical response of UO_2^{2+} in 1-butyl-3-methylimidazolium nonafluorobutane-sulfonate, bmiNfO shows overlapping waves at negative potentials consistent with multiple reduction processes.[108] The electrochemical processes were assigned to the multi-step reduction of hexavalent to tetravalent uranium via two single electron processes followed by the direct deposition of $UO_2(s)$ at the electrode surface.

The study also indentifies a single, large oxidation wave which was attributed to the oxidation of multiple uranium species. Previous assignment of the oxidation/reduction processes associated with the voltammetric response has been complicated due to the lack of literature associated with the reduction of free or complexed UO_2^{2+} in RTIL. In addition, mixed ligand complexes have been previously suggested to account for the multiple voltammetric waves observed.[16]

Although the multi-step reduction and single oxidation wave observed for UO_2^{2+} in $[Me_3N^nBu][TFSI]$ are consist with bmiNfO, direct comparison of potentials for

oxidation/reduction processes are complicated by the lack of standard reference electrodes used in previous measurements and the different chemical constituencies in each RTIL solution studied.[107,108]

The cyclic voltammetric responses for samples at two and four days are consistent with the two step, single electron reduction of U(VI) to U(V) to U(IV) and possible deposition of UO_2(s). Analysis of the voltammetric waves as a function of scan rate can be used to determine if the oxidation/reduction processes are based on diffusion of solution species or adsorbed surface species. A linear dependence is observed for the each voltammetric wave when the peak current is plotted versus the square root of the scan rate, $v^{1/2}$ (Inset, Figure 5.10).[45] Based on the scan rate data the electrochemical reduction at 0.76 V and -0.10 V and oxidation at 1.21 V observed at two and four days is not consistent with surface bound species. The results suggest that the solution reduction of hexavalent uranium to tetravalent uranium can occur in solution. The electrochemical reactions could then be as follows:

$$UO_2(TFSI)_2 \; + \; e^- \; \rightarrow \; UO_2^+ \; + \; 2TFSI^-$$
$$UO_2^+ \; e^- \; \rightarrow \; UO_2$$
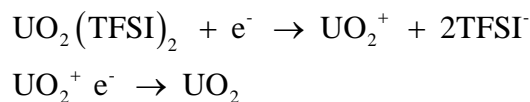
An additional option would be through the formation of a neutral uranium species:

$$UO_2(TFSI)_2 \; + \; e^- \; \rightarrow \; UO_2(TFSI) \; + \; TFSI^-$$
$$UO_2(TFSI) + e^- \; \rightarrow \; UO_2 + \; TFSI^-$$
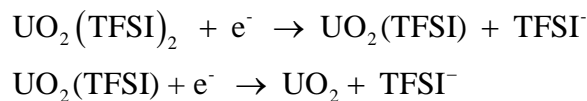
The electrochemical response of $UO_2(TFSI)_2$ in RTIL $[Me_3N^nBu][TFSI]$ after 30 days of argon degassing is more complex, Figure 5.10c. Two additional reduction processes are observed in the in the potential range between -0.6 V and -1.4 V with two oxidation processes overlapping the voltammetric wave previously identified at 1.21 V. The reduction can be attributed to the electrodeposition of uranium species onto the electrode surface. The oxidation is indicative of desorption of the deposits from the electrode surface followed by the normal oxidation of solution species.

To demonstrate the reduction waves are due to the electrodeposition of soluble uranium species, the electrode was poised at a final potential of ~-2 V to ensure that surface deposits remain. The uranium surface deposit was probed using SEM, Figure 5.11.
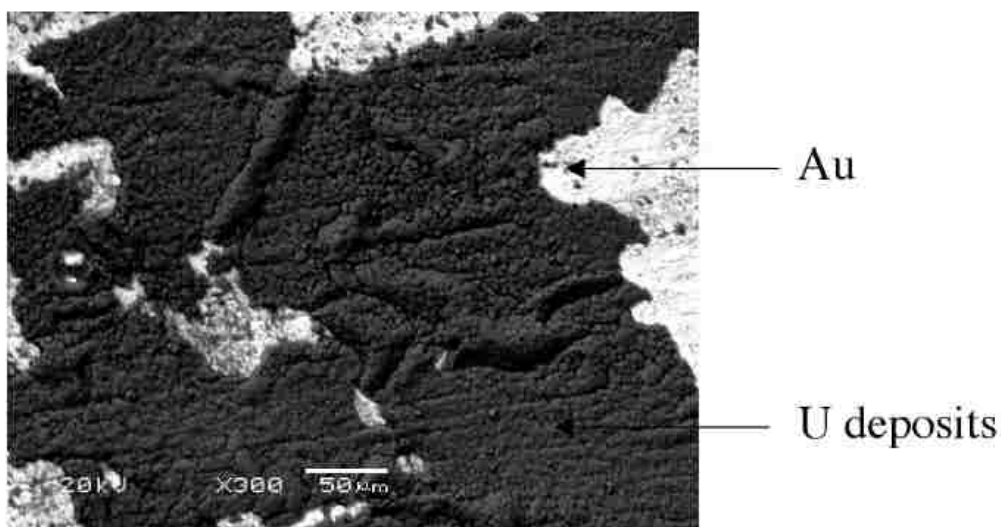
Figure 5.11. SEM of Au substrate with electrochemically deposited uranium

The gold electrode can be observed as the light surface in the SEM image. The multi-step electrochemical deposition suggests that the deposition is not simple and that the TFSI ligand may play a role.

130

The potential dependent deposition of uranium species at a glassy carbon electrode from solutions containing uranium was also evaluated using linear sweep voltammetry, Figure 5.12.
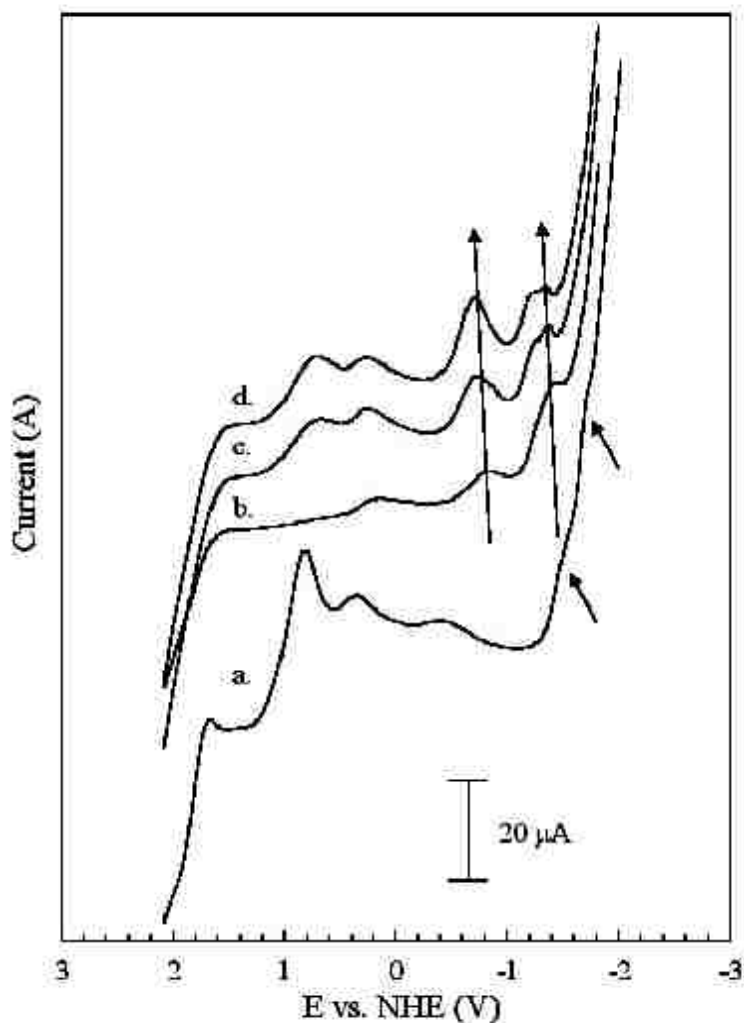
Figure 5.12. Linear sweep voltammetry of successive scans a – d, of soluble UO_2^{2+} in [Me$_3$N^{n}Bu][TFSI] after 40 days under argon. The arrows highlight the electrochemical regions for the deposition of UO_2(s). Scan rate = 100 mV/s.

The figure shows four sequential scans Figure 5.12 a-d, for UO_2CO_3 in RTIL [Me$_3$N^{n}Bu][TFSI] after 30 days The potential range encompasses the regions previously

131

identified for the possible deposition of uranium in the form of UO_2 (s) from [Me$_3$N^{n}Bu][TFSI].[71,107,108] The first LSV scan shows the characteristic voltammetric response observed previously for the sample with the addition of two distinct shoulders at more negative potentials (small black arrows). The observation of the reduction processes is complicated by the reduction of the RTIL cation at more negative potentials. However, the subsequent LSV scan yields lower current responses for the reduction of solution species suggesting some electrode surface passivation occurs after the first scan. The electrochemical reduction of the solution species re-emerge after the second scan indicating that the electrode surface changes with each sequential scan. The voltammetric waves attributed to the deposition of uranium species are observed at ~-0.73 and -1.34 V and are more prominent for each successive scan, Figure 5.12b – 5.12d. The bands also shift to more positive potential (more thermodynamically favorable) with each successive scan showing an increase in current density indicative of an increase in surface deposition.

The deposits on the glassy carbon electrode surface were lightly scraped to remove the material and the sample was then measured using XAFS spectroscopy. The XANES spectra was recorded and compared to solid uranyl nitrate Figure 5.13.
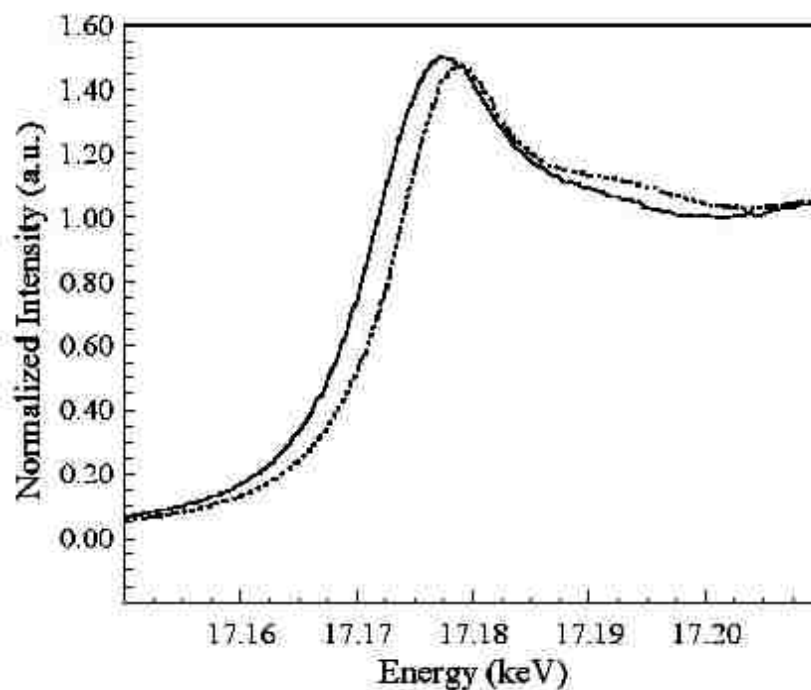
Figure 5.13. XANES spectra for hexavalent U(VI) standard (uranyl nitrate) (dashed line) and uranium deposits (solid line).

The XANES spectra of electrodeposited product exhibit a slightly more intense white line than the U(VI) reference. The position of absorption edge, determined by first derivative method, show to be 1.1 eV lower than the uranyl nitrate standard which indicate that the compound exhibits an oxidation state lower than U(VI). A decrease in the relative intensity at ~17.19 keV was observed for the deposits.

These two observations are consistent with previous reported energies for XAFS measurements of uranium (VI) and uranium (IV), and support the assignment of UO_2(s) for the electrochemical surface deposit.[109] Analysis of the EXAFS spectra of the electrodeposited product, show the presence of: 1.6 oxygen atoms at 1.73(2) Å, 7 oxygen atoms at 2.31(2) Å and 2 U atoms at 4.01(4) Å. The U=O contribution at 1.73(2) Å is

characteristic of U(VI), while the U-O contribution at 2.31(2) Å is likely due to UO_2. The U-U contribution at 4.01(4) Å also indicates the presence of UO_2.

Analysis of the structure for UO_2 from literature, indicate that each uranium atom is surrounded by 8 U atoms with U-O with d =2.37 Å.[110] The U-O bonds change with increasing oxygen coordination. When oxygen coordinated reaches ten oxygen atoms there are four normal U-O bonds (2.37 Å), four U-O bonds with d = 2.22 Å and two additional U-O bonds with d = 2.30 Å.[111-113] The presences of 7 U atoms at 2.31(2) Å suggest that the stoichiometry of the electrochemical deposit is not consistent with pure UO_2(s). Rather, the deposit is consistent with a mixed oxidation state of uranium oxide with increased oxygen character. The presence of U(VI) in the final product and additional oxygen indicate that further oxidation of the deposits after electrodeposition may have occurred in air prior to the XAFS experiment. A final option would be a UO_3 deposit, but the preliminary results as presented above were not consistent with this species either. In summary, the deposits have been confirmed to have a uranium deposition using both XAFS and SEM techniques. The XAFS reflected U(IV) and U(VI) may be present on the electrode surface, and SEM confirmed the presence both uranium and oxygen. However, the data obtained was not consistent with one singular oxidation state of uranium.

5.4 Conclusions

The present work has evaluated the direct dissolution of UO_2CO_3(s) in RTIL [Me_3N^nBu][TFSI]. The data indicate that the direct dissolution can be initiated with degassing of the solution under argon atmosphere. However, the process is slow and the

solubility is limited due to the poor displacement of CO_3^{2-} by the TFSI anion. The direct dissolution and solubility of $UO_2CO_3(s)$ is increased with the addition of HTFSI. The UV/Visible and IR spectroscopy suggest that free UO_2^{2+} can complex with the TFSI ligand in the RTIL solution. The solubility of UO_2^{2+} was probed electrochemically and multiple reduction processes and a single oxidative process emerge at short time in the absence of acid. These electrochemical processes were attributed to diffusion related processes rather than surface adsorption of uranium species. The potential dependent deposition of uranium species from RTIL was also demonstrated. The electrochemical deposition of uranium was achieved in RTIL with and without the addition of HTFSI and the surface deposit was confirmed using SEM analysis. XANES indicate that the oxidation state of the electrochemically deposited species are consistent with known uranium oxidation states. These studies indicate that the direct dissolution of nuclear materials may possible through the acidification of RTIL. Furthermore the potential mediated separation of lanthanides and actinides using electrochemical methods may be possible using the same solution utilized for the direct dissolution of the species.

Chapter 6: Preliminary U(III) Results, Conclusions and Recommendations

6.1 Preliminary U(III) Results

Initial experimentation was successfully performed during the final stages of this Dissertation on two U(III) species: $U(TFSI)_3$ and $UI_3(THF)_4$. However, do to limitations with available equipment and reference literature, the research was left in the preliminary stages. The following sections present the initial observations from these experiments.

6.1.1 Introduction

Uranium metal is of great importance for use nuclear fuel, medicinal targets, and in military armor and munitions.[114,2,115] Medicinally, uranium can be used as a target from producing Mo-99.[114] Uranium metal alloys can be used for nuclear fast reactor fuel. An example is binary alloy consisting of 38% uranium and 62% zirconium combined with 1% niobium cladding.[116] The zirconium increases the fuel's melting point, so the Zr-U fuel rods could operate under lower temperature conditions than that of UO_2 fuel.[116] Additionally, there are military applications to utilizing ammunition containing depleted uranium.[115] In this case, the addition of the uranium to the weapons affords the projectiles the ability to pierce through heavy armor.[115]

Uranium metal can be recovered from spent nuclear fuel or chemically generated produced following known reactions. Typically, a liquid molten salt system is used for

the reclamation of the uranium metal by first dissolving the fission products from the reactor cycle, then electrochemically depositing the uranium onto the surface of the cathode.[117,118] Another method for obtaining uranium metal is by utilizing magnesium or calcium to reduce UF_4 or UCl_4 at reaction temperatures above 1300 °C.[119] This route entails specially fabricated reaction vessels to sustain the stress from such high temperatures, which, in turn would lead to increased cost.[120] This scheme also involves the use or production of highly toxic hydrofluoric gas during the synthesis of the UF_4 materials. This is an additional expense as specific safety precautions must be taken to handle HF gas.[120]

Due to the complications listed above, one possible improvement in processes used to obtaining uranium metal would be the elimination of elevated temperatures and the toxic offgas.. Room temperature ionic liquids (RTIL) systems can be utilized in the process to provide similar chemical and electrochemical properties associated with molten salt systems to achieve U metal deposition or recovery from oxidized forms without the need of high temperatures.

As described in Section 1.1, RTILs are purely ionic solvents that are typically free of water and they provide a unique opportunity to examine f-elements electrochemically without appreciable hydrolysis. A water free solution is especially important in obtaining uranium metal from the electrodeposition from solution. Previous experiments outlined in this dissertation indicate that reactions of uranium species in aqueous solutions produce the oxide rather than the targeted oxygen free U(III) complex. Thus, because water hydrolysis dominates the process in the aqueous solutions examined water free solvents were used in the research presented in this Chapter. Additionally, RTILs have shown

promise in the area of radiation damage resistance.[121] This attribute would likely be necessary to utilize them as solvents for separations of radionuclides, as radiation damage could reduce extraction efficiency by impacting or degrading the chemical species within the solvent.

To electrochemically deposit uranium metal from a molten salt eutectic system, oxygen free U(III) or U(IV) complexes are often utilized.[96,122,123] By applying a sufficiently negative potential, U(III) can be reduced to U(0), yielding a uranium metal deposit on the surface of the cathode. To examine a lower temperature deposition process $U(TFSI)_3$ was synthesized from $UI_3(THF)_4$ and the potential mediated deposition of uranium metal was examined in RTIL .

The reduction and oxidation states of $U(TFSI)_3$ and $UI_3(THF)_4$ were evaluated electrochemically using cyclic voltammetry. For each species, an electrochemically deposited uranium metal sample was obtained. The deposits were analyzed using scanning electron microscopy (SEM), energy dispersive spectroscopy (EDS), and powder x-ray diffraction (XRD).

6.1.2 Methods

6.1.2.1 Reagents

The synthesis of the $UI_3(THF)_4$ and the $U(TFSI)_3$ solids were described in Section 3.4. The RTIL solvent, $[Me_3N^nBu][TFSI]$, was purchased from Solvionic (France). Tetrahydrofuran (THF) was purchased from Sigma Aldrich (reagent grade). All

purchased reagents were purged with argon gas prior to use to remove any excess oxygen content.

6.1.2.2 Experimental Design

All electrochemical experiments were performed inside of an argon filled glove box. Initially, these trials were performed inside of a Labconco glove box, and later they were moved to a MBRAUN glovebox (see Section 2.8). At any point in which the air-sensitive samples needed to be removed from the argon filled glove box, they were sealed into screw-top containers that were then taped closed with masking tape. These containers were then placed into a second screw-top container that was also taped closed with masking tape. After sufficiently sealing them from the air, the samples were moved quickly to the final location. For example, this protocol was followed when transferring the materials from the Labconco glove box to the MBRAUN glove box. This was done so as to protect the samples for oxidizing in the open atmosphere.

6.1.3 Results and Discussion

6.1.3.1 Electrochemistry of U(TFSI)$_3$ and UI$_3$(THF)$_4$

U(TFSI)$_3$ was added to an RTIL solution to produce concentration of approximately 5 mM. For comparison, an RTIL solution containing 5mM of UI$_3$(THF)$_4$ was also examined in parallel. For both solutions, the solids were added to RTIL and stirred for 10 minutes until the solids had dissolved (based on visual inspection). Both

U(III) solutions were then examined using cyclic voltammetry to evaluate oxidation/reduction processes associated with the U(III) species in the RTIL solution (Figure 6.1). The resulting electrochemical oxidation and reduction reactions of the two U(III) species is discussed simultaneously.

There are two reductive waves and two oxidation waves that can be observed in the cyclic voltammetry for both species in RTIL. Additional voltammetric waves are observed for $UI_3(THF)_4$, when compared to $U(TFSI)_3$. Table 6.1 summarizes the observed oxidation and reduction processes for the 10th cycle.
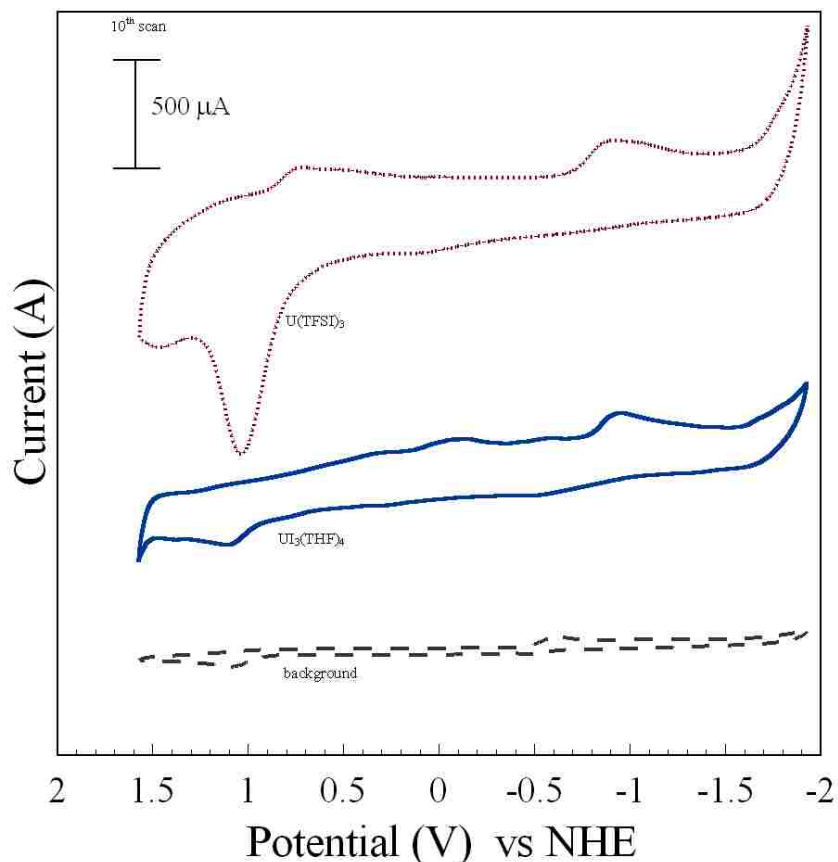
Figure 6.1. CV results at 100 mV/s from the 10th cycle for both of the U(III) species in the RTIL. The grey dashed line is the RTIL background, the solid blue line is 5mM $UI_3(THF)_4$, and the red dotted line is the 5mM $U(TFSI)_3$.

Table 6.1. Oxidation and reduction processes in each U(III) system at the end of the 10th cycle.

Species	Reduction Process: Potential (V) versus NHE			
$UI_3(THF)_4$		-0.095	-0.6092	-0.934
$U(TFSI)_3$	0.7252			-0.934
	Oxidation Process: Potential (V) versus NHE			
$UI_3(THF)_4$	-0.513	1.098		
$U(TFSI)_3$		1.049	1.466	

It can be seen from the comparison in Table 6.1 that the processes at -0.9 V versus NHE and +1.0 versus NHE occur at the same potential for both species. Therefore, a preliminary conclusion can be drawn that these two bands are both caused from reduction and oxidation, respectively, of the uranium species in solution. One option is that the $U(TFSI)_3$ species is deposited onto the surface of the electrode by first removing one or two of the TFSI ligands in a stepwise manner similar to the mechanism presented as a possibility for the Sm-TFSI complex (Section 4.3.3). The responses observed at -0.9 V would then represent deposition of uranium metal on the electrode surface. A schematic of this theoretical process is presented below in Scheme 6.1.
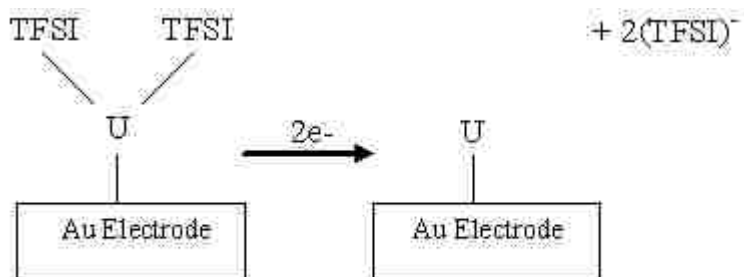
Scheme 6.1. Possible uranium deposition steps occurring during potential mediated deposition from U(TFSI)$_3$ in RTIL.

The additional electrochemical processes that are observed for UI$_3$(THF)$_4$ can be at least partially attributed to free iodine as a result of the reduction process observed in the following mechanism:

$$UI_3 + 3e^- \rightarrow U(0) + 3I^-$$
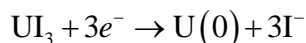
After the I$^-$ is free from the uranium complex, it can undergo further reactions on its own or re adsorb on the deposited uranium. In addition, the I- can react with the gold surface that does not contain uranium deposits.[124] The adsorption of I$^-$, as well as I$_3^-$ on gold electrode surfaces is well known, and potential interactions will be discussed further in this section.[125] The two possibilities for the iodide interactions and adsorption on the electrode further complicate the analysis of the UI$_3$(THF)$_4$ system.

Analysis of the reductive and oxidative processes in the U(TFSI)$_3$ system is also not trivial due to the potential interactions of the TFSI ligand.[126] The best possible option would be to analyze both U(III) systems with a Quartz Crystal Microbalance (QCM) to obtain a more comprehensive analysis of the voltammetry, but due to the radioactive

nature of the uranium species, this analysis method was not available. In the absence of

the QCM results, only the initial data will be discussed here. Given the preliminary nature

of the results, no formal conclusions can be made with certainty.

The voltammetry multiple cycles of U(TFSI)$_3$ in the RTIL solution is presented in

Figure 6.2. This information can be used to gain an understanding of what is changing

over time in the RTIL system.
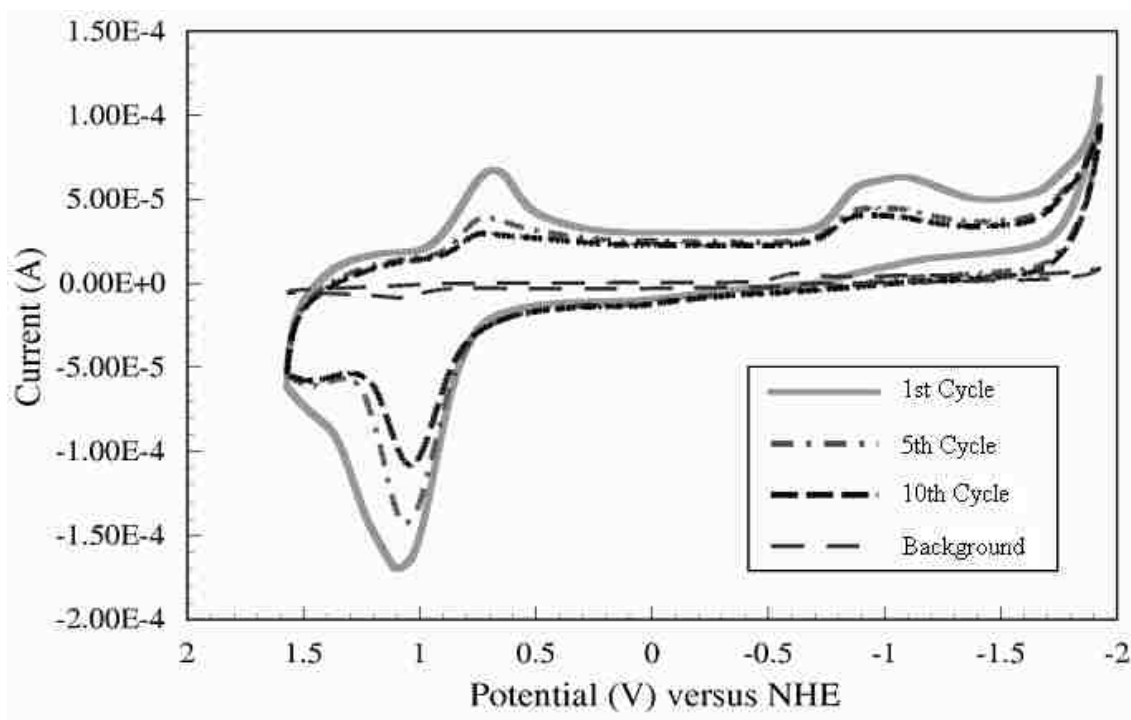
Figure 6.2. Cyclic voltammetry at 100 mV/s of 5mM U(TFSI)3 in RTIL. The solid light grey line is the 1st cycle, the dotted dashed medium grey line is the 5th cycle, and the black short dashed line is the 10th cycle. The grey long dashed lines represent the RTIL background.

It can be seen in Figure 6.2 that all of the redox reactions observed from U(TFSI)$_3$ in RTIL are diminishing with each subsequent cycle. When electrodeposition is occurring during CV, a decrease may be observed in one or more bands.[9] Changes in the magnitude of cyclic voltammetry bands can be observed as a result of a reduction in the surface area of the gold electrode.[9] Further examination of the voltammetry can give insight into whether the potential mediated deposition is favored at the original electrode, or on an electrode that already contains the material to be deposited.[44] In addition, it was observed that the decreasing current response continued through all cycles examined. Future work should include analysis of more cycles to determine if/when steady state in the electrochemical responses occurs.
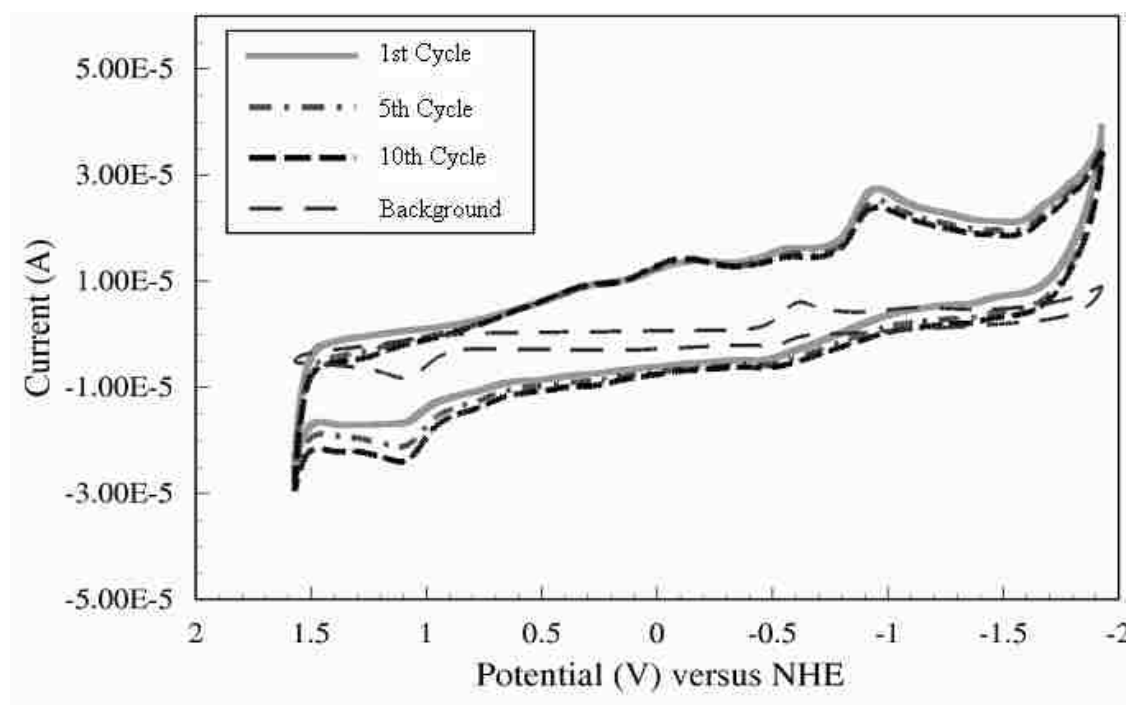
Figure 6.3. Cyclic Voltammetry at 100 mV/s of 5mM UI$_3$(THF)$_4$ in RTIL. The solid light grey line is the 1st cycle, the dotted dashed medium grey line is the 5th cycle, and the black short dashed line is the 10th cycle. The grey long dashed lines is the RTIL background.

It can be seen in Figure 6.3 that the reduction reactions at -0.61 and -0.93 V for UI$_3$(THF)$_4$ in the RTIL observed are decreasing with each successive cycle. However, the oxidation reaction at 1.0 V appears to be increasing with continued cycles. These observations were consistent through all cycles examined. Furthermore, the differences in the voltammetry as a result of additional bands from oxidation and reduction of I$^-$ can be readily observed. The decreases in the current are consistent with reductive adsorption of I$^-$ at the electrode surface.[125,127,128] Another observation from comparing Figures 6.2 and 6.3 is that the current response in the U(TFSI)$_3$ system decreases more rapidly than in the UI$_3$(THF)$_4$ experiments. As discussed previously in this Chapter, a reduction in current indicates a decrease in surface area on the gold electrode;[45,44] this could be the result of increased quantities of uranium deposited from U(TFSI)$_3$ in RTIL when compared to UI$_3$(THF)$_4$ in RTIL or a change in thermodynamics associated with the subsequent reduction of U(TFSI)$_3$ at a uranium surface when compared to a clean gold surface. The current density, which is found by dividing the current by the surface area on the electrode, has a strong influence on the deposition rate as well as the quality of the deposit.[129] In electrodeposition, each system has an optimal current density that should be used to obtain the highest deposition efficiency.[129] This optimal current density was not determined for the work presented in this Chapter, but should be found in future work to assist with larger quantity deposits of uranium metal. As stated for the above U(TFSI)$_3$ discussion around Figure 6.2, future work should also include more cycles to determine if/when steady state in the electrochemical response would be reached, as well as to

145

identify and confirm the specific reactions occurring at each oxidation and reduction wave.

6.1.3.2 Deposition of uranium metal

It was observed that the uranium metal deposition with the TFSI removed appeared to be occurring at -0.9 V versus NHE. The electrochemical deposition of uranium metal onto the surface of the gold sheet electrode was explored utilizing controlled potential deposition. The voltage was held constant at -1.5 V versus NHE. A more negative potential was selected to be sufficiently electronegative to drive the bulk deposition of U(0) free of the TFSI anion complexation.[45] Electrochemical deposition utilizing an over potential was described in Section 2.8. Any additional potential beyond the minimum calculated deposition potential is considered the over potential.[45] More specifically, the over potential (η) is the difference between the equilibrium potential (E) and the potential as the current is flowing (E(I)):

$$\eta = E(I) - E \hspace{4cm} \text{Equation 6.1}$$

In potential mediated electrochemical depositions, an over potential is typically utilized to achieve improved deposition results.[96] In addition, the over potential term can also be related to increased nucleation rate.[130] This technique was used in the work performed in this Dissertation in order to obtain a large enough deposit to analyze via further techniques. Using the cyclic common waves at -1.0 V from the voltammetry results presented in Figures 6.1-6.3, a potential for electrodeposition was selected. The same

potential was selected for both U(III) species given the data reflected U(0) deposition occurred in the same region from both U(TFSI)$_3$ and UI$_3$(THF)$_4$ in the RTIL.

6.1.3.3 Analysis of electrodeposited uranium metal

Following electro-deposition from both systems, the electrodes were sealed into an argon filled container (see Section 6.2.1) and removed from the glove box for analysis via SEM and EDS. Once at the instrument, they were immediately placed into the chamber, which maintains a constant vacuum. Images were obtained of the surface of both electrodes. Grainy uranium deposits could be seen consistently on the electrode surfaces, whereas the gold electrode surface lies in the flat, light colored regions (Figures 6.4 and 6.5).
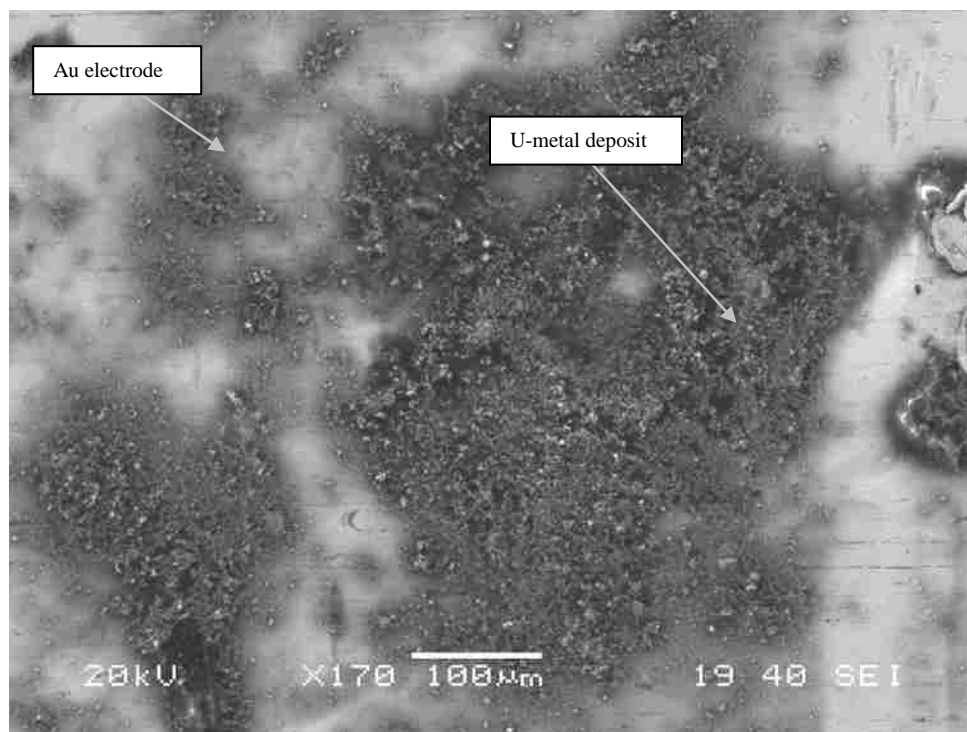
Figure 6.4. SEM images of uranium metal deposited on a gold electrode deposited from UI$_3$(THF)$_4$ in RTIL.
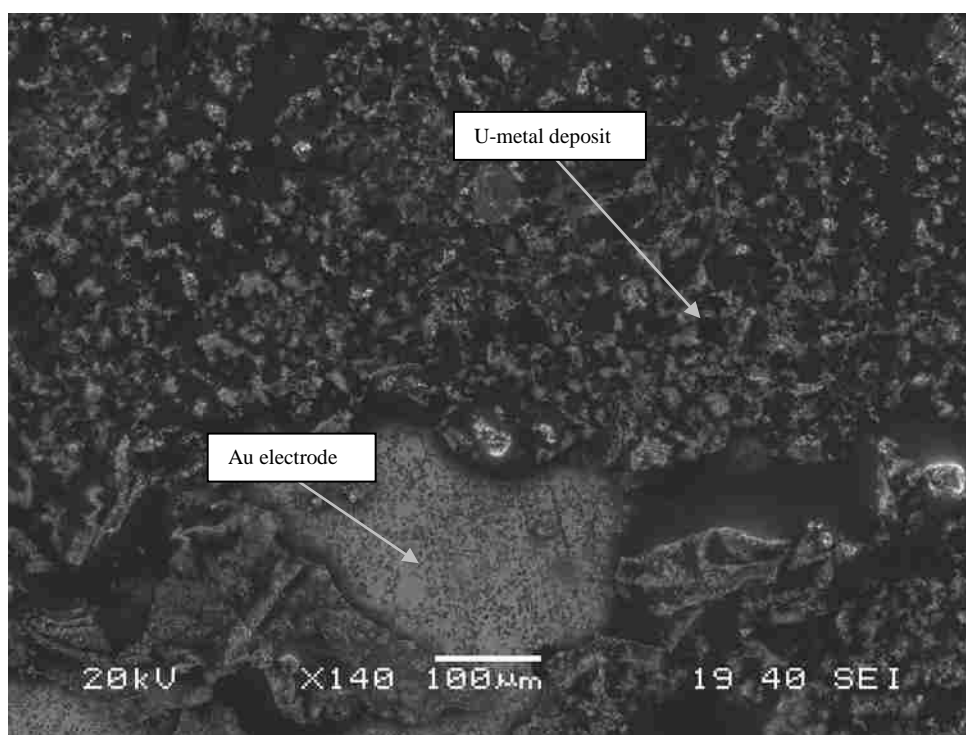
Figure 6.5. SEM images of uranium metal deposited on a gold electrode from U(TFSI)$_3$ in RTIL.

The deposit obtained from the $UI_3(THF)_4$ system can be seen in Figure 6.4, and the deposit from the $U(TFSI)_3$ system is in Figure 6.5. Not surprisingly, the surface morphology was very similar for both electrodes. Once the images were obtained, EDS analysis was executed. A series of eleven spots were evaluated on each electrode for elemental composition. A representative spectrum along with the corresponding SEM image can be seen in Figure 6.6.
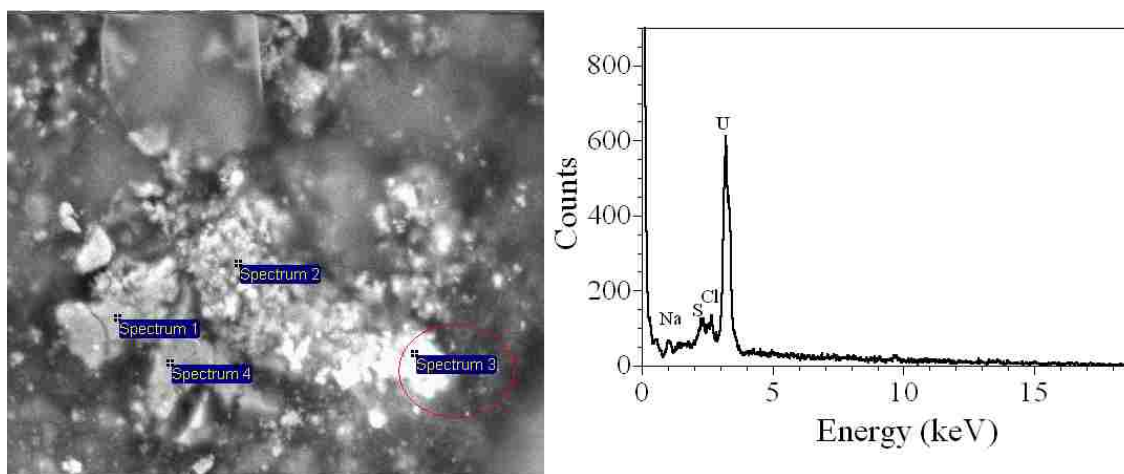
Figure 6.6. Left: SEM image of a gold electrode with uranium deposits. The image depicts several spots analyzed with EDS. The corresponding EDS data for Spectrum 3, red circled, is shown on the right.

In every case, uranium was found with no accompanying oxygen at 5.5 keV. Given the EDS is able to detect oxygen content down to 0.5 weight percent,[93] this is strong support of uranium metal deposition.[93] Additionally, EDS analysis can be utilized to identify other elements that are contained in the TFSI species including fluorine, oxygen, nitrogen, and sulfur consistent with some residual ligand on the surface. Elements lighter than carbon cannot be seen in the EDS.[94] The RTIL species, $[Me_3N^nBu][TFSI]$ contains carbon, hydrogen, nitrogen, sulfur, oxygen, and fluorine.

Evidence of the RTIL components were visible in the EDS results with the appearance of the sulfur band at 2.47 keV. In addition, chlorine and sodium were also observed in the spectrum, which could have been introduced as potential contaminants or un-reacted materials from the RTIL synthetic process.

In order to further understand the nature of the uranium metal deposit, the samples were examined using powder XRD. Preliminary XRD results indicated that alpha phase uranium metal may be deposited on the surface of the electrode; however the amorphous nature of the deposit proved to make using this technique complicated. In order to improve the response, additional deposits were obtained from a pure solution, and then an attempt to re-crystallize the uranium metal was made.

The electrode was placed into an argon filled glass tube while still in the inert atmosphere glove box. The glass tube was then sealed with parafilm followed by tape, then inserted into a secondary sealed container. Next, the tube was removed from the glove box and subsequently attached to a Schlenk line. It was then sealed by using a torch while maintaining an air free atmosphere from the vacuum on the Schlenk line (Figure 6.7).

Figure 6.7. Glass tubes containing the U(0) deposited Au electrodes after sealing closed.

The glass tube was then placed into a tube furnace and heated to 550 ºC for 5 hours. The temperature was selected using the phase diagram for uranium, such that alpha uranium would remain stable. According to the diagram, the temperature would then be under 660 ºC.[119] Glass tubes were preferred because they could be more rapidly sealed then quartz, and thus further prevent air from entering the system. However, these glass tubes have a softening point of approximately 600 ºC, so the temperature was kept at 550 ºC such as to provide the optimum conditions for the glass to remain sealed and for the formation of alpha uranium crystalline properties. After cooling, the glass tube was

returned to the argon filled glove box, opened, and cut into two pieces. One piece was

packed in an air tight sample holder for a second attempt at XRD analysis (Figure 6.8).
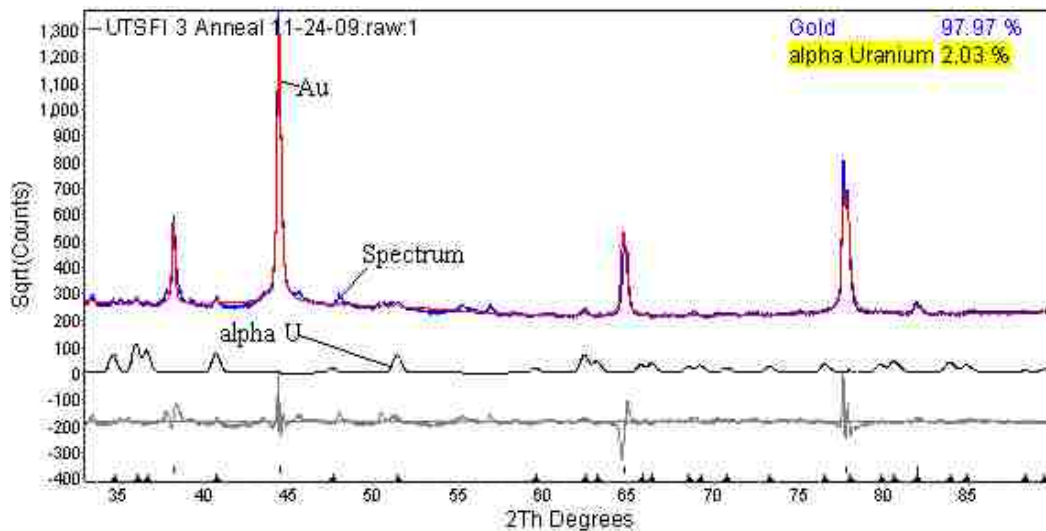
Figure 6.8. XRD pattern with alpha uranium metal analysis

The efforts to re-crystallize the uranium proved somewhat successful. Bruker

TOPAS software was used during data analysis. The TOPAS software was designed for

structural determination using powder XRD results.[131] From these results, 2 % by weight

alpha uranium metal was determined to be on the surface of the electrode in the examined

sample. The vertical lines in the figure indicate the areas in the resulting XRD spectrum

that corresponded to the expected alpha uranium result. The second electrode piece was

analyzed using SEM and EDS (Figure 6.9 and 6.10). The uranium deposits can be seen

in the white grainy sections attached on the surface of the gold electrode.
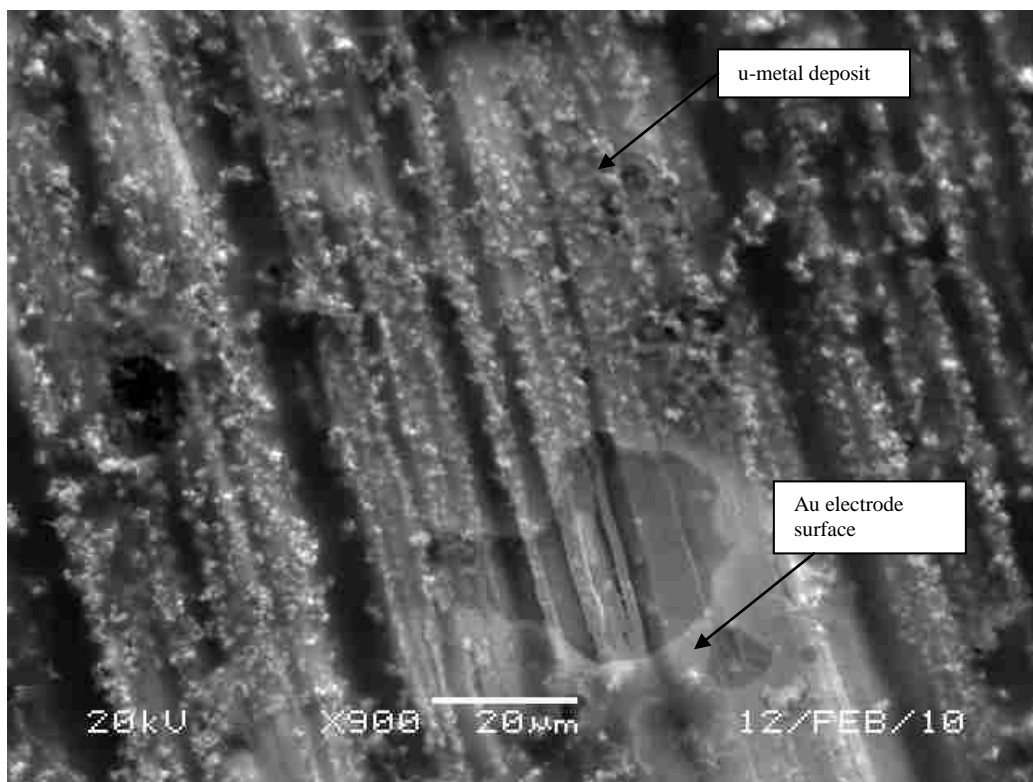
Figure 6.9. SEM image of annealed uranium on the gold electrode starting from U(TFSI)$_3$ in RTIL.
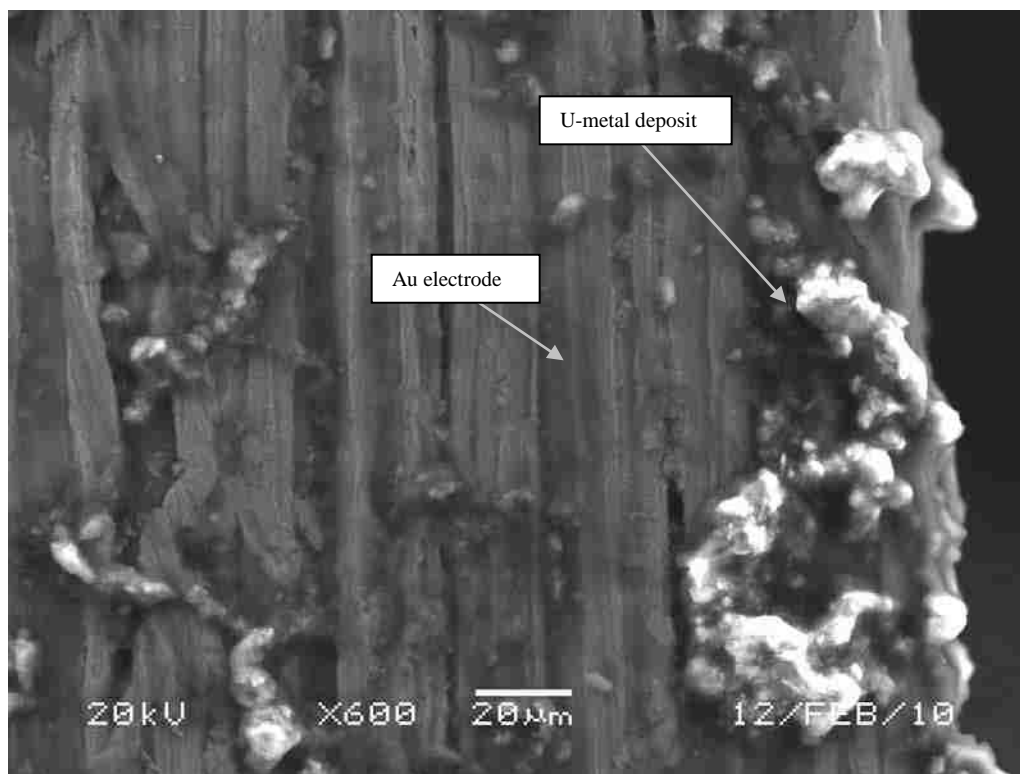
Figure 6.10. SEM image of annealed uranium on the gold electrode starting from $UI_3(THF)_4$ in RTIL.

The corresponding EDS was also obtained for ten spots on the electrode surface.

A representative spectrum is shown below in Figure 6.11.
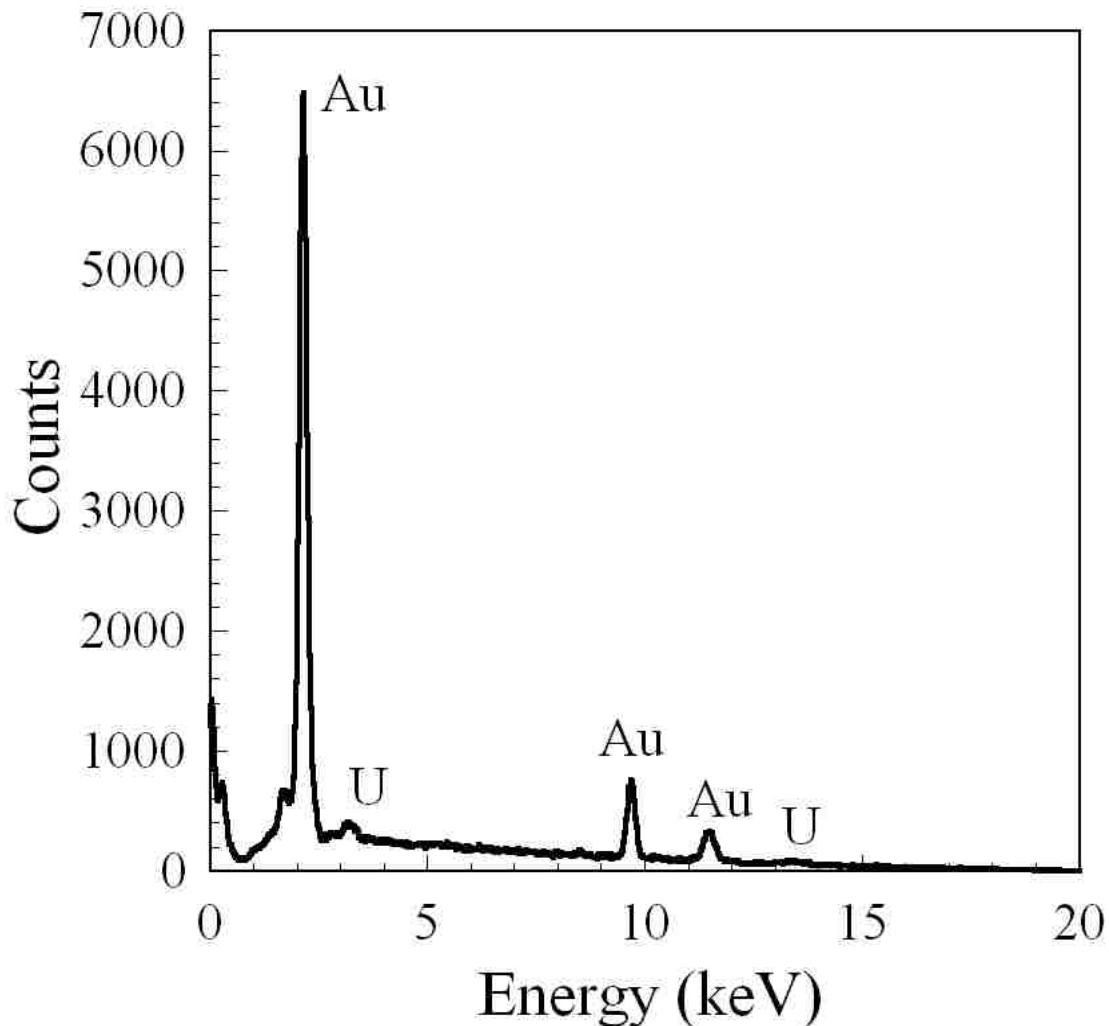
Figure 6.11.   SEM EDS representative spectrum of an annealed gold electrode after uranium deposition from U(TFSI)$_3$ in RTIL.

Once again, uranium was found with no accompanying oxygen at 5.5 keV or previously observed contaminants/traces of the TFSI anion (shown in Figure 6.6). These results indicate that a successful deposit of U(0) can be obtained from the RTIL solution. This evidence is strengthened by the number of spots analyzed on the electrode surface, as a representative sampling of the entire surface of the electrode was evaluated in this process.

6.1.3.4 Summary:

In these studies, two U(III) complexes, $U(TFSI)_3$ and $UI_3(THF)_4$, were analyzed using cyclic voltammetry. Using this technique, deposition of U(0) was observed at -0.93 V versus NHE for the $U(TFSI)_3$ species and the $UI_3(THF)_4$ complex. In the case of the $U(TFSI)_3$ species, it is presented here that it initially deposits as a U-TFSI species on the surface of the electrode at +0.72 V, and as the current is continued to more negative directions, the remaining ligand is displaced, leaving the free metal on the surface by -0.93 V versus NHE (Figure 6.2). For the $UI_3(THF)_4$, it is presented that the U(0) deposit is obtained in a single 3 electron reduction process at -0.93 V (Figure 6.3). It is interesting to note that the deposition of U(0) is achieved in a more electropositive region from both the $U(TFSI)_3$ as well as the $UI_3(THF)_4$ in RTIL solutions when compared to LiCl-KCl eutectic melts.[22,23] Given the nature of the known interaction of the RTIL solvent with the metal ligands, it is likely responsible for these shifts.[12] This is because the TFSI anion has been documented to have stabilizing affects as a result of coordination with the metal ligand. These stabilizing affects have been observed in multiple studies in the form of more electro-positive reduction peaks, just as the case was observed in this work.[47,28] Using SEM and the accompanying EDS as well as XRD, alpha uranium metal was found to be present on the gold electrode surface. These studies have shown that it is possible to directly dissolve a U(III) complex and to achieve potential mediated reduction to uranium metal separated from the solution and deposited onto the electrode surface.

6.2 Dissertation Conclusions

This research has explored several methods for introducing various f-species into the RTIL solvent, [Me$_3$N^{n}Bu][TFSI]. The RTIL solution was analyzed carefully, tailoring the anion and the cation in such a way that optimal electrochemical conductivity and f-species solubility could be explored with a low melting point, conductive ionic solvent. The melting point of the amine based cation was depressed to allow room-temperature electrochemistry to be executed with a wide electrochemical window afforded by combining the Me$_3$N^{n}Bu cation with the TFSI anion.

Methods of introducing the f-species while still exploiting the exceptional utility of the RTIL solvent were explored. Sm(TFSI)$_3$ was synthesized in aqueous solution for these purposes, and the extraction capabilities of the RTIL were examined. It was found that by reducing the acidity of the aqueous phase to above pH 9.0, high extraction efficiency could be obtained, with 100 % of the samarium entering into the RTIL phase. Although other samarium complexes could be extracted under the same conditions, the efficiency of the extraction was diminished relative to beginning with Sm(TFSI)$_3$; indicating that, during the research performed for this dissertation, the TFSI anion complex affords greater solubility in the RTIL solvent.

The electrodeposition of Sm(0) metal was demonstrated at a potential of -1.5 V versus NHE; which is between 0.3 and 1.0 V more electropositive than previous published results in RTIL and aqueous media. Results from QCM experiments combined with CV analysis indicated that this deposition likely occurred in a stepwise manner, in which an initial Sm-TFSI complex was deposited onto the surface of the gold electrode. The TFSI was later removed from the surface as the potential was varied to more

negative values. This indicates that the TFSI ligand provides more favorable electrochemical thermodynamics for the potential mediated electrodeposition. Samarium deposits were analyzed using SEM and EDS; and the results further supported that samarium metal was deposited on the electrode surface, with no accompanying traces of oxygen or TFSI ligand, thus confirming the potential mediated samarium metal deposition from RTIL solution.

The research presented in this dissertation reflected the multifunctional aspects of the RTIL solvent, in that the initial samarium complex could be extracted from an aqueous solution into the RTIL. The same RTIL solvent was then used to remove the samarium from the RTIL solution by electrodeposition onto the surface of a gold electrode.

Additional investigations into methods of introducing a f-element species into the RTIL solvent were conducted by argon assisted dissolution of uranyl carbonate. This mechanism was made possible by H^+ introduced into the solvent from trace amounts of water in the ionic liquid, which aided in the displacement of carbonate and subsequent dissolution of UO_2^{2+} into the RTIL. In replicate studies, it was found that by adding HTFSI acid to the initial RTIL solution, the reaction mechanism was greatly improved in terms of both in maximum solubility and in reaction rate for completion. By adding HTFSI acid, other species not examined in this Dissertation may be made soluble into the RTIL that otherwise would not have been. This solubility is afforded by the acid/base reaction in which the super acid, HTFSI is potentially able to react with the insoluble complex to form a RTIL soluble species.[132,133] The same RTIL solvent could then be utilized to remove the f-species of interest by electrodeposition onto the electrode.

Following introduction of uranyl into the RTIL, a potential mediated electrodeposition of UO_2(s) was obtained on the electrode surface. The electrode surface was then imaged with SEM. In addition, EDS analysis confirmed the presence of uranium and oxygen on the deposit. Finally, XANES analysis confirmed that the uranyl deposit was primarily in the 4+ oxidation state, with some quantity on uranyl on the electrode's surface having oxidized to the 6+ oxidation state.

Finally, preliminary data was presented earlier in this Chapter for the direct dissolution of two U(III) species, $U(TFSI)_3$ and $UI_3(THF)_4$ into the RTIL. In both cases, U(0) deposits were achieved at the electrode surface when electrochemical analysis was performed. The uranium deposits were verified using SEM EDS and powder XRD techniques.

In summary, these studies have shown three different methods of introduction of several different f-species into the RTIL solvent, $[Me_3N^nBu][TFSI]$:

1. Extraction

2. Argon assisted dissolution with acidification

3. Direct dissolution both with and without TFSI complexation

All of these methods reflected various needs in industry, as well as the capabilities of the RTIL as a solvent. In all cases, the RTIL was used for multiple purposes, with the final result being a successful retrieval of the f-species from the RTIL and onto the electrode surface utilizing electrodeposition techniques. Finally, in the case of both samarium and uranium, metal deposition was obtained under room temperature conditions, reflecting the utility of the wide electrochemical window afforded by the RTIL solvent.

6.3 Recommendations

This research presented in this Dissertation exploited the extraction utility of the RTIL solvent, and indicated that the aqueous layer pH has a direct affect on the success of the extraction. It is reported in this work that the shared complex of Metal-TFSI anion increased the extraction efficiency, but additional RTIL anion/cation combinations should be examined to understand the extent to which this applies. In addition, comparisons of the affects of oxidation state by studying the same anion f-element metal complex in different oxidation states would further aid in understanding to what degree oxidation state plays a role in the extraction efficiency. For example, an extraction in which the efficiencies of $Sm(TFSI)_3$ and $Sm(TFSI)_2$ are compared would be of great use in comparing oxidation state effects on extraction efficiency without having to account for variations in the ligands to which the metals are complexed to.

In the extraction results presented in this dissertation, the acidity of the aqueous phase was reduced, which increased the crossover of the samarium species into the RTIL phase. Further studies should be performed in which the acidity of the RTIL is increased, while the acidity of the aqueous phase is unchanged. Water free organic acids should be used for this type of study.

In this Dissertation, the efficiency of the extraction process was examined, but not the reaction kinetics. Further exploration into the kinetics would prove informative. This study should include multiple ligands and oxidation states with respect to the species being extracted. The results would provide insight into whether the most efficient species extracted was also the most rapid process.

The acidity of the RTIL layer is also of interest. As of this date, no publications exist to provide a method to determine the acidity of the RTIL. Future work should include a comprehensive analysis of adding water free acid to the RTIL and evaluating the outcome both spectroscopically as well as using other methods, such as revisiting the litmus paper results.

Additional research related to the UO_2CO_3 ligand displacement process should also be performed.   Additional carbonate species could be evaluated for solubility after adding HTFSI to examine if the same ligand displacement process occurs. A complete study of how to optimize the conditions to increase the solubility by addition of HTFSI acid would be extremely beneficial. This is notable considering the fact that many researchers have reported difficulties with ligand solubility in RTIL solutions.

As mentioned previously in this Chapter, further studies on the U(TFSI)₃ and UI₃(THF)₄ systems need to be performed in order to better understand the electrochemical reactions occurring in the system when performing cyclic voltammetry or electrodeposition. A QCM would be ideal for answering lingering mechanism questions.

Finally, and perhaps most of interest to industry would be exploration of the deposition of uranium and other f- element metals followed by volatilization of the electrode to leave only pure f-metal behind. To efficiently accomplish this, different electrodes with lower melting points than that of gold would need to be explored, as well as the quantity of deposited materials increased. One electrode that should be considered is zinc. A literature search revealed that it has been successfully utilized as a working electrode,[134] and the melting point of the electrode is 420 ℃.[135] This is over 200 ℃

lower than that of alpha uranium metal, and therefore may afford isolation of the uranium.[119]

References

(1)   Guor-Tzo Wei; Chao-Jung Chen; Zusing Yang *Analytica Chimica Acta* **2003**, *488*, 183-192.

(2)   Maury, O. Ephritikhine, M. Nierlich, M. Lance, M.; Samuel, E. *Inorganica Chimica Acta* **1998**, *279*, 210-216.

(3)   Nockemann, P. Servaes, K. Van Duen, R. Van Hecke, K.; Van Meervelt, L. *Inorganic Chemistry* **2007**, *46*, 11335-11344.

(4)   Mekki, S. Wai, C. M. Billard, I. Moutiers, G. Burt, J. Yoon, B. Wang, J. Gaillard, C. Ouadi, A.; Hesemann, P. *Chem. Eur., J.* **2006**, *12*, 1760-1766.

(5)   Nockemann, P. Thijs, B. Pittois, S. Thoen, J. Glorieux, C. Van Hecke, K. Van Meervelt, L. Kirchner, B.; Binnemans, K. *J. Phys. Chem. B* **2006**, 20978-20992.

(6)   Nockemann, P. Thijs, B. Parac-Vogt, T. N. Van Hecke, K. Van Meervelt, L. Tinant, B. Hartenbach, I. Schleid, T. Ngan, V. T. Nguyen, M. T.; Binnemans, K. *Inorg. Chem.* **2008**, *47*, 9987-9999.

(7)   Billard, I. Gaillard, C.; Hennig, C. *Dalton Trans.* **2007**, 4214-4221.

(8)   Rao, C. H. Venkatesan, K. A. Nagarajan, K.; Srinivasan, T. G. *Radiochim. Acta* **2008**, *96*, 403-409.

(9)   Evans, R. G. Klymenko, O. V. Price, P. D. Davies, S. G. Hardacre, C.; Compton, R. G. *ChemPhysChem* **2005**, *6*, 526-533.

(10)   Buzzeo, M. C. Evans, R. G.; Compton, R. G. *ChemPhysChem* **2004**, *5*, 1106-1120.

(11)   Seddon, K. R. Stark, A.; Torres, M. J. *Pure Appl. Chem* **2000**, *72*, 2275-2287.

(12)   Warren J. Oldham, J. Costa, D. A.; Smith, W. H. *Development of Room Temperature Ionic Liquids for Applications in Actinide Chemistry*; Los Alamos National Laboratory: Division, Nuclear Materials Technology, 2001; p. 10.

(13)   Cocalia, V. A. Gutowski, K. E.; Rogers, R. D. *Coordination Chemistry Reviews* **2006**, *250*, 755-764.

(14)   Dietz, M. L. *Sep. Sci Technol.* **2006**, *41*, 2047-2063.

(15)   Luo, H. Dai, S. Bonnesen, P. V. Haverlock, T. J. Moyer, B. A.; Buchanan III, A. C. *Solvent Extraction and Ion Exchange* **2006**, *24*, 19-31.

(16)   Nikitenko, S. I. Cannes, C. Naour, C. L. Moisy, P.; Trubert, D. *Inorganic Chemistry* **2005**, *44*, 9497-9505.

(17)   Chaumont, A.; Wipff, G. *Inorganic Chemistry* **2004**, *43*, 5891-5901.

(18)   May, I. Taylor, R. J. Denniss, I. S.; Wallwork, A. L. *Czechoslovak Journal of Physics* **1999**, *49*, 597-601.

(19)   May, I. Taylor, R. J. Denniss, I. S.; Wallwork, A. L. *Czechoslovak Journal of Physics* **1999**, *49*, 597-601.

(20)   Giridhar, P. Venkatesan, K. A. Srinivasan, T. G.; Vasudeva Rao, P. R. *Journal of Radioanalytical and Nuclear Chemistry* **2005**, *265*, 31-38.

(21)   Ouadi, A. Klimchuk, O. Gaillard, C.; Billard, I. *Green Chemistry* **2007**, *9*, 1160-1162.

(22)   Shirai, O. Iwai, T. Suzuki, Y. Sakamura, Y.; Tanaka, H. *Journal of Alloys and Compounds* **1998**, *271*, 685–688.

(23)   Reddy, B. P. Vandarkushali, S.; Venkatesh, P. *Electrochimica Acta* **2004**, 2471-2478.

(24)   Lebedev, V. A. Sal'nikov, V. I. Bychkov, A. V. Savochkin, Y. P.; Kormilitsyn, M. V. *Russ J Appl Chem* **2009**, *82*, 47-51.

(25)   Kinoshita, K. Koyama, T. Inoue, T. Ougier, M.; Glatz, J. P. *journal of physics and chemistry of solids* **2005**, *66*, 619–624.

(26)   Koyama, T. Iizuka, M. Shoji, Y. Fujita, R. Tanaka, H. Kobayashi, T.; Tokiwai, M. *Journal of Nuclear Science and Technology* **1997**, *34*, 384–393.

(27)   Nagai, T. Fujii, T. Shirai, O.; Yamana, H. *Journal of Nuclear Science and Technology* **2004**, *41*, 690–695.

(28)   Bhatt, A. May, I. Volkovich, V. Collison, D. Helliwell, M. Polovov, I.; Lewin, R. *Inorganic Chemistry* **2005**, *44*, 4934-4940.

(29)   Owen, T. *Fundamentals of UV-Visible spectroscopy primer*; Agilent Technologies, 2000.

(30)   Willard, H. Merritt, L.; Dean, J. *Instrumental Methods of Analysis*; 5th ed. D. Van Nostrand Company: New York, 1974.

(31)   Silverstein, R. M. Bassler, G. C.; Morrill, T. C. *Spectrometric Identification of Organic Compounds*; 4th ed. John Wiley & Sons: New York, 1981.

(32)   Thomson, J. *Sample Preparation & Liquid Scintillation Counting*; Perkin Elmer life sciences, 2003.

(33)   Ross, H. Noakes, J.; Spaulding, J. *Liquid scintillation counting and organic scintillators*; Lewis Publishers, Inc.: Chelsea, Michigan, 1991.

(34)   Elmer, P. *The 30-minute Guide to ICP-MS*; Perkin Elmer SCIEX, 2010.

(35)   Thomas, R. *Practical Guide to ICP-MS*; Marcel Dekker, Inc: New York, NY, 2004.

(36)   Dunlap, M.; Adaskaveg, J. E. Introduction to the Scanning Electron Microscope Theory, Practice, & Procedures **1997**.

(37)   Goldstein, J. Newbury, D. Joy, D. Lyman, C. Echlin, P. Lifshin, E. Sawyer, L.; Michael, J. *Scanning Electron Microscopy and X-Ray Microanalysis*; 3rd ed. Springer, 2003.

(38)   Warren, B. E. *X-Ray Diffraction*; Dover Publications: Mineola, NY, 1990.

(39)   *Industrial Applications of X-Ray Diffraction*; Chung, F.; Smith, D., Eds. 1st ed. CRC Press: New York, NY, 1999.

(40)   Bare, S. In *EXAFS Data Collection and Analysis Course*; 2005.

(41)   Introductory and Tutorial Information on XAFS. *XAFS.Org* **2006**.

(42)   Rundle, R. E. Baenziger, N. C. Wilson, A. S.; McDonald, R. A. *Journal of the American Chemical Society* **1948**, *70*, 99–105.

(43)   Taylor, J. C.; Hurst, H. J. *Acta Crystallographica Section B: Structural Crystallography and Crystal Chemistry* **1971**, *27*, 2018–2022.

(44)   Wang, J. *Analytical Electrochemistry*; John Wiley & Sons, 2000; Vol. 2nd.

(45)   Bard, A. J.; Faulkner, L. R. *Electrochemical Methods, Fundamentals and Applications*; 2nd ed. John Wiley & Sons: New Jersey, 2001.

(46)   Saheb, A. Janata, J.; Josowicz, M. *Electroanalysis* **2006**, *18*, 405-409.

(47)   Bhatt, A. I. Duffy, N. W. Collison, D. May, I.; Lewin, R. *Inorganic Chemistry* **2006**, *45*, 1677-1682.

(48)   Harris, D. *Quantitative Chemical Analysis*; sixth. W.H. Freeman and CO: New York, 2003.

(49)   Herstedt, M. Smirnov, M. Johansson, P. Chami, M. Grondin, J. Servant, L.; Lassegues, J. C. *Journal of Raman Spectroscopy* **2005**, *36*.

(50)   Basics of Karl Fischer Titration. *SigmaAldrich.com* **2010**.

(51)   Antoniou, S. Kolokassidou, C. Polychronopoulou, K.; Pashalidis, I. *J Radioanal Nucl Chem* **2009**, *279*, 863-866.

(52) Bernhard, G. Geipel, G. Brendler, V.; Nitsche, H. *Journal of Alloys and Compounds* **1998**, *271*, 201–205.

(53) Yang, Z. Coutinho, D. H. Yang, D.-J. Balkus Jr., K. J.; Ferraris, J. P. *Journal of Membrane Science* **2008**, *313*, 91-96.

(54) Burla, M. C. Caliandro, R. Camalli, M. Carrozzini, B. Cascarano, G. L. De Caro, L. Giacovazzo, C. Polidora, G.; Spanga, R. *J. Appl. Cryst.* **2005**, *38*, 381-388.

(55) Farrugia, L. J. *J. Appl. Cryst.* **1999**, *32*, 837-838.

(56) Sheldrick, G. M. *Acta Cryst. A* **2008**, *A64*, 112-122.

(57) Haas, A. Klare, C. Betz, P. Bruckmann, J. Kruger, C. Tsay, Y.-H.; Aubke, F. *Inorganic Chemistry* **1996**, *35*, 1918-1925.

(58) Duluard, S. Grondin, J. Bruneel, J.-L. Pianet, I. Grélard, A. Campet, G. Delville, M.-H.; Lassègues, J.-C. *J. Raman Spectrosc.* **2008**, *39*, 627-632.

(59) Umebayashi, Y. Mitsugi, T. Fukuda, S. Fujimori, T. Fujii, K. Kanzaki, R. Takeuchi, M.; Ishiguro, S.-I. *The Journal of Physical Chemistry B* **2007**, *111*, 13028-13032.

(60) Sadowski, P.; Majdan, M. *Monatshefte f\ür Chemie/Chemical Monthly* **1995**, *126*, 863–870.

(61) Prasad, E. Knettle, B. W.; Flowers, R. A. *J. Am. Chem. Soc.* **2002**, *124*, 14663-14667.

(62) Avens, L. R. Bott, S. G. Clark, D. L. Sattelberger, A. P. Watkin, J. G.; Zwick, B. D. *Inorg. Chem.* **1994**, *33*, 2248-2256.

(63) Zanella, P. Rossetto, G. De Paoli, G.; Traversero, O. *Inorganica Chimica Acta* **1980**, *44*, L155.

(64) Jie Luo; Ying Deng; Yuyu Sun *Journal of Bioactive and Compatible Polymers* **2010**, *25*, 185-206.

(65) Kerenskaya, G. Goldschleger, I. U. Apkarian, V. A. Fleischer, E.; Janda, K. C. *J. Phys. Chem. A* **2007**, *111*, 10969-10976.

(66) Schelter, E. J. Wu, R. Scott, B. L. Thompson, J. D. Cantat, T. John, K. D. Batista, E. R. Morris, D. E.; Kiplinger, J. L. *Inorganic Chemistry* **2010**, *49*, 924-933.

(67) Cotton, S. *Lanthanide and Actinide Chemistry*; 2nd ed. Wiley, 2006.

(68) Williams, D. B. Stoll, M. E. Scott, B. L. Costa, D. A.; Oldham, W. J. *Chemical Communications* **2005**, *2005*, 1438-1440.

(69) Matsumiya, M. Suda, S. Tsunashima, K. Sugiya, M. Kishioka, S.; Matsuura, H. *Journal of Electroanalytical Chemistry* **2008**, *622*, 129–135.

(70) Meinrath, G.; Kimura, T. *Inorganica Chimica Acta* **1993**, *204*, 79-85.

(71) Giridhar, P. Venkatesan, K. A. Subramaniam, S. Srinivasan, T. G.; Vasudeva Rao, P. R. *Journal of Alloys and Compounds* **2008**, *448*, 104-108.

(72) Dietz, M.L; Stepinski, D.C. *Talanta* **2008**, *75*, 598-603.

(73) Czerwinski, K. R. Zeh, P.; Kim, J. I. *Radiochim. Acta* **1997**, *76*, 3.

(74) Binnemans, K. *Chem. Rev.* **2007**, *107*, 2592-2614.

(75) Chao, X. U. XingHai, S. QingDe, C.; HongCheng, G. A. O. *Sci China Ser B-Chem* **2009**, *52*, 1858–1864.

(76) He-Fang Wang, Yi-Zhou Zhu, Xiu-Ping Yan,* Ru-Yu Gao, and Jian-Yu Zheng *Advanced Materials* **2006**, *18*, 3266-3270.

(77) Hirayama, N. Deguchi, M. Kawasumi, H.; Honjo, T. *Talanta* **2005**, *65*, 255–260.

(78) Conocar, O. Douyere, N.; Lacquement, J. *Journal of Nuclear Materials* **2005**, *344*, 136-141.

(79)   Marinsky, J. *Ion Exchange and Solvent Extraction*; Sengupta, A.; Marcus, Y., Eds. Marcel Dekker, Inc: New York, NY, 2004; Vol. 16.

(80)   Rydberg, J. Cox, M.; Musikas, C. *Solvent Extraction Principles and Practice*; 2nd ed. Marcel Dekker, Inc: New York, New York, 2004.

(81)   Markusson, H. Belières, J.-P. Johansson, P. Angell, C. A.; Jacobsson, P. *J. Phys. Chem. A* **2007**, *111*, 8717-8723.

(82)   Okada, Y.; Sawada, H. *Colloid Polym Sci* **2009**, *287*, 1359-1363.

(83)   Guillet, E. Imbert, D. Scopelliti, R.; Bünzli, J.-C. G. *Chem. Mater.* **2004**, *16*, 4063-4070.

(84)   Naudin, E. Ho, H. A. Bonin, M.-A. Breau, L.; Bélanger, D. *Macromolecules* **2002**, *35*, 4983-4987.

(85)   Matsumiya, M. Suda, S. Tsunashima, K. Sugiya, M. Kishioka, S.; Matsuura, H. *Journal of Electroanalytical Chemistry* **2008**, *622*, 129–135.

(86)   Kondo, M. Uchikawa, M. Namiki, K. Zhang, W. W. Kume, S. Nishibori, E. Suwa, H. Aoyagi, S. Sakata, M. Murata, M.; others *J. Am. Chem. Soc* **2009**, *131*, 12112–12124.

(87)   Billard, I. Mekki, S. Gaillard, C. Hesemann, P. Moutiers, G. Mariet, C. Labet, A.; Bunzli, J.-C. *G. Eur. J. Inorganic Chemistry* **2004**, *6*, 1190-1197.

(88)   Moustafa, E. M. Zein El Abedin, S. Shkurankov, A. Zschippang, E. Saad, A. Y. Bund, A.; Endres, F. *The Journal of Physical Chemistry B* **2007**, *111*, 4693-4704.

(89)   SAESOR, J. QUARTZ CRYSTAL MICROBALANCE DNA SENSOR FOR DETECTION OF VIBRIO CHOLERAE CTX GENE, MAHIDOL UNIVERSITY, 2006.

(90)   Pei, Z. Ma, X. Ding, P. Zhang, W. Luo, Z.; Li, G. *Sensors* **2010**, *10*, 8275-8290.

(91)   Parrish, J. D.; Little, R. D. *Tetrahedron Letters* **2001**, *42*, 7767–7770.

(92)   Hangarter, C. M. Bangar, M. Hernandez, S. C. Chen, W. Deshusses, M. A. Mulchandani, A.; Myung, N. V. *Appl. Phys. Lett.* **2008**, *92*, 073104.

(93)   Kuisma-Kursula, P. *X-ray Spectrometry* **2000**, *29*, 111–118.

(94)   JEOL USA Electron Optics Documents & Downloads.

(95)   Pashalidis, I. Czerwinski, K. Fanghänel, T.; Kim, J. I. *Radiochimica Acta* **1997**, *76*, 55-62.

(96)   Morss, L. R. Edelstein, N. M. Fuger, J. Katz, J. J. Kirby, H. W. Wolf, S. F. Haire, R. G. Burns, C. J.; Eisen, M. S. *The Chemistry of the Actinide and Transactinide Elements*; third. Springer Netherlands, 2006.

(97)   Wang, Z. Zachara, J. M. Yantasee, W. Gassman, P. L. Liu, C.; Joly, A. G. *Environ. Sci. Technol.* **2004**, *38*, 5591-5597.

(98)   Gureli, L.; Apak, R. *Separation Sc. & Tech.* **2005**, *39*, 1857-1869.

(99)   Meinrath, G. Lis, S. Pikula, Z.; Glatty, Z. *J. Chem. Thermodynamics* **2006**, *38*, 1274-1284.

(100) Morsi, M. *Communications of the American Ceramic Society* **1983**, C41-C43.

(101) Mǎluțan, T. Pui, A. Mǎluțan, C. Tǎtaru, L.; Humelnicu, D. *J Fluoresc* **2008**, *18*, 707-713.

(102) Shigematsu, Tsunenobu; Tabushi Masayuki; Tarumoto, Tsunehiko *J. Chem. Soc. Japan* **1960**, *81*, 262.

(103) Duluard, S. Grondin, J. Bruneel, J.-L. Pianet, I. Grélard, A. Campet, G. Delville, M.-H.; Lassègues, J.-C. *J. Raman Spectrosc.* **2008**, *39*, 627-632.

(104) Johansson, P. *J. Phys. Chem. A* **2001**, *105*.

(105) Wang, X.; Andrews, L. *Inorganic Chemistry* **2006**, *45*, 4157-4166.

(106) Zazhogin, A. P. Zazhogin, A. A. Umreiko, D. S.; Umreiko, S. D. *Journal of Applied Spectroscopy* **2009**, *76*, 89–92.

(107) Smolenskii, V. V. Bove, A. L. Borodina, N. P. Bychkov, A. V.; Osipenko, A. G. *Radiochemistry* **2004**, *46*, 583-586.

(108) Asanuma, N. Harada, M. Yasuike, Y. Nogami, M. Suzuki, K.; Ikeda, Y. *Journal of Nuclear Science and Technology* **2007**, *44*, 368–372.

(109) Hunter, D. B.; Bertsch, P. M. *Journal of Radioanalytical and Nuclear Chemistry* **1998**, *234*, 237-242.

(110) Petiau, J. Calas, G. Petitmaire, D. Bianconi, A. Benfatto, M.; Marcelli, A. *Phys. Rev. B* **1986**, *34*, 7350-7361.

(111) Allen, G. C. Tempest, P. A.; Tyler, J. W. *Nature* **1982**, *295*, 48-49.

(112) Allen, G. C.; Tempest, P. A. *J. Chem. Soc., Dalton Trans.: Inorganic Chemistry* **1982**, 2169-2173.

(113) Allen, G. C.; Tempest, P. A. *J. Chem. Soc., Dalton Trans.: Inorganic Chemistry* **1983**, 2673-2677.

(114) Hofman, G. L. Wiencek, T. C. Wood, E. L. Snelgrove, J. L. Suripto, A. Nasution, H. Amin, D. L.; Gogo, A. In *19th International Meeting on Reduced Enrichment for Research and Test Reactors*; 1996.

(115) Doebling, S. W. Farrar, C. R. Prime, M. B.; Shevitz, D. W. *Damage identification and health monitoring of structural and mechanical systems from changes in their vibration characteristics: a literature review*; Los Alamos National Lab., NM (United States), 1996.

(116) Koo, Y. H. Lee, C. T. Oh, J. Y. Sohn, D. S. Baryshnikov, M. Chechurov, A.; Margulis, B. *Nuclear Engineering and Design* **2008**, *238*, 1592–1600.

(117) Iizuka, M. Koyama, T. Kondo, N. Fujita, R.; Tanaka, H. *Journal of Nuclear Materials* **1997**, *247*, 183–190.

(118) Koyama, T. Iizuka, M. Shoji, Y. Fujita, R. Tanaka, H. Kobayashi, T.; Tokiwai, M. *Journal of Nuclear Science and Technology* **1997**, *34*, 384–393.

(119) Guillaumont, R. Fanghänel, T. Fuger, J. Grenthe, I. Neck, V. Palmer, D. A.; Rand, M. H. *Update on the Chemical Thermodynamics of Uranium, Neptunium, Plutonium, Americium and Technetium*; Elsevier Science, 2003.

(120) Facts About Hydrogen Fluoride (Hydrofluoric Acid). *Centers for Disease Control and Prevention* **2005**.

(121) L. Berthon, S. I. N. *Dalton Trans.* **2006**, 2526-2534.

(122) Maury, O. Ephritikhine, M. Nierlich, M. Lance, M.; Samuel, E. *Inorganica Chimica Acta* **1998**, *279*, 210-216.

(123) Brodsky, M. B.; Carleson, B. G. F. *Journal of Inorganic and Nuclear Chemistry* **1962**, *24*, 1675-1681.

(124) Scott, V. J. Labinger, J. A.; Bercaw, J. E. *Organometallics* **2010**, *29*, 4090-4096.

(125) Titretir, S. Erdoğdu, G.; Karagözler, A. E. *J Anal Chem* **2006**, *61*, 592-595.

(126) Howlett, P. C. Izgorodina, E. I. Forsyth, M.; MacFarlane, D. R. *Zeitschrift fur Physikalische Chemie* **2006**, *220*, 1483-1498.

(127) Obliers, B. Broekmann, P.; Wandelt, K. *Journal of Electroanalytical Chemistry* **2003**, *554*, 183–189.

(128) Smith, D. K. Miller, N. R.; Korgel, B. A. *Langmuir* **2009**, *25*, 9518-9524.

(129) Durney, L. *Electroplating Engineering Handbook*; Fourth. Chapman & Hall: London, 1996.

(130) Djokic, S. *Modern Aspects of Electrochemistry - Electrodeposition: Theory and Practice*; Springer: London, 2010; Vol. 48.

(131) Dinnebier, R. Workshop Powder Diffraction Structure Determination and Refinement from Powder Diffraction Data **2000**.

(132) Mudring, A.-V.; Tang, S. *Eur. J. Inorg. Chem.* **2010**, *2010*, 2569-2581.

(133) Fernicola, A. Navarra, M.; Panero, S. *Journal of Applied Electrochemistry* **2008**, *38*, 993-996-996.

(134) Li, H.-L. Chambers, J. Q.; Hobbs, D. T. *Journal of Applied Electrochemistry* **1988**, *18*, 454-458-458.

(135) Shriver, D. F.; Atkins, P.J. *Inorganic Chemistry*; 3rd ed. W.H. Freeman and CO: New York, 1999.

Vita

Graduate College

University of Nevada, Las Vegas

Wendy Jacqueline Pemberton

Home Address:

1176 Hollow Reed Court

Henderson, NV 89011

Degrees:

Bachelor of Science, Chemistry, 2006

Dissertation Title: Synthesis, Extraction, Dissolution, and Voltammetry of

F-Species in a Room Temperature Ionic Liquid Solvent

Dissertation Examination Committee:

Chairperson, Kenneth R. Czerwinski, Ph. D.

Committee Member, David W. Hatchett, Ph. D.

Committee Member, Al Sattelberger, Ph.D.

Graduate Faculty Representative, Ralf Sudowe, Ph. D.